2023-01-16

Evaluation of Injury and Repair in Multiple Sclerosis Using Advanced MRI Methods

Hosseinpour, Zahra

UNIVERSITY OF CALGARY

Evaluation of Injury and Repair in Multiple Sclerosis Using Advanced MRI Methods

by

Zahra Hosseinpour

A THESIS

SUBMITTED TO THE FACULTY OF GRADUATE STUDIES

IN PARTIAL FULFILLMENT OF THE REQUIREMENTS FOR THE

DEGREE OF DOCTOR OF PHILOSOPHY

GRADUATE PROGRAM IN BIOMEDICAL ENGINEERING

CALGARY, ALBERTA

JANUARY, 2023

Abstract

Multiple sclerosis (MS) is an inflammatory demyelinating and neurodegenerating disease of the central nervous system impacting more than 2.8 million people worldwide. Many of the people experience paramount disability after 10-15 years of disease onset. Optimal management requires accurate measurement of tissue pathology, including the likelihood of repair in lesions. However, there is no established marker of lesion severity in vivo. This project aimed to develop methods to characterize tissue injury and repair as seen in focal lesions based on brain magnetic resonance imaging (MRI) of relapsing-remitting MS (RRMS). The focus was on image processing techniques ranging from development, validation, to application. Initially, based on histology-informed MRI of postmortem MS brains, I conducted texture analysis using an optimized method known as gray level co-occurrence matrix (GLCM) and compared texture analysis to advanced MRI measures using machine learning models for classifying MS pathology, including de- and re-myelinated lesions. Based on the selected MRI measures, I then developed a percentile approach for characterizing MS lesion severity in clinical MRI, and for assessing lesion recovery in clinical trial MS participants. Overall, brain MRI texture measures performed the best in differentiating de- and re-myelination. These measures characterized 2 extreme types of MS lesions on de- and re-myelination, which differentiated men from women, and detected significant recovery in acute MS lesions with treatment. Collectively, advanced texture analysis in clinical MRI is promising for characterizing lesion injury and repair in MS. This ability is critical for improved evaluation of both disease activity and treatment response for MS participants.

Preface

Chapter 3 of this thesis has been published as Z Hosseinpour et al. “Texture analysis in brain T2 and diffusion MRI differentiates histology-verified grey and white matter pathology types in multiple sclerosis” Journal of Neuroscience Methods 379 (2022): 109671.

Chapter 4 and Chapter 5 of this thesis make up two research manuscripts in preparation for submission at the time of this thesis submission.

Acknowledgment

I would like to express my deepest appreciation to my supervisor, Dr. Yunyan Zhang, for her expertise, guidance, and constant support during my Ph.D. study. I appreciate her knowledge and technical skills and am very thankful for the experiences I have gained under her supervision.

I am immensely grateful to my supervisory committee Dr. Bruce Pike and Dr. Wee Yong, for their guidance and support through my research; your ideas, advice, and feedback have been truly invaluable. I want to thank the Biomedical Engineering department for providing me with the opportunity to learn and develop my skills. I am also thankful to my lab members, Glenn Pridham and Olayinka Oladosu, for their help.

Ultimately, I want to thank my family, particularly my parents, for their unconditional support throughout my life.

Dedication

To my late father and my devoted mother for their endless love and support. I hope this achievement will fulfill the dream they envisioned for me.

Table of Content

List of Tables

List of Figures

List of Abbreviations

Abbreviation	Definition
MS	Multiple sclerosis
MRI	Magnetic resonance imaging
MTR	Magnetization transfer ratio
DTI	Diffusion tensor imaging
GLCM	Grey-level co-occurrence matrix
FLAIR	Fluid attenuated inversion recovery
RRMS	Relapsing-remitting MS
CNS	Central nervous system
SPMS	Secondary–Progressive MS
PPMS	Primary–Progressive MS
NAWM	Normal appearing white matter
CSF	Cerebrospinal fluid
DWI	Diffusion–weighted imaging
MWI	Myelin water imaging
MTI	Magnetization transfer imaging
SWI	Susceptibility-weighted imaging
MD	Mean diffusion
FA	Fractional anisotropy
AD	Axial diffusivity
RD	Radial diffusivity
MWF	Myelin water fraction
QSM	Quantitative susceptibility mapping
STI	Susceptibility tensor imaging
ASM	Angular second moment
PST	Polar Stockwell transform
RF	Random forest
SVM	Support vector machine
PCA	Principal component analysis
DAWM	Diffusely abnormal white matter
remWM	White matter remyelinated lesion
demWM	White matter demyelinated lesion
remGM	Grey matter remyelinated lesion
demGM	Grey matter demyelinated lesion
NAGM	Normal appearing grey matter
ROI	Regions of interest
RFE	Recursive feature elimination
sDEM	Severely demyelinated
hREM	Highly remyelinated
EDSS	Expanded disability status scale
DMT	Disease modifying therapies

CHAPTER1: Introduction

2.1 Overview of research

Multiple sclerosis (MS) is a common inflammatory demyelinating and neurodegenerative disease of the central nervous system, affecting >2.8 million people globally [1]. There is no cure. Further, MS pathology is highly heterogeneous, making accurate disease measurement and treatment evaluation extremely challenging. Without appropriate management, many of the patients will end up with significant disability after 10-15 years of disease onset, such as those with the relapsing-remitting form of MS (RRMS) [1, 2]. Hence, there is a critical need for precise assessment of MS pathology.

Tissue damage in MS is mediated by several factors including inflammation, demyelination, and axonal loss [3]. In many of the patients, repair such as remyelination also occurs and can be improved by treatment with a potential repair agent [4, 5], particularly in lesions with acute inflammation [6, 7]. Focal lesions remain to be the hallmark of MS pathology [8]. Accurate assessment of the characteristics and severity of lesions may enable early identification of patients who deserve early initiation of target therapies. Early treatment has shown enormous potential to slow disease progression, and likely even promote repair [9]. However, there is still lack of established measures for assessing tissue injury and repair in MS in vivo [10].

Magnetic resonance imaging (MRI) is an ideal method for both diagnosis and management of MS. In clinical imaging, conventional MRI scans are routinely used to evaluate disease activity and

treatment response such as lesion burden and the presence of new lesion activities. However, conventional MR imaging has difficulty detecting subtle changes at a tissue level following injury and repair [11]. Advanced MRI methods, including magnetization transfer (MT) imaging, myelin water imaging, and diffusion tensor imaging (DTI), have shown increased specificity to MS pathology and therefore may be able to overcome some of the limitations inherent to conventional MRI [12]. But these techniques are not commonly used in clinical imaging protocols.

Advanced analysis of the 'texture' of brain MRI has shown the promise for robust characterization of MS pathology. Texture refers to the brightness or darkness of a pixelated area in an image. Texture analysis identifies structural characteristics by assessing the distribution pattern of image signal intensity [13]. There are different approaches to use in texture analysis, including statistical, spectral, and structural (syntactic) [14], with the former 2 types being applied the most. Texture analysis can be applied to any digital images, including conventional and advanced MRI. Grey level co-occurrence matrix (GLCM) is one of the most widely used statistical texture analysis method [15]. Previously, GLCM texture analysis using T2-weighted MRI has shown the ability to classify MS lesions, normal appearing white matter in MS, and heathy white matter tissues [16]. Using the fluid attenuated inversion recovery (FLAIR) MRI, GLCM features have also demonstrated the power to detect early structural changes in healthy brain white matter [13]. Similar results are found in texture analysis of MS using frequency-based methods [17]. Further, based on advanced MRI such as diffusion imaging, another study has derived new computational measures of the directionality of diffusion MRI using the GLCM texture analysis method. This study has discovered that the diffusion texture MRI measures are more accurate than traditional DTI metrics in brain structure characterization [18]. Further, recent evidence suggests that

combining with machine learning algorithms may further increase the capacity of texture analysis in MS pathology evaluation [19]. However, many of the texture analysis studies are limited by either lack of thorough validation or lack of in vivo application. This thesis project plans to address these issues by using brain MRI datasets from both postmortem samples and living participants with MS.

2.2 Hypothesis and aims

MS is a complex disease with dynamically changing and unpredictable pathology. While different imaging techniques are under development, there is still lack of competitive measures of tissue characteristics in vivo in MS. Both disease monitoring and treatment discovery require accurate measurement of tissue pathology. Strong evidence suggests that the texture patterns of MRI signal intensity relate to the degree of tissue integrity [20, 21]. Given the possibility of using texture analysis in a clinical setting, I hypothesize that advanced image texture analysis will provide new sensitive measures of tissue integrity, and that applying these measures in clinical imaging will facilitate the characterization of lesion severity and recovery following injury in MS. My overall goal of this thesis project is to develop, validate, and apply new MRI methods based on optimal texture analysis techniques for improved measurement of MS pathology particularly regarding tissue injury and repair in lesions. The availability of these methods can aid to find new outcome measures of injury and repair in MS or other similar diseases and advance disease monitoring regarding both disease activity and treatment response. This thesis includes 3 specific aims as described below.

Aim1. Develop new image analysis methods including texture analysis and validate the imaging outcome with postmortem samples.

Aim2. Evaluate the utility of the newly developed imaging methods for assessing lesion property such as de- and re-myelination in living MS participants recruited in a clinical study.

Aim3. Evaluate longitudinal changes in enhancing and non-enhancing MS lesions employing validated texture analysis methods and estimate injury and repair after treatment with domperidone to assess the treatment response.

2.3 Thesis organization

The overall objective of this thesis is to develop methods for characterizing tissue injury and repair such as de- and re-myelination associated with lesions in MS. The process involves 3 key steps: 1) method implementation and validation ex vivo; 2) in vivo implementation and assessment using cross-sectional patient data; and 3) in vivo assessment using longitudinal patient data. Specifically, technical development in step 1 includes texture analysis of both conventional and advanced MRI scans from postmortem brain samples of MS patients assisted by machine learning modeling. Using knowledge generated from the postmortem data, step 2 takes advantage of archived brain MRI scans obtained at screening for a well-characterized clinical trial in living MS participants. This is followed by longitudinal analysis in step 3 for a portion of the trial eligible MS participants applying the validated approaches and measurements in previous steps.

Chapter one provides a brief overview of research, hypothesis, the three specific aims, and the organization of the thesis.

Chapter 2 is the literature review. It consists of an overview of MS, common MRI modalities for MS, and image analysis techniques. Both advanced and conventional MRI techniques including their theory, acquisition and application in MS are discussed in this chapter. Additionally, image analysis techniques including the associated image pre-processing steps different texture analysis techniques and a brief review of machine learning algorithms are provided.

Chapter 3 represents the texture analysis of advanced and conventional MRI of MS postmortem brain combined with a machine learning algorithm for classifying MS pathology subtypes, including de- and re-myelination. The texture measures were also compared with two common advanced MRI measures: magnetization transfer ratio (MTR) and fractional anisotropy (FA) for tissue classification. GLCM texture analysis using conventional MRI has been conducted, and a new analysis method for high angular diffusion MRI, namely, voxel-based analysis of diffusion texture, has been employed. These evaluations have been validated against histology from postmortem brain samples with MS to assess the capability of the proposed method for evaluating pathological changes such as de- and re-myelination.

Chapter 4 investigates the feasibility of using the histology-validated image analysis techniques from Chapter 3 in living MS participants to classify MS lesion types in vivo. I evaluated in vivo MS lesions utilizing texture analysis of the standard clinical imaging sequences FLAIR MRI. The goal was to define lesions' severity respecting the degree of myelination and identify two critical

MS lesion types: severely demyelinated (sDEM) and highly remyelinated (hREM). Percentile statistics of the verified GLCM texture measurements were used for lesion identification. The lesion probability maps were then calculated to characterize the distribution of the identified lesion types in the brain. Additionally, the two lesion types were compared between age groups and sexes.

Chapter 5 presents the longitudinal analysis of lesion changes in MS participants recruited in a clinical study following add-on treatment with a candidate reparative drug, domperidone. The assessment used a GLCM based on FLAIR MRI, focusing on top selected texture measures in previous aims. For comparison, we also evaluated acute lesions in the control group without the domperidone add-on and non-acute lesions in both the groups with and without add-on. Additionally, participants were divided into low and high response groups respecting the level of a hormone prolactin and evaluated correspondingly.

Finally, the overall summary, discussion, conclusion and the key findings of the thesis are presented in **Chapter 6**. The future direction is briefly discussed to further investigate the capability of the presented approaches in assessing disease activity and treatment impact in MS or other similar diseases compared with other quantitative measures from conventional or advanced MRI.

CHAPTER 2: Literature Review

3.1 Overview of MS

3.1.1 General Characteristics

MS is a chronic inflammatory demyelinating, and neurodegenerative disease that engages the central nervous system (CNS) [22]. Approximately 2.8 million people are affected globally [23]. Genetically susceptible subjects are more prone to develop MS, particularly being exposed to environmental factors, including smoking, latitude, and vitamin D deficiency [24]. The clinical symptoms of MS are demyelinated plaques inside the CNS [22]. Myelin is a spiral glial cell membrane around the axon. Glial cells consist of the Schwann cells in the peripheral nervous system and oligodendroglial cells in the CNS. The myelin sheath enhances axonal conduction velocity while providing protection to the surrounded axons. Oligodendrocytes also provide trophic support to the axons [4, 25]. The infiltration of different immune cells to the CNS causes inflammation and myelin damage (demyelination), which can lead to secondary macrophage recruitment and further demyelination [26]. When demyelination occurs, signals cannot be transferred as before, and the axons can go on degeneration, leading to neurologic disability in MS patients [27]. On the other hand, myelin can be repaired through a process known as remyelination that can improve nerve impulse conduction and preserve the axons from further degeneration [28]. However, the repaired myelin may not be exactly the same as the intact sheath (Figure 2.1), particularly when some degrees of axonal damage are available [29]. Overall, the key features of MS include demyelination, remyelination, inflammation, and axonal loss. There is currently no cure for MS, but some medications are beneficial to help the remyelination process and mitigate symptoms such as domperidone..

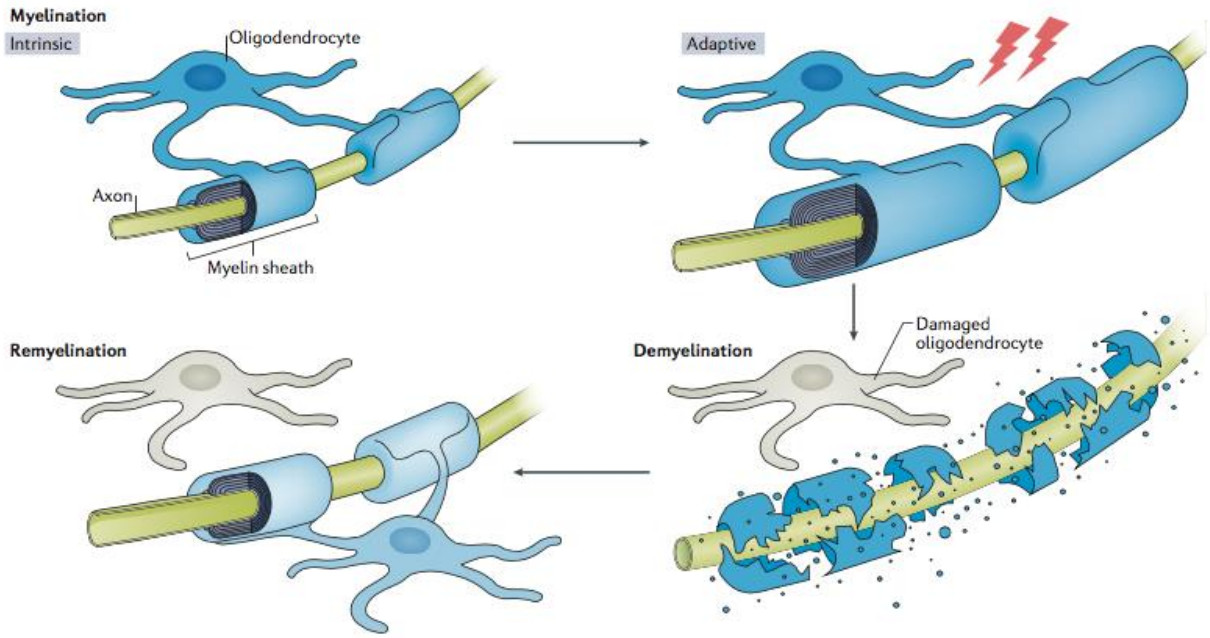

Figure 3.1. The process of myelination, demyelination and remyelination. Remyelinated axons can be distinguished by their thinner myelin sheaths (Image adapted from [29]).

3.1.2 **MS pathology**

MS plaques are still the hallmark of MS pathology. These focal lesions can be classified into different types according to their pathological features, stages, changing patterns, and inflammatory presence. Acute, chronic active, and chronic silent lesions may happen during the disease course [30]. Acute lesions indicate the primary stage of lesion development and contain strong inflammatory infiltration and ongoing demyelination throughout the plaque. Acute plaques are mostly seen in RRMS and may indicate a pathologic sign of disease attack [31]. Remyelination occurs in MS, and the degree of remyelination might be significantly different between different lesions [6, 7].

The main pathologic feature of chronic MS lesions is multifocal demyelinated regions [26]. Their borders are more distinct than acute lesions because the inflammatory cells are more pronounced at the border of the chronic lesions, whereas they are distributed throughout the acute lesions [30]. Based on the type of tissue destruction, chronic lesions are divided into two main forms: chronic active and chronic inactive [30]. In chronic active lesions, centrifugal inflammation and demyelination are dominant along the edges and decline toward the center. Remyelination usually appear on the border of chronic active lesions [30, 31]. With respect to chronic inactive lesions, they are typically hypocellular accompanied by complete demyelination, and there is no apparent inflammation at the edges of the lesions [8]. Remyelination happens rarely in chronic inactive lesions, as oligodendrocytes are essentially all gone [30, 31].

3.1.3 **MS subtypes**

There are different clinical forms of MS. The RRMS form is defined by inflammatory attacks (relapses) where complete or near complete recovery (remission) of symptoms can follow [32]. Up to 80% of MS patients belong to this group [33, 34]. Most of the untreated RRMS patients progress after a median time of 19 years from the beginning of their disease [35]. Instead of having a relapsing and remitting episode that can be relatively easily determined, the RRMS patients begin to see their illnesses advance progressively and insidiously without remission. At this stage, the disease form is called secondary–progressive MS (SPMS). Primary–progressive MS (PPMS) is another subtype of MS that affects fewer patients (10-20%). This subtype is progressive right from disease onset and does not feature distinct attacks [34].

3.2 MRI of MS

Magnetic Resonance Imaging (MRI) is one of the most effective imaging modalities for MS diagnosis and disease evaluation including lesion assessment [36]. However, characterizing de- versus re-myelinated lesions with conventional MRI is not intuitive [4, 28] (Figure 2.2). Advanced MRI techniques hold more promise for better detection of structural tissue changes and the disease. This includes methods that combine image processing techniques with conventional or advanced MRI, such as texture analysis [28]. The sections below will review common MRI techniques used in clinical or research imaging of MS.

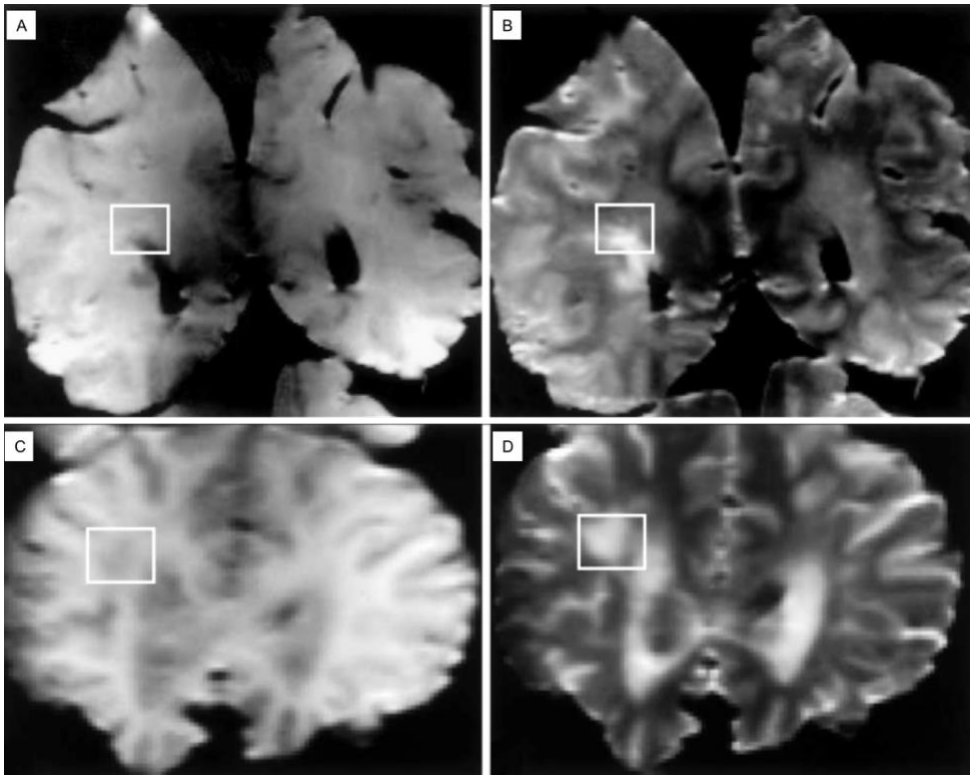

Figure 3.2. Histology-verified demyelinated and remyelinated lesions on MRI. Shown are demyelinated lesions on coronal postmortem T1-weighted (A) and T2-weighted (B) (top row); and fully remyelinated lesions on coronal postmortem T1-weighted (C) and T2-weighted (D) (bottom row) (image adapted from [37]).

3.2.1 **Conventional MRI methods**

T1- Weighted MRI

Conventional MRI is highly sensitive in the assessment of MS disease activity [38]. They provide image contrast based on tissue properties. MRI physics defines two different relaxation times in a tissue. Longitudinal relaxation time (T1) is the time of energy exchange when excited protons return to the equilibrium. T1-weighted imaging is based on the longitudinal relaxation time of tissues and is acquired by employing short repetition time and very short echo time. Fatty tissues appear bright, in contrast to non-fatty tissues which appear dark on T1-weighted MRI [39] (Figure 2.3). In unenhanced T1-weighted images, some lesions hold an isointense appearance, but most appear hypointense (black hole) compared to normal-appearing white matter (NAWM) [38]. In the chronic stage, the hypointense appearance of MS lesions observed on pre-contrast T1-weighted MRI is a sign of significant and irreversible tissue damage [38, 40].

Post-contrast T1-weighted imaging helps detect the breakdown of blood-brain barrier, visible with gadolinium enhancement [40]. Active lesions are correlated with disruption of the blood-brain barrier and therefore appear bright following gadolinium injection [38]. Enhanced lesions often hold a ring or nodular shape [41]. New MS lesions are mostly characterized as nodular regions of gadolinium enhancement on T1-weighted images [38]. While contrast enhancement finishes, some black holes become isointense. This alteration of appearance in MRI is considered a sign of tissue repair [38] and is sometimes used as a marker in clinical trials [42]. But there are drawbacks with this approach including the inherent low specificity of T1-weighted imaging to MS pathology and the uncertainty on how to appropriately interpret the intensity of black holes.

T2- Weighted MRI

Transverse relaxation time (T2) is the time constant that protons take to loose phase coherency, resulting in decreasing transversal magnetization and signal loss [39]. T2-weighted imaging is based on the T2 relaxation time of tissues. Using a long repetition and long echo time, T2-weighted images are generated. High water content tissues look bright in T2-weighted images [43]. T2-weighted imaging is effective for MS lesion detection, and most of the detected lesions show a round or oval shape. The lesions are spread across the CNS but are mostly seen in the periventricular area. Although MS is known as a white matter (WM) disease, grey matter (GM) can also be involved. Lesions in the GM are divided in different types based on their location: extended through WM and GM, restricted to the cortex, and extended from subpial areas to the cortical layers [44]. GM lesions are generally bright on T2-weighted imaging [40], including the new, active ones. Edema resolution and tissue repair change the size of these new lesions over time [38]. Acute MS lesions often have a more complicated appearance: hyperintense in the center and iso- or hypo-intense around it. T2-weighted images are not pathologically specific, and different lesion processes such as inflammation and de- or re-myelination cannot be easily discriminated by this imaging modality [40].

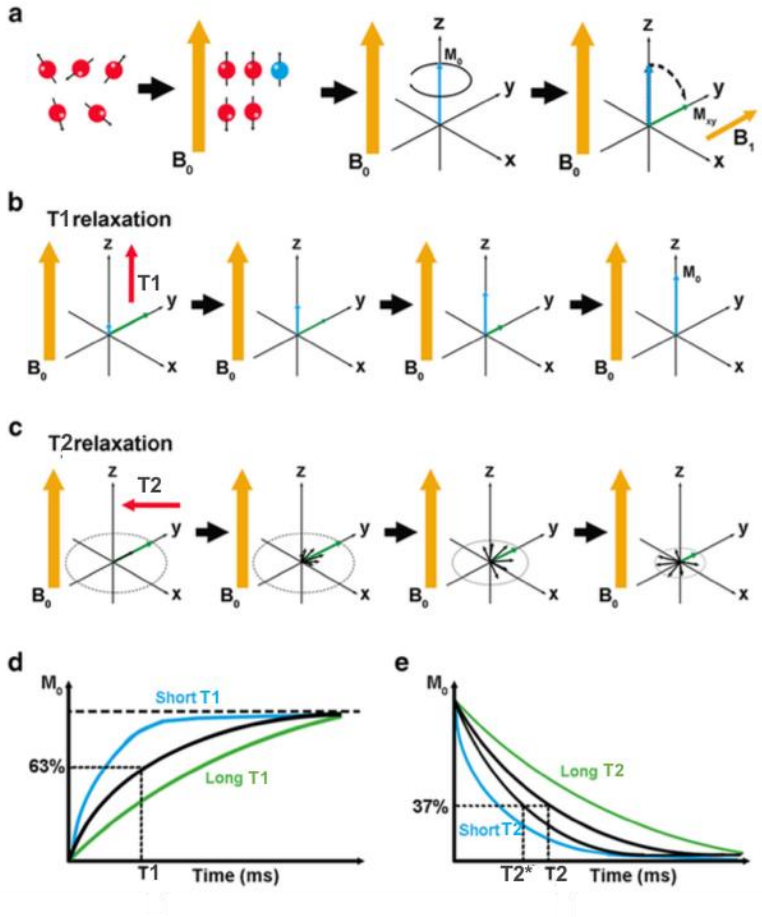

Figure 3.3. A graphic diagram of the basic MRI physics. The red balls represent protons spinning around their axis and tend to align with the direction of the applied external magnetic field, B_0, with spin-up and spin-down orientations. The resultant difference between parallel and antiparallel protons (blue ball) represents the protons that produce the MRI signal. The magnetization vector, M_0, is the sum of these protons, which can be tilted in the presence of a second magnetic field (B_1) orthogonal to B_0 at the x-y plane (M_{xy}). When B_1 is turned off, M_{xy} returns to equilibrium by two relaxation processes: T1 and T2 (a). T1 relaxation (b), T2 relaxation (c), T1 relaxation curve, in which tissues with short T1 (blue) and long T1 (green) values are shown (d) T2 relaxation curve, in which tissues with short T2 (blue) and long T2 (green) values are shown (image adapted from [45]).

Fluid attenuated inversion recovery (FLAIR) MRI

FLAIR imaging produces T2-weighted images with nulled cerebrospinal fluid (CSF). The signal from CSF is suppressed by employing a long delay time after a 180-degree radiofrequency pulse (RF) in MR imaging, which is called inversion time (TI) [46]. In addition to suppressing the CSF signal, the effects of blood flow are also removed by the FLAIR sequence, leading to a better visualization of MS lesions [47]. FLAIR images enhance the appearance of periventricular lesions but have less sensitivity in depicting lesions located in the brainstem or cerebellum [40]. FLAIR imaging is used successfully for MS lesion segmentation, particularly for lesions located in the periventricular and subcortical WM regions [47, 48]. The precision that FLAIR images provide in lesion depiction forms an important reason for them to be chosen in MS lesion segmentation [48].

3.2.2 **Advanced MRI methods**

Conventional MRI images face challenges in characterizing subtle structural changes. These may include detecting injuries in the NAWM, presence of grey matter lesions, and changes within lesions such as repair. Advanced MRI methodologies may address these issues. Through advanced imaging we can measure pathological changes in MS lesions with additional detail and monitor the process of repair [39]. Examples of advanced MRI techniques that showed potential for assessing tissue injury and repair include diffusion–weighted imaging including diffusion tensor imaging (DTI) and high angular resolution diffusion–weighted imaging, magnetization transfer imaging (MTI), myelin water imaging (MWI), and susceptibility-weighted imaging (SWI) [49, 50]. MTI and MWI are sensitive to myelin integrity [51, 52]. Diffusion-related imaging is used for myelin and axon integrity, and injury and repair assessment [49]. SWI can be used for injury and repair assessment, such as myelin density and iron content identification [53].

Diffusion magnetic resonance imaging

Diffusion-weighted MRI is based on the activity of water molecule movement in tissues and is effective in brain WM imaging. The diffusion of molecules is associated with their action of random motion due to the effect of thermal energy. Diffusion coefficient refers to the mean squared random displacement of molecules in a particular medium per time unit. The probability distribution of molecules displacement in free diffusion (no boundaries) is isotropic, with a Gaussian distribution and without any distinguished direction [54]. However, biological tissues consist of different components that restrict the movement of molecules (Figure 2.4) [55]. Therefore, the diffusion coefficient of water molecules, also called the apparent diffusion coefficient, in human brain is lower than the diffusion coefficient of free water molecules. This is partly due to the tightly attached axons, which are completely aligned and are surrounded by the myelin sheath as seen in healthy conditions. As a result, the displacement of water molecules in axons is not unrestricted [54].

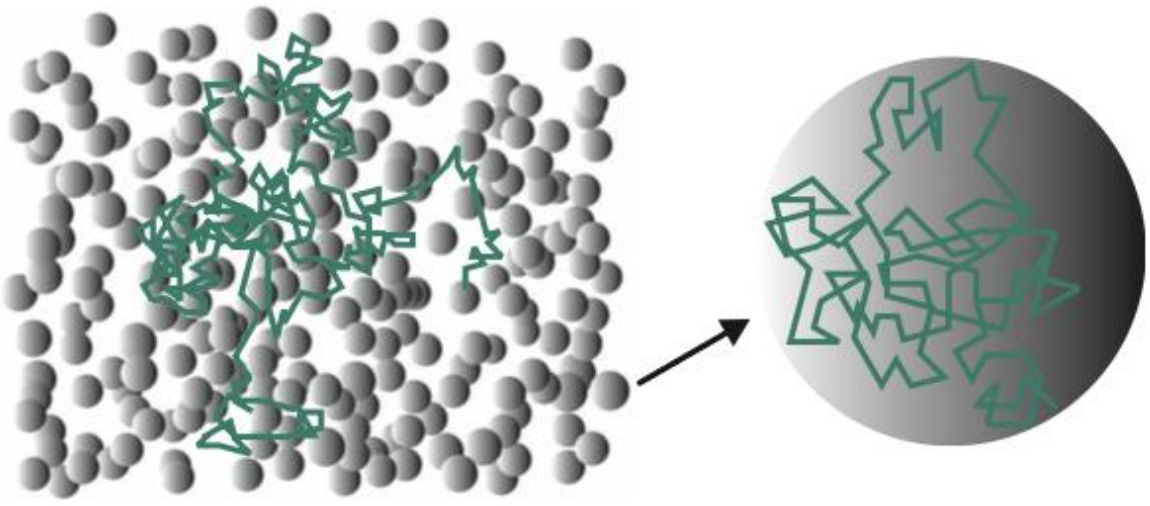

Figure 3.4. A diagram of diffusion phenomenon. Shown are the hindered motion of extracellular water molecules (left), and restricted diffusion inside a cell by the cellular membranes (right) [55].

The simplest kind of diffusion imaging is DWI, which is acquired by using a single pulse gradient spin-echo sequence in various gradient directions [56]. Diffusion Tensor Imaging (DTI) uses a diffusion model with a Gaussian distribution called a tensor model to estimate tissue diffusion characteristics. Diffusion is orientation dependent, and acquisition in three dimensions (x, y, z) are needed. For DTI, at least six diffusion images are required to reconstruct diffusion indices. Several scalar measurements can be extracted from DTI: mean diffusion (MD), a measure of water movement without considering the directionality; fractional anisotropy (FA), an invariant measure of anisotropy and fiber directionality; axial diffusivity (AD), an estimate of diffusion parallel to the direction of fiber tract; and radial diffusivity (RD), a measure of diffusivity in the direction perpendicular to that of the fiber tract [56, 57]. As described before, the water molecules have different behaviors in different environments. Isotropic tissues represent an environment that has less restricted water movement, while anisotropic tissues feature restricted water movement.

DTI defines different diffusion characteristics of a tissue, such as magnitude, the level of anisotropy, and the anisotropic orientation. Different pathological processes in the brain can cause microstructural changes and hence water movement. In MS, pathological changes such as inflammation, demyelination, and axonal damage can all cause alterations in DTI. Indeed, MS lesions show higher MD, lower FA and higher RD compared to NAWM [58-60]. Nonetheless, DTI also has some limitations, the most important of which is its Gaussian distribution assumption for the diffusion model. It is suitable for single fiber population, but this is unrealistic in the WM which includes multiple fiber crossings. Therefore, new models are needed to be able to model non-Gaussian diffusion signals [57, 59].

High Angular Resolution Diffusion Imaging (HARDI)

The HARDI is a relatively new diffusion imaging technique. It uses a much larger number of diffusion gradient directions than DTI. Therefore, HARDI can capture higher angular resolution of diffusion signals [61, 62]. Based on the increased number of diffusion directions, HARDI improves the DTI fiber tracking by distinguishing multiple fiber populations [62]. Compared to DTI, HARDI can also depict additional microstructural details as seen in areas with multi-fiber crossing. Further, HARDI signal reconstruction can be model-independent employing Q-ball imaging method [63]. The diffusion MR signal is derived by employing the probability density function of the random displacement of protons. Thus, it can properly define the diffusion characteristics in complex tissues. Using this technique, Santis et al. characterized axonal damage by estimating axonal diameter in the brain of MS patients compared with healthy control subjects [64]. HARDI also demonstrates the ability for distinguishing fine axonal connections in the spinal cord [65]. One outstanding shortcoming of HARDI is the long acquisition time (10-20 minutes). Overall, high-resolution diffusion-weighted MRI holds considerable potential in detecting subtle tissue abnormalities in various systems including the CNS and is used in this thesis project [66].

Magnetization Transfer Imaging (MTI)

MTI provides contrast based on the magnetization exchange between protons bounded to macromolecules (bound pool) such as myelin and protons in the surrounding free water pool. The bound pool of protons is first saturated with a radiofrequency (RF) pulse; when returning to the equilibrium, these protons transfer their magnetization to the free water pool and make it partially saturated. This attenuation in MR signal can be detected with use of another RF pulse. Consequently, MTI can detect characteristics of macromolecules indirectly [67] (Figure 2.5).

Myelin is a structure containing macromolecules such as proteins and lipids. MTI can be used to measure myelin changes with measuring magnetization transfer ratio (MTR), a measure of the amount of bound protons based on subtraction of images before and after the application of a saturation pulse. Decreased MTR relates to demyelination and MTR increase is consistent with remyelination [68]. MTR decline has been reported in acute and chronic MS lesions, indicating demyelination [38, 69]. Nevertheless, MTR values may also be affected by inflammation and edema, and MTR changes are not exclusively due to myelin content alteration [70]. MTR is used in the current study to be compared with MRI texture measurements derived from GLCM using postmortem data.

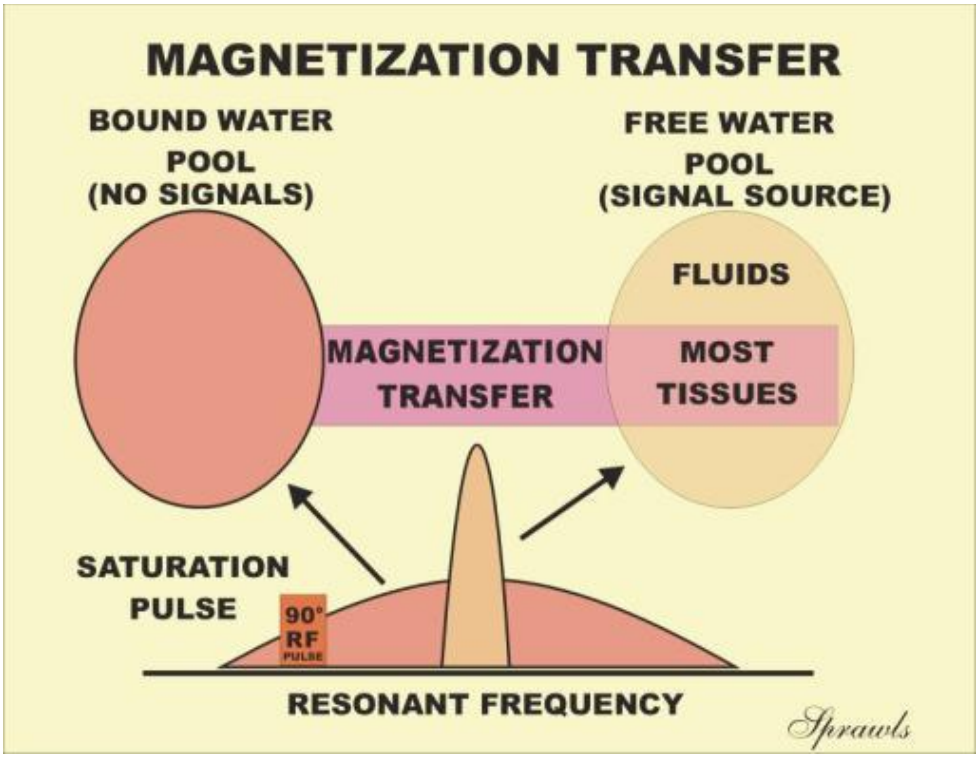

Figure 3.5. Principles of magnetization transfer imaging. The signal coming from the bound pool, such as myelin, can be detected by magnetization transfer between the free pool, reflecting free water proton, and the bound pool [71].

Myelin water imaging (MWI)

The MWI is another MR technique which gives insight into myelin structure. This technique takes advantage of the short T2 relaxation time of water molecules inside myelin, compared to intracellular and extracellular water. A myelin water fraction (MWF) is calculated in MWI, which is the ratio of the short T2 distribution presumably originated from myelin water and the total T2 distribution [69]. Although not in routine clinical use, MWF has been used in research for studying myelin characteristics in MS and other brain disorders. In a longitudinal study of lesion evolution, there was a considerable improvement after median follow up of 6 months in the MWF of gadolinium-enhanced lesions compared to non-enhanced lesions, suggesting myelin recovery [72]. In another study, the MWF was found to be lower in both focal lesions and the NAWM of PPMS patients than controls, and the lower MWF was correlated with higher clinical disability [73]. Similar to other MR techniques, MWI is not specific to the myelin, and other processes, such as inflammation and edema, must be considered in assessing MWF [74].

Susceptibility Weighted Imaging (SWI)

The SWI takes advantage of differences in the magnetic susceptibility between tissues. It uses both the magnitude and phase of a gradient echo sequence to generate new imaging contrasts [75]. By utilizing the paramagnetic nature of deoxyhemoglobin, the SWI shows a great utility in imaging small vessels. The application of SWI is extended with its role in enhancing the contrast between WM and GM as well as water and fat, and in detecting iron in the brain. The SWI detects MS lesions as an area with a hypointense rim or as a hypointense nodule, and most lesions exhibit a central vein sign, indicating the involvement of vessels in lesion formation or evolution (41). Nonetheless, distinguishing paramagnetic and diamagnetic susceptibility merely based on SWI is

difficult [76]. Quantitative susceptibility mapping (QSM) is an MR technique that relates the spatial distribution of both susceptibility and frequency by deconvolution of MRI signal [77]. The QSM advances by providing more quantitative measures than SWI [77]. Both demyelination and iron deposition can increase tissue susceptibility as commonly seen in MS lesions, which are detectable by QSM [76]. One of the limitations about QSM is that it assumes the susceptibility being isotropic, but the susceptibility of WM is typically anisotropic with high directionality dependence [76]. The susceptibility tensor imaging (STI) technique may resolve this case. The STI measures tissue susceptibility in several directions relative to the main magnetic field and a susceptibility tensor can be derived for fiber tract reconstruction [76]. The shortcoming of STI is the need for brain rotation in the scanner that may not always be possible in practice [76].

Overall, Advanced MRI techniques hold considerable potential in detecting further details of brain microstructure but most of them mainly serve as research sequences in clinical studies or trials. Conventional MRI methods are still the mainstay in clinical MS imaging. While lack of specificity to MS pathology based on direct assessment of MRI signal intensity, conventional MRI combined with pertinent image analysis techniques may improve. Accordingly, the latter becomes the core theme of the research chapters of this thesis project. Nonetheless, to provide proof of concept evidence, this project also includes comparisons with two common advanced MRI methods: DTI and MTI (e.g. Chapter 3/Aim1). For either conventional or advanced MRI, the application of robust image pre-processing techniques are necessary to improve image quality and consistency.

3.3 Image Pre-processing Techniques

3.3.1 **Inhomogeneity correction**

The imperfection of image acquisition process causes a nonuniform low-frequency intensity variation throughout the image (Figure 2.6) [78]. Intensity inhomogeneity is prominent in high magnetic field MR imaging and results in various intensities for the same tissue at different locations within the image [78].

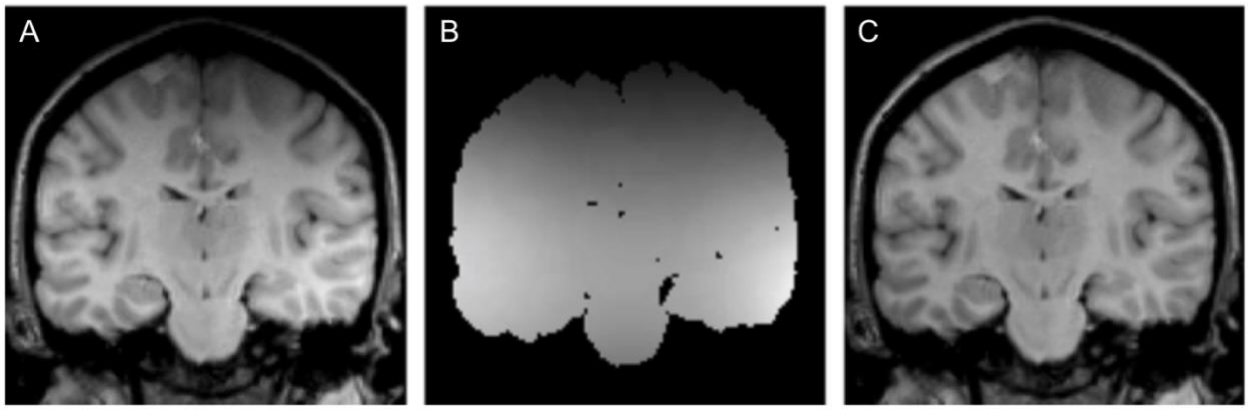

Figure 3.6. Intensity inhomogeneity correction in brain MRI. Shown are the original image with inhomogeneity artifact (A), the calculated field of inhomogeneity to remove (B), and the inhomogeneity-corrected image (C) (images adapted from [78]).

Various methodologies have been suggested in the literature for bias field correction [78, 79]. Nonparametric nonuniform normalization (N3) is one of the popular inhomogeneity correction algorithms. This approach iteratively finds the smooth multiplicative field of the tissue intensity distribution by maximizing the high frequency component of the distribution [80]. N4ITK is a modified version of N3 that improved its performance by substituting N3 bias field approximation with a robust B-spline approximation and a modified optimization algorithm [80].

3.3.2 **Brain extraction**

There are some non-brain tissues such as skull, eyes, skin, and fat in the source brain MR Images. The process of brain extraction removes these non-brain structures to improve the reliability of the subsequent image analysis steps such as lesion segmentation [81, 82] (Figure 2.7). One widely used brain extraction method is the brain extraction tool (BET), which is implemented in FSL software (Oxford, UK).

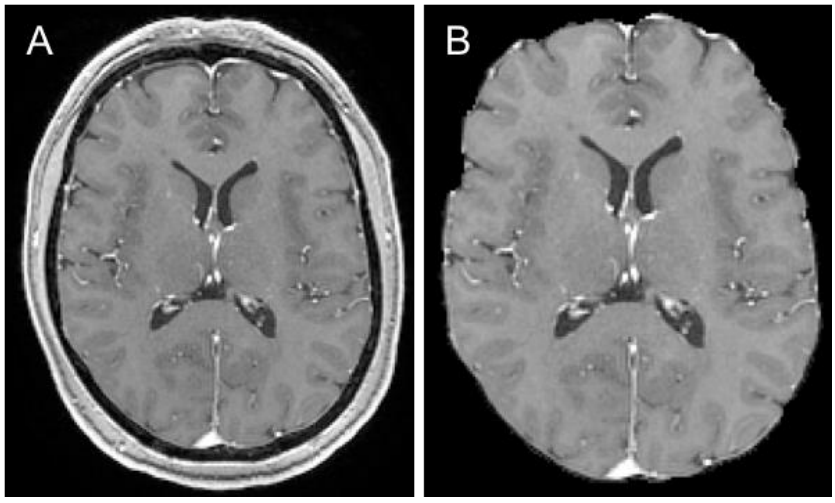

Figure 3.7. A brain extraction example acquired from a RRMS participant in a clinical trial of domperidone. Shown are the original axial post-contrast T1-weighted brain MRI (A), and the associated brain extracted image (B) achieved using the corresponding tool (BET) from an open source software FSL.

3.3.3 **Co-registration**

Image co-registration is aligning two or more images of the same view. The images may be taken at different time points, from different machines, and/or from multiple viewpoints [83]. Medical image registration seeks an optimal spatial transformation to adjust the feature points of two

images (secondary and reference) concerning the spatial position and underlying anatomical structures [84, 85]. Image co-registration procedures mainly consist of the following [83]: 1) Feature detection - finding distinctive features in the image, such as edges, contours, and corners; 2) Feature matching - assessing consistency between the detected features in the secondary and reference images using feature descriptors and similarity measurements; 3) Transform model estimation - estimating the parameters of the mapping function to match the secondary and reference images. The parameters are optimized by measuring the similarity and feature correspondence between the two images [83, 84]. Transformation models can be rigid or non-rigid depending on the number of parameters or the degree of freedom of the model [84]; and 4) Image resampling and transformation - transforming the secondary image by computed mapping function and proper interpolation techniques [83]. A sample registration of two MRI sequences is shown in Figure 2.8.

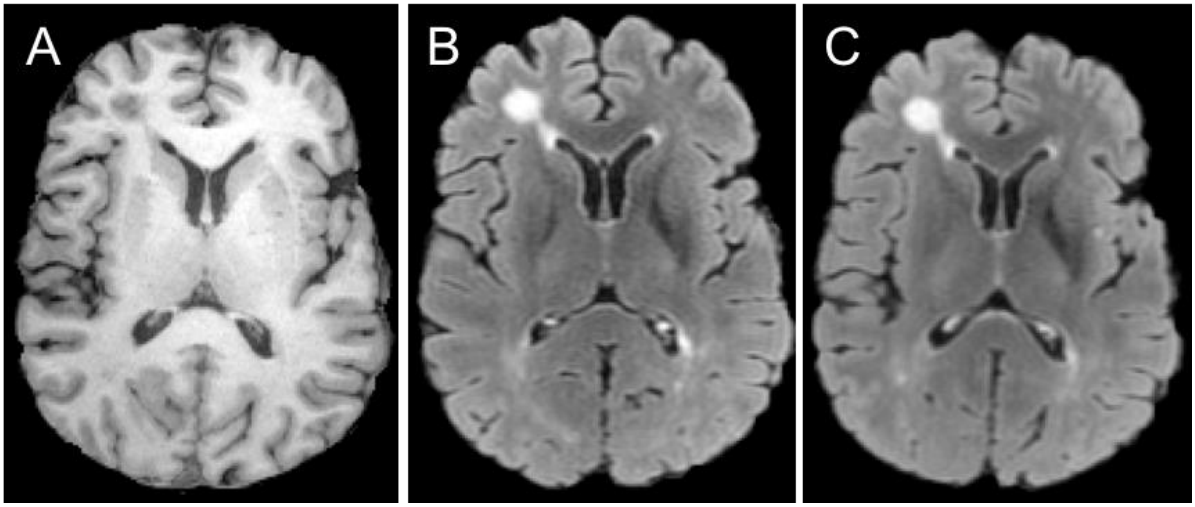

Figure 3.8. An image co-registration example between brain MRI sequences acquired from a RRMS patient. Shown are a pre-contrast T1-weighted MRI (reference) (A), FLAIR MRI (secondary) (B), and co-registered FLAIR (C) with alignment closer to the reference image.

3.3.4 **Denoising**

Image denoising is one of the fundamental techniques in image processing. Image denoising aims to recover an improved quality image from the noisy version of the image [86]. MR images can be corrupted by noise throughout the acquisition or transmission process [87]. Thermal noise is the predominant noise in MR images, represented by Gaussian and Rician distribution. Noise in MRI can be reduced by post-processing approaches [88]. Noise reduction methods in the spatial domain can be classified into two main groups – linear and non-linear filtering [89]. Gaussian and mean filtering are two linear filters widely used in image denoising. Non-linear filtering approaches perform better in edge-preserving with less blurring effect. They include anisotropic diffusion filtering [90], adaptive Wiener filter [91], median filter [92] and non-local mean filtering and its variants [93, 94]. The non-local mean filtering methodologies are very efficient in MRI noise reduction, particularly in the presence of Rician noise [89] as shown in the research chapters of this thesis.

3.3.5 **Normalization**

Different MR images may present different intensities, even if they are produced by the same scanner and protocol [95], because MRI instrumentation leads to the intensity variation of intra-scan and inter-scan images. Consequently, image normalization is applied to images before quantitative image analysis [96]. Significant image intensity variations might affect the image texture feature extraction and evaluation, and subsequently it can influence the reproducibility of the related research studies [97]. Image pre-processing techniques, including image normalization, are effective in minimizing the impact of inter-patient and intra-patient image intensity variation.

It has been shown that image intensity normalization enhanced the robustness of the textural features and the performance of the brain tumor grade classification [97].

3.3.6 **Eddy, motion, and susceptibility artifacts correction**

Eddy-current is induced in conductive materials of the MR scanner by rapidly changing magnetic fields, being more dominant in diffusion imaging. Eddy-current might affect gradient strength or direction, resulting in image distortions leading to misalignment between the captured images [98]. These distortions might affect the images by translation, scaling, and shearing that causes misregistration artifacts between conventional and diffusion MRI acquiring in a diffusion tensor imaging procedure [99]. During a long diffusion imaging acquisition time, the images are prone to motion artifacts. Another distortion related to diffusion imaging arises from the inhomogeneities in the magnetic field and is mainly due to susceptibility alteration within the object, known as susceptibility artifact [100]. In brain imaging, susceptibility artifacts are more prominent at the air/tissue interfaces. Susceptibility distortion leads to magnetic field inhomogeneity and affects the image's pixel position, resulting in mislocalization [101]. The artifacts mentioned above affect the accuracy, reliability, and reproducibility of diffusion-derived metrics and need to be corrected [100]. Several methodologies have been suggested for eddy-current and susceptibility distortion correction, including additional registration and transformation approaches, field mapping, and reversed-phase encoding [100, 101]. The Functional Magnetic Resonance Imaging of the Brain Software Library (FSL) provided the required tools to correct eddy, motion, and susceptibility artifacts using both graphical user interface and command-line option [101] (Figure 2.9).

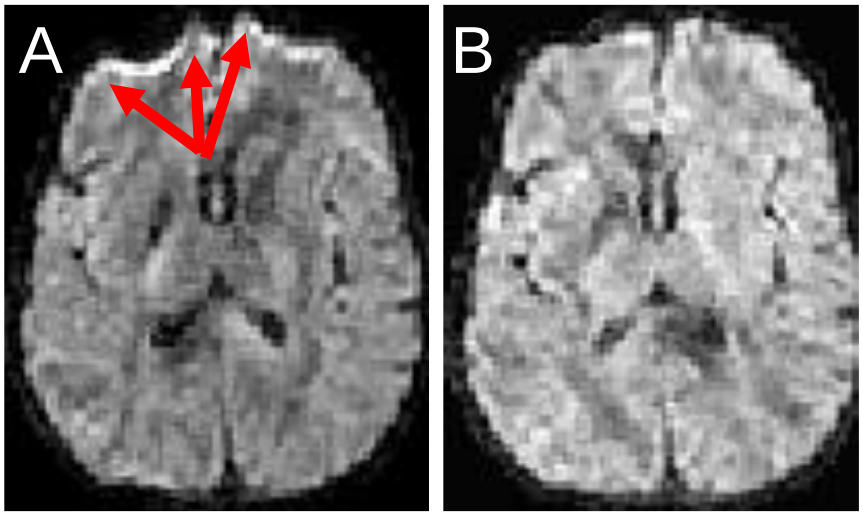

Figure 3.9. Susceptibility artifact in DTI acquired from a RRMS patient. Shown are the original image (A), where red arrows indicate distortion due to susceptibility artifacts, and the image with corrected eddy, motion and susceptibility artifact (B) with FSL (eddy and top-up correction).

3.4 Image Texture analysis

As noted above, MS is characterized by different pathological processes such as inflammation, demyelination, remyelination, and axonal damage. Such changes can jointly exist in the MRI of individual MS lesions or non-lesion areas, causing enormous heterogeneity in the distribution pattern of image signal intensity. However, assessing changes in the distribution pattern is challenging using human eyes. Texture analysis is a useful approach for identifying subtle structural changes that are not easily detectible on conventional MRI. With texture analysis techniques, we can extract valuable quantitative information through mathematical calculation with MRI [20]. Texture analysis is mainly classified into three common approaches – statistical, spatial frequency-based, and structural approaches, with the first two used primarily in MS studies.

3.4.1 **Statistical Approach**

This approach uses statistical parameters in the first or second order. First-order statistics include mean and variance, and second-order statistics include grey level co-occurrence matrix (GLCM) and run–length matrix (RLM) [14, 20]. The GLCM is widely used in image texture analysis in various conditions [102-104]. It calculates how often pairs of pixels with specific values and specified spatial relationships occur in an image (Figure 2.10). Quantitative statistical features are derived from the GLCM to measure image texture [105]. Contrast, dissimilarity, angular second moment (ASM), entropy, and correlation are some commonly extracted features from GLCM.

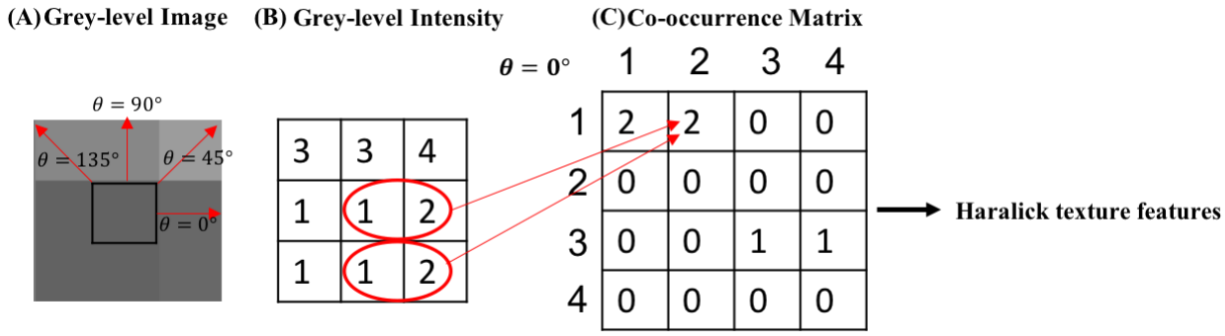

*Figure 3.10. An example of GLCM computation. Shown are a grey-level image (A), a 3× **3** matrix of the image intensity values (B), the calculated GLCM matrix for pixel distance=1, orientation=0°, and intensity level=4 (C).*

Contrast

Contrast refers to the non-linear weighted differences in image signal intensity between a pixel and its neighboring pixels in an image. This variable measures the extent of local variation in the image (texture/tissue coarseness) and is calculated by the square of grey level differences in the GLCM matrix [106]. Large local intensity variation leads to higher contrast values. GLCM

contrast is calculated by adding the multiplication of GLCM elements by a weighting factor. The weighting factor here is the square of the grey-level difference. So, the values increase exponentially from the main diagonal [107]. Contrast has been used as one of the practical GLCM features in different studies. In a study of brain cancer detection, contrast was used for classification of cancerous tissues [108]. In MS, a study found contrast as one of the most discriminant features in classifying the three tissue groups in MS and control – normal white matter, NAWM, and MS lesions [15].

Dissimilarity

Dissimilarity refers to the weighted differences between adjacent pixels (tissue heterogeneity) [108]. The absolute value of the grey-level difference is used as the weighting factor for GLCM dissimilarity calculation. It has similar output to contrast but with linear changes from the main diagonal [107]. GLCM features, including dissimilarity, have been effectively used to discriminate MS and control, based on their retinal nerve fiber layer computed from optical coherence tomography [109]. A recent study also involved dissimilarity and some other GLCM features to classify MS from healthy control [110].

Angular second moment (ASM)

The ASM, also called energy, represents the uniformity of the distribution of image signal intensity. This measure is calculated as the sum of squares of GLCM elements, which indicates image homogeneity [111]. The uniform spatial distribution of intensity values causes higher values of ASM [58]. The ASM has been used to quantify the structural changes in acute inflammation in muscles, showing that inflamed tissues have low ASM values. In general, it seems that injury

reduces tissue uniformity [112]. Another study used GLCM features to describe skin texture; among different GLCM features, ASM and entropy were most promising in reflecting skin tissue structure [113]. GLCM texture parameters, including ASM, were successfully used to differentiate MS lesions from the NAWM [114].

Entropy

Entropy is originally a thermodynamic concept used in image processing to measure the degree of disorder or randomness of intensity distribution [113]. Entropy measures how much various information the image contains [111]. A more disordered texture has higher entropy [115]. An MRI texture analysis study of breast cancer revealed that the entropy feature from GLCM is the most discriminant feature for breast cancer subtype classification [116]. In a different study, entropy has also shown a high clustering ability to characterize myocardium muscle [117].

Correlation

Correlation refers to the linear dependency of grey levels between neighboring pixels specified, which measures tissue irregularity. A constant image value has a correlation value of one, which implies no correlation [107]. One study used GLCM correlation, in addition to contrast and entropy, in combination with a convolutional neural network for MS lesion detection [118]. A recently utilized supervised classification, a gradient tree boosting, algorithm and FLAIR MRI combined with RLM and GLCM features, including correlation, achieved high classification accuracy (over 98%) in identifying active MS lesions [119].

3.4.2 **Spatial Frequency-based Approach**

Each distinct image texture pattern also has a unique frequency distribution. The rapid and slow intensity changing patterns in an image reflects its frequency content. The Fourier transform is primarily used to describe the overall frequency characteristics of an image. However, Fourier transform cannot extract local frequency information. In addition, the definition of the frequency of the grey level change is scale dependent. Wavelet transform employs a multi-scale approach and is location discernable, and therefore helps characterize structural changes in heterogeneous tissues. However, the high computation cost of Wavelet transform is a drawback. The Stockwell transform is another advanced frequency-based approach that gives a unique frequency spectrum at each pixel. The polar form of Stockwell transform (PST) is rotationally invariant and less sensitive to the motion artifact present in medical images than the Stockwell transform [20]. PST could differentiate coarse tissue such as lesions from fine tissue like NAWM [20].

3.5 Image Classification

3.5.1 **Machine learning algorithms**

Classification is a fundamental process in data analysis. Several machine learning algorithms have been developed for this purpose [120]. Machine learning is the strategy that constructs computer algorithms to perform a particular task using given data to provide a specific outcome [121]. Classification is a kind of machine learning algorithm used to build a model by labeling different classes in the dataset or predicting the classes in a new given dataset [120]. Classification tasks can be categorized in three main approaches: supervised, unsupervised, and semi-supervised.

Supervised machine learning

This approach uses labeled data to train the algorithm. The dataset is partitioned into train and test groups. By learning the pattern of data from the training set, the model is built to predict the class of data in the test set [122]. Some of the most common supervised machine learning methods are described here.

Decision tree

Decision trees use tree shape representation of the classification problem, including nodes and branches. Each node represents a feature, and each branch represents a decision. These algorithms perform classification by continuously splitting the data based on their feature values [123, 124].

Random forest

A random forest (RF) is an ensemble of many — ideally uncorrelated — decision trees [125]. A bootstrap sample with replacement from the original data, and a random sample of features at each split are used to construct individual trees [126]. Each tree performs a classification or regression task, and the results of an RF represent the aggregate (majority vote or averaging) outcome from all trees [127, 128]. A critical parameter in RF is out-of-bag error. It is calculated using the out-of-bag samples that have not been used for constructing tree algorithms, and the measure can be considered as an internal validation for those trees. The overall out-of-bag error of the RF will be the average prediction error calculated using the trees with all out-of-bag samples [126].

Support vector machine

Another commonly used machine learning algorithm is support vector machine (SVM). The SVM can be used for the classification and regression problems [129]. SVM identifies margins between different classes in the dataset. Maximizing the margin or increasing the distance between classes reduces the classification error [122, 130]. The SVM can perform either linear or non-linear classification tasks, with use of non-linear kernel functions for the latter [131].

Unsupervised machine learning

Unsupervised machine learning algorithms do not rely on any labeled data. Unsupervised algorithms attempt to discover patterns and features without training with labeled data [132]. Then they use the learned rules to classify patterns and trends of new data. This type of methods are primarily useful for clustering and feature reduction [122].

K-means clustering

K-means is one of the most common unsupervised learning algorithms for data classification. It classifies the data through a pre-determined number of clusters. Several methods can be used for choosing k for the k-means algorithm, including using the number of expected classes in the data or data visualization [116]. For example, Martinez-Heras et al. considered k=2 to cluster two types of MS lesions based on the severity of the changes in their diffusion measurements [133]. The algorithm identifies k centers per cluster, and when algorithm completes, every data point is allocated to the nearest center [122, 134].

Principal component analysis

Principal component analysis (PCA) identifies the principal components of the data, which are linearly uncorrelated variables [122]. The first principal component is in the direction of the data demonstrating the most significant spread. The second principal component is the direction of the second largest variation orthogonal to the first component [135]. PCA is typically known as a dimensionality reduction approach that reduces the number of features to a smaller set containing the most information, resulting in faster and simpler computation [136].

Semi-supervised machine learning

Semi-supervised machine learning is an approach that combines supervised and unsupervised algorithms. It might be used in classification tasks where un-labelled data is available, and providing labeled data from the unlabeled data is tedious. This approach combines a small number of labeled data with many unlabeled data to train the model [122].

3.5.2 **Percentile approach**

A percentile is a score used in statistics to split the data into two sets, indicating the value below or above a certain percentage. Percentile statistics were revealed as promising in classifying tissue types or disease activity in different studies, including those in MS [68, 137, 138]. For example, a previous study successfully identified highly repaired and damaged tissues in MS using the $25\%^{ile}$ and $75\%^{ile}$ thresholds of the MTR values [139]. A recent study utilized different percentiles of myelin water fraction (MWF) beside lesion volume, cortical thickness and thalamic volume to differentiate RRMS from progressive MS patients [140]. They reported $50\%^{ile}$ MWF, $25\%^{ile}$ MWF, $75\%^{ile}$ MWF, and $75\%^{ile}$ thresholds of lesion volume as the most informative features

selected by PCA [140]. It has been suggested that the coarseness of MRI texture was significantly greater in MS lesions with tissue damage than in those with repair [17, 141], indicating that lower and higher percentile of texture values may be used to identify injury and repair in MS lesions. Therefore, percentile statistics can be implemented to determine lesion severity and classify MS lesion types based on the predefined percentile thresholds.

3.5.3 **Z-score-based approach**

Z-score is a numerical measurement that indicates the relationship of a data point to the mean of the dataset. It represents how many standard deviations a data point is above or below the mean. Z-score in MS is often used to compare cognitive impairment and disability between groups [142, 143], or compare MS and control groups. One study used z-score for analyzing microstructural changes of RRMS brain tissues. They assessed tissue alteration in NAWM and lesions compared to controls and found significant changes in mean T1 relaxometry, T2 relaxometry, T2* relaxometry, and MTR, suggesting edema, demyelination, and tissue degeneration [144]. Another study calculated normalized z-score of Jacobian determinant values to compare the brain volume between children with MS and age- and sex-matched healthy controls [145]. Their results showed that MS subjects revealed a significant volume reduction in the thalamus and the splenium of the corpus callosum, as well as significant enlargement in the ventricles of the brain compared to control [145].

3.6 Summary

MS is an inflammatory demyelinating disease of the central nervous system. It is characterized by different pathological components, including demyelination and remyelination. MRI is one of the

fundamental imaging modalities for studying neuropathology. However, MR images are prone to different noises and artifacts, which should be minimized prior to quantitative data analysis [110]. There are different methodologies available for image pre-processing as discussed in this chapter. Similarly, there are also different approaches for classifying the types of tissue pathology in MS, including both supervised and unsupervised algorithms. This research project focuses on development and validation of image processing and analysis techniques for characterizing brain MS pathology types, particularly regarding injury and repair such as de- and re-myelination in lesions.

CHAPTER 3: Texture analysis in brain T2 and diffusion MRI differentiates histology-verified grey and white matter pathology types in multiple sclerosis

4.1 Background

MS pathology involves different types of tissue abnormalities. Accurate evaluation of MS pathology is crucial for a better understanding of disease activity and treatment impact. However, due to the heterogeneity of MS pathology, it is not intuitive to classify tissue pathology types using conventional methods. As discussed in Chapter 2, texture analysis has been effectively used to differentiate normal from abnormal structural alterations in various diseases, including MS. Furthermore, combining texture analysis with machine learning algorithms may improve the ability to differentiate tissue types. The goal of this chapter was to investigate whether and how this approach could distinguish all common types of MS pathology involving both gray and white matter of MS subjects, including de- and re-myelinated lesions, based on histology-informed postmortem MRI. In addition, for systemic understanding, this study also included recognized metrics of advanced MRI. The content of this chapter has been published as a manuscript [146].

4.2 Introduction

Multiple sclerosis (MS) is a complex disease of the central nervous system impacting >2.8 million people globally, many of whom end up with paramount disability [147]. MS pathology is highly heterogeneous presenting with various injury types that involve both grey and white matter,

including inflammatory demyelination, neuronal loss, and axonal degeneration [148]. Tissue repair, such as remyelination, also occurs in MS but it is incomplete and not present in all lesions [148]. Further, while the grey matter possess inherently lower myelin than the white matter, remyelination seems to be more abundant in the grey than white matter, and grey matter lesions also contain several subtypes [149], deserving further investigation. Accurate assessment of tissue pathology is critical for optimal assessment of both disease activity and treatment responses for all MS patients.

Magnetic resonance imaging (MRI) is a pivotal tool for MS measurement. However, regardless of the high sensitivity, conventional MRI is typically nonspecific for MS pathology [150]. Advanced MRI may improve in this regard , including magnetization transfer (MT) imaging (e.g. MT ratio, MTR), myelin water imaging, and diffusion tensor imaging (DTI) [150]. For instance, MTR can detect changes associated with de- and re-myelination, and to a lesser extent, inflammation and edema [150]. DTI-based fractional anisotropy (FA) has shown various correlations with myelin and axonal density [151]. Nonetheless, the utility of these advanced measures for distinguishing different pathology types in MS requires further validation.

Previous research has shown that advanced analysis of the ‘texture’ of MRI can increase its sensitivity and specificity to tissue pathology, including voxel-based texture analysis of DTI [18]. Texture analysis evaluates the distribution pattern of image voxels that reflects the structural integrity of the underlying tissue [106, 152]. Fozouni et al. found that voxel-wise analysis of diffusion texture across diffusion directions is more accurate than traditional DTI measures of brain structure. In MS, texture analysis using standard MRI in vivo detects lesion activity [141];

differentiates persistent from transient T1 black holes [17]; and distinguishes lesions from normal and normal-appearing white matter (NAWM) [16]. In addition, MRI texture measures have shown strong correlates with myelin integrity in both post-mortem and animal studies of MS [27, 153]. Together with machine learning algorithms, texture analysis of standard MRI from post-mortem brains has also classified brain tissue types, including white matter lesions versus non-lesion areas in MS [19]. However, robust methods for differentiating different brain pathology types in MS have not been established using texture analysis, with or without machine learning techniques. Further, to our knowledge, there is no evidence showing the relative ability of advanced versus conventional MRI measures in a machine learning setting for classifying MS pathologies.

The goal of this study was to address the unmet needs mentioned above. Specifically, we aimed to investigate the ability of MRI texture measures to differentiate histology-confirmed grey and white matter tissue types in MS using post-mortem brain MRI, as compared to MTR and FA. This was facilitated by the development of multiple new image preprocessing and analysis approaches, as well as new machine learning models.

4.3 Materials and Methods

4.3.1 Samples

There were 27 formalin-fixed brain samples, one each from 15 MS patients (7 female), and 12 from 4 matched control subjects (all female). The MS cohort included 11 secondary progressive MS, 1 primary progressive MS, and 3 unknown diagnoses. The mean (± standard deviation) age was 68.5±12.7 years for MS patients and 70.5±8.5 years for controls. Disease duration in patients was 29.1±13.2 years. All brain samples were coronally cut as 10-mm-thick slices prior to imaging

with a post-mortem delay of 5.56±2.27 hours. This study was approved by the Institutional Ethics Board. Informed Consent was obtained from each participant prior to death.

4.3.2 Tissue type definition in histology

Post-imaging, the brain slices were paraffin embedded and prepared for histology. Given the purpose of this specific study, histological assessment focused mainly on myelin characteristics achieved by immunostaining with myelin proteolipid protein (PLP). Analyses for other pathological changes such as inflammation were not included and out of the scope of the current study and reported somewhere else respecting cortical inflammation [154]. Briefly, for this thesis, the brain samples were sliced into 10-mm-thick coronal sections. Five of the sections were chosen based on presence of lesions on MRI and were transferred to a custom-made brain slice holder that was compatible for imaging using a head coil. The brain slices were then cut into half to show the scanning plane [155], and the tissue cutting surface was photographed to assist histology and MRI matching, which was further enabled by the use of white matter lesion locations and anatomical landmarks such as grey and white matter borders, ventricles, sulci, and gyri [155, 156]. Regions of interest (ROIs) were identified on anatomical MRI using an established image processing tool (MIPAV, NIH, USA) and then were populated to histological samples [154, 157].

The initial histology types were identified as: demyelinated lesions (complete loss of myelin stain); diffusely abnormal white matter (DAWM, partial loss of myelin stain); normal grey and white matter (intact myelin stain, to match the normal appearing tissues in MRI: NAGM and NAWM), and remyelinated lesions (shadow plaques). Specifically, given the difficulty of differentiating incomplete demyelination and partial remyelination, particularly with PLP, an area of

remyelination was made when thin, irregularly formed myelin sheaths were observed [158]. This step of analyses provided seven ROI types, four in the white matter: NAWM, DAWM, remyelinated lesion (remWM), and demyelinated lesion (demWM), and 3 in the grey matter: NAGM, remyelinated lesion (remGM), and demyelinated lesion (demGM).

Subsequently, the demGM was further divided into four subtypes as reported previously [159]. These were: type I, affecting both grey and white matter; type II, within the cortex; type III, subpial; and type IV, extending across the cortex. Finally, grey and white matter ROIs in control subjects with anatomical matching to the NAWM and NAGM regions of MS were identified for comparison. There were no abnormalities detected in the control specimens other than age-related changes. Overall, there are eleven ROI types from MS and normal brain tissues.

4.3.3 Imaging protocol

All brain slices underwent both anatomical and advanced MRI using a 7T BioSpec scanner (Bruker BioSpin USR70/30, Ettlingen, Germany) and an 8.6-cm-diameter radiofrequency transmit/receive coil (model 1P T12053V3). At imaging, the brain slices were placed in 10% buffered formalin within a rectangular plastic tissue container with slice surfaces aligned with the corresponding imaging planes. Anatomical imaging focused on T2-weighted MRI. It was acquired using a two-dimensional multi-echo spin-echo sequence, with repetition time (TR) = 4000ms, echo time (TE) = 19.1/38.2/57.3ms; field of view (FOV) = 100×80mm^2; matrix = 1000×800; and voxel size = 0.10×0.10×1mm^3. The imaging time was 5.20 hours. Advanced MRI included MT and diffusion imaging. Diffusion MRI used a twice-refocused spin-echo sequence with 3 b values (0, 1500, and 3000s/mm2) and 30 gradient-encoding diffusion directions. The TR = 5000ms; TE = 55ms; FOV

= 100×80mm^2; matrix = 50×40; and voxel size = 2×2×1mm^3. The acquisition time was 1.26 hours. MT imaging used a three-dimensional gradient-recalled echo sequence with and without a saturation pulse. The TR = 40.9ms; TE = 12.9ms; FOV = 100×80 mm^2; matrix = 1000×800; voxel size = 0.10×0.10×1mm^3; offset frequency = 3kHz; and MT pulse flip angle α = 850°. The imaging duration was ~2 hours.

4.3.4 Image preparation

Image preprocessing included 5 major steps. These were: 1) linear co-registration between all parametric maps and the reference images, which were T2-weighted MRI, using the FLIRT algorithm from FSL (Oxford, UK) per subject; 2) N4 bias field correction for T2-weighted MRI employing the ANTs tool [160]; 3) manual brain extraction to remove image background using ImageJ (version 1.50i, NIH, USA); 4) intensity normalization to the range 0-255; and 5) noise reduction. The last three steps were applied for both T2-weighted MRI and DTI.

Noise reduction in step 5 above used different approaches to account for different types of noises involved. T2-weighted MRI was expected to contain mainly Gaussian white additive and salt and pepper noises [92], which were processed by applying the mean and median filters included in ImageJ (NIH, USA). These filters work based on a sliding window approach. For each windowed region, its center value was substituted by the mean or median value of all pixels in the window and repeated for all windows. The mean filter is effective for eliminating Speckle (Gaussian) noise, whereas the median filter can remove different types of noises, including Gaussian and salt and pepper noises [92], as the latter is non-linear and therefore has increased edge-preserving effect. Diffusion images contained primarily Rician noise [161], which was corrected by using an

adaptive soft coefficient matching (ASCM) filter [162]. Subsequently, to increase the angular sampling and texture resolution of diffusion, the number of diffusion gradient directions was increased from 30 to 90 using an established interpolation approach [163]. Prior evidence suggested that texture values were more accurate with larger number of diffusion directions and texture measures based on 90 directions were found to be stable and competitive in assessing brain microstructure in animals [18]. This technique performed up-sampling of diffusion directions based on spherical harmonics functions and the Q-ball model; both are commonly used in improving the estimation of diffusion orientation distribution function [163]. The image processing pipelines were shown for T2-weighted and diffusion-weighted MRI as seen in Figure 3.1.

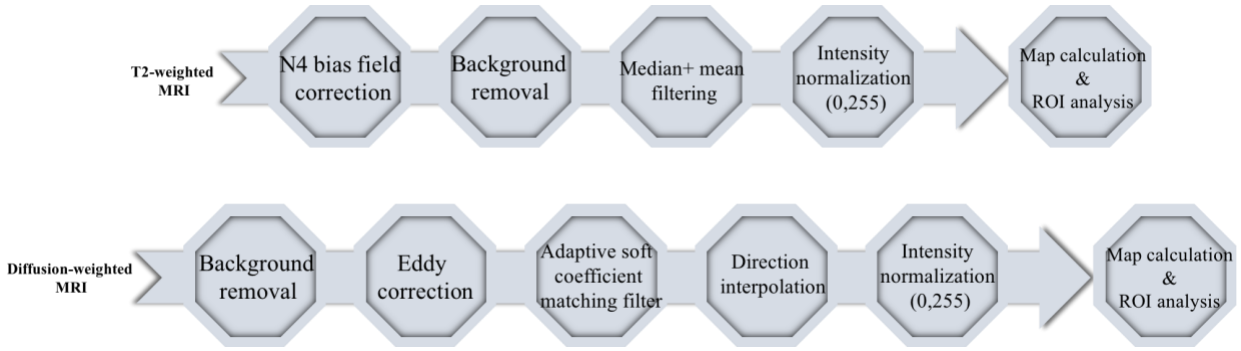

Figure 4.1. Image processing pipeline for T2-weighted (top row) and diffusion-weighted MRI (bottom row) scans. The MR images were pre-processed with the required steps and the final texture maps were calculated using the pre-processed MR images.

4.3.5 Image texture analysis

Texture analysis with T2-weighted MRI

Texture analysis for the prepared T2-weighted images used the grey level co-occurrence matrix (GLCM) method based on implementation in the scikit-image library in Python (version 2.7) [164]. The GLCM calculates the occurrence frequency of a pixel relative to its neighboring pixels at a specified distance (d) and orientation (θ) in an image. Typically, the method evaluates pixel relationships in 4 orientations: 0°, 45°, 90°, and 135°. To detect fine image texture, a small distance is preferable [165]. Our analysis applied d=1, covering all 4 directions. At each direction, the GLCM provided 14 features [106]. However, due to the known fact of inter-feature correlations, we focused only on 5 recommended features [166]: contrast, dissimilarity, angular second moment (ASM), entropy, and correlation. This included the average and maximum texture of the 4 directions per feature, as well as entropy calculated using a sliding window approach (entropy filter). Within a window, the latter used the same equation as defined for the typical entropy in GLCM. Contrast detected local intensity variations in an image, indicating tissue coarseness. Dissimilarity assessed differences between adjacent pixel values thereby indicating tissue heterogeneity. The ASM measured the similarity between pixel values, which highlighted tissue homogeneity. Entropy examined the randomness of pixel values, indicating tissue complexity. Finally, correlation assessed the dependency between neighboring pixels, suggesting tissue irregularity [106, 108]. Furthermore, to assess how image resolution impacts texture outcomes, T2-weighted images from three MS subjects who had the most ROIs were further investigated. These images were down-sampled from 800x1000 to a clinical equivalent matrix size of 320x400 (image resolution also changed from 10 to 1 pixel/mm). The resulting texture outcomes were compared between original and down-sampled images using Wilcoxon rank sum test.

Texture analysis with diffusion MRI

Diffusion texture analysis also used the GLCM theory, but it followed a new, direction-based approach [18], where each pixel was associated with a specific vector of diffusion values across directions (Figure 3.2). This calculation used the lower b value (b = 1500s/mm^2) data, as this option provided a greater anatomical contrast and appeared less noisy than the higher b value data according to our preliminary experiments. Based on diffusion values from all 90 directions per pixel interpolated from the original DTI, we computed 2 new texture features: diffusion ASM and diffusion entropy. This analysis excluded the other GLCM features as they all required more neighboring pixel information [106] than were available here from individual vectors.

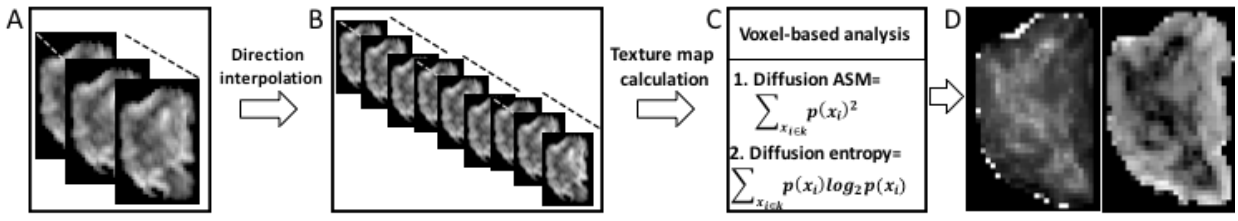

Figure 4.2. Diagram of directionality upsampling and texture analysis for diffusion MRI. The number of diffusion directions were interpolated from 30 (A) to 90 (B) using the theory of spherical harmonics and Q-ball model. Texture analysis was done across the interpolated diffusion directions per voxel using the equations (C) as defined in the GLCM for 2 parameters (D): diffusion angular second moment (ASM, left), and diffusion entropy (right). Shown are coronal sections obtained from the anterior part of the brain. Note: $\boldsymbol{p(x_i)}$: probability of a diffusion value repeating across gradient directions; $\boldsymbol{x_i}$: diffusion values in each direction.

4.3.6 MTR and DTI assessment

All quantitative imaging maps were calculated for the whole image initially. MTR calculation used this equation: $(M_0 - M_s)/M_0 * 100$, with M_0 and M_s representing non-saturated and saturated MT signal, respectively [159]. DTI analysis focused on FA, as it was one of the most frequently used and promising DTI metrics [151]. FA computation used the FDT Toolbox (FDT) included in FSL based on our interpolated 90-direction data. Eventually, mean ROI values were used in subsequent analyses to minimize the impact of differences in ROI size.

4.3.7 Tissue type classification based on all available imaging features

To assess the likelihood of classifying different tissue types, we started with all available imaging measures (texture, MTR, and FA) using a random forest (RF)-based machine learning method. The RF is an ensemble of many, ideally uncorrelated, decision trees [125]. Each tree performs a classification or regression, and the aggregate outcome from all trees achieved by majority vote or averaging highlights the final results of a RF [128]. Our RF classifiers contained 500 trees each. Each classification was repeated 10 times based on a 10-fold cross validation scheme, with 9 folds of the data for training and 1 (one) fold for testing each time. For tissues that had a relatively small sample size (e.g., remWM and DAWM), a reduced number of folds (6 and 9) was used instead of 10 to keep individual fold sizes equivalent across experiments. To explore inter-patient variability, we also performed leave-one-out analyses on a patient basis using a different RF, for three example groups: across all four WM tissue types, three GM tissue types, and between de- and re-myelinated lesions from both grey and white matter. Model evaluation used recognized metrics including accuracy, sensitivity, and specificity where applicable. Performance comparison between classifiers used the kappa statistic [167], which measured differences between the observed

accuracy and random accuracy; the higher the Kappa, the better performance the classifier. This study defined 5 kappa criteria: 0.01–0.20, 0.21–0.40, 0.41–0.60, 0.61–0.80, and 0.81–1.00, reflecting minimal, fair, moderate, substantial, and almost perfect agreement, respectively [167].

In addition, as our data was not entirely balanced between classes initially, we performed another set of tissue classifications based on 'balanced data' achieved by adjusting sample weights in associated classes for comparison. Several other approaches including oversampling or undersampling are also capable of handling imbalanced data, but these methods could cause artificial data or data loss and therefore are less favorable than sample weight adjustment [168]. In this study, we adjusted data balance by assigning higher weight to the minority class and lower weight to the majority class. Specifically, for class (a), its weight was calculated as: total number of samples / (number of classes* number of samples in class (a)) [169]. Classifier comparison used the same criteria set above, based on Kappa statistic.

Further, using the balanced data approach, we also developed new multi-label classification models for predicting unseen data as an additional evaluation step. This involved 4 RF models for all associated multi-label grey and white matter tissue groups. In each classification, the data was split into training and testing at a ratio of 70:30. Model development was done through cross validation used the training data, which was further split into 3 to 8 folds depending on sample size. Model evaluation used the corresponding held-out testing dataset.

4.3.8 Feature selection

Following the classifications, we performed feature ranking using a recursive feature elimination (RFE) method [170]. In brief, the RFE started with a RF built on all variables. After a classification procedure, the importance of each variable was defined based on the 'error index' associated with individual variables, and the variable of least importance was removed. After each classification step, a new RF model was generated using the remaining variables. This process repeated until a single variable or a minimum subset of variables were left in a model [170]. The performance of a RF was estimated at each iteration through RFE based on out-of-bag samples, which were the held-out data for model testing. Eventually, the feature subsets providing the smallest classification error (highest RFE accuracy) were selected [171]. Finally, while RFE was performed for each classification, only features associated with RF models showing moderate to almost perfect kappa accuracy were evaluated in subsequent analyses.

4.3.9 Comparison of classifications based on different imaging modalities

To compare the utility of different types of imaging features, we developed RF models for both binary and multi-label classifications using features from each modality alone. Specifically, we compared MTR with FA and with top-performing MRI texture features, with each feature fed into the model separately. Model development followed similar procedures as described above (Section 2.7), followed by accuracy and Kappa assessment.

4.3.10 Group comparison of tissue types based on selected imaging features

Group comparisons included all combinations of grey and white matter tissue groups identified above and all the associated RFE features. Tissue type comparison used one-way Kruskal-Wallis

to accommodate non-Gaussian distribution of the features, followed by correction for multiple comparisons using the Dunn test, where $p<0.05$ was considered significance. Statistical analyses were performed using R (version 3.6.3) [172].

4.4 Results

4.4.1 Sample outcomes

There were 435 ROIs examined from MS patients. Each patient had 4–123 ROIs, 2–82 from the grey matter, and 1–41 from the white matter (Table 3.1). The control subjects had 160 ROIs (95 grey matter and 65 white matter ROIs), ranging 7–23 per subject. The ROI size ranged 160–4669 pixels in grey matter lesions, and 229–1264 pixels in white matter lesions. Texture analysis generated 33 feature maps per subject: 31 from T2-weighted MRI [5 GLCM features X 6 choices each (4 directions + 2 directional average and maximum) + entropy filter], and 2 from DTI. Together with MTR and FA, there were 35 imaging features in total per ROI for further assessment (Figure 3.3).

Table 4.1. Number of regions of interest by tissue type in each MS brain sample examined.

MS case	1	2	3	4	5	6	7	8	9	10	11	12	13	14	15	**Total**
NAWM	1	3	4	-	2	1	2	1	1	18	1	1	1	1	1	**38**
DAWM	1	1	-	1	1	1	1	-	1	1	1	-	1	-	-	**10**
WML	-	1	1	-	1	-	-	1	-	22	3	1	-	-	33	**63**
NAGM	1	1	1	1	1	6	1	1	7	17	-	15	1	9	1	**63**
GML	4	12	12	2	1	8	-	6	4	65	19	33	3	14	78	**261**
Type I	-	8	-	2	-	2	-	-	-	33	-	3	-	2	20	**70**
Type II	3	1	3	-	-	-	-	-	1	2	-	2	1	2	3	**18**
Type III	1	2	4	-	1	3	-	2	2	12	4	11	2	4	29	**77**
Type IV	-	1	2	-	-	1	-	1	1	18	13	17	-	6	24	**84**

Note: NAWM: normal appearing white matter; DAWM: diffusely abnormal white matter; WML: de- and re- myelinated white matter lesions; NAGM: normal appearing grey matter; GML: demyelinated grey matter lesions; Type I-IV: four types of GML.

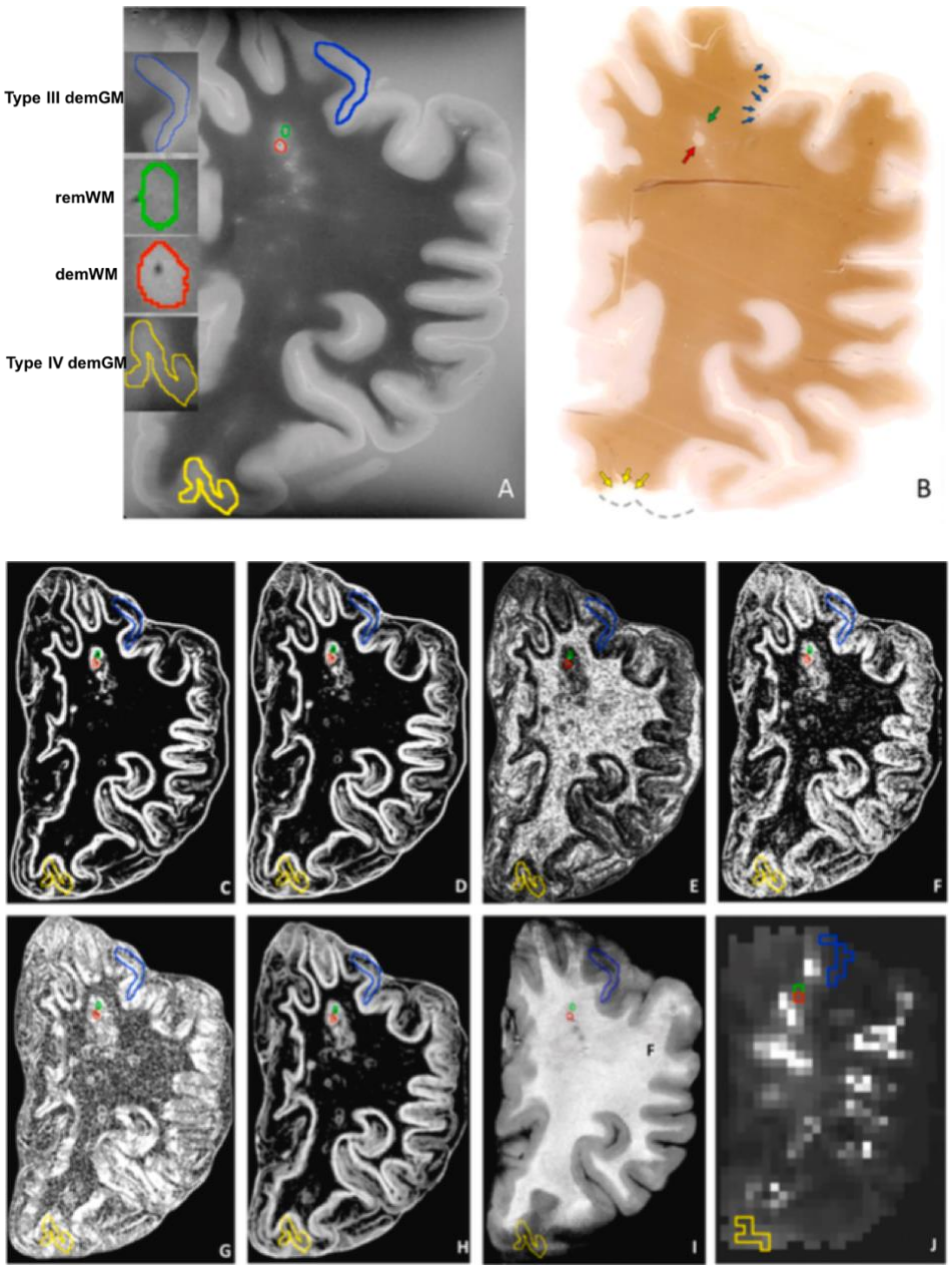

Figure 4.3. Example images and feature maps examined in this study. Top panel shows an T2-weighted MR image from a coronal brain section along with example regions of interest (color outlines, A), and the corresponding histology image and tissue regions (arrows) stained with Proteolipid protein for myelin (B). Bottom panel shows the calculated imaging feature maps. In the top row (C-F), they are: T2-contrast, T2-dissimilarity, T2- angular second moment (ASM), and T2-entropy. In the bottom row (G-J), they are: T2-correlation, T2-entropy filter, magnetization transfer ratio (MTR), and fractional anisotropy (FA). All direct GLCM features (the first 5) shown are the mean from all 4 directions computed.

4.4.2 Tissue classification results based on all available features

Model performance varied across tissue classification groups. Based on all possible combinations of grey and white matter ROI types in MS and control subjects, there were 20 RF groups, with each containing 2-4 tissue types. Without adjustment of data balance, 13 of 20 RF models achieved moderate to almost perfect kappa performance (Table 3.2; Supplementary Figure 3.1). In general, the classification of white matter tissue groups performed better than grey matter groups (accuracy = 0.85-0.97; kappa = 0.76-0.94 versus accuracy = 0.59-0.89; kappa = 0.41-0.60). Within the white matter, classification between NAWM and demWM was the best, followed by DAWM versus demWM, and then NAWM versus DAWM. The classification between MS NAWM and normal white matter also achieved a high accuracy of 0.83 and kappa of 0.67. Regarding the grey matter, classification between Type I and Type III demGM was the best, followed by NAGM versus demGM, and among NAGM, remGM, and demGM. Further, classification between demyelinated and remyelinated lesions from both grey and white matter achieved substantial performance (accuracy = 0.86; kappa = 0.55). The sensitivity and specificity of the models showed a similar trend except for Type 1 versus Type II demGM lesions, which had the highest sensitivity (Supplementary Table 3.1). Additional tests using leave-one-out models by patient revealed comparable performance: the classification accuracy and kappa were 0.84 and 0.75 respectively among white matter tissue groups (NAWM, DAWM, remWM, and demWM), 0.84 and 0.47 among grey matter tissue groups (NAGM, remGM, and demGM), and 0.85 and 0.51 between the joint de- and re-myelinated lesion groups from grey and white matter.

Based on data balanced with sample weight adjustment, the RF models showed a slight improvement in multiple evaluation metrics in some tissue groups, but the overall performance was essentially similar to that on data without balance adjustment (Supplementary Table 3.2).

In predicting unseen data, the newly developed multi-label models achieved an equivalent performance to the corresponding cross-validation models noted above. Specifically, the 4-label white matter model performed the best that had a substantial Kappa. It was followed by the 4-label de- and re-myelinated grey and white matter lesion model and then the 3-label grey matter tissue model; both showed a moderate Kappa. The 4-label demGM lesion model had the lowest performance, with kappa below the moderate cut-off (Table 3.3).

Table 4.2. The performance of RF models and RFE-selected features for models with moderate to perfect Kappa using data without balance adjustment.

Moderate-perfect Kappa groups	**Accuracy**	**Kappa**	**RF-RFE selected features**
NAWM/demWM	0.97/0.05	**0.94**	T2-contrast, FA
DAWM/demWM	0.96/0.08	**0.83**	T2-contrast, T2-dissimilarity
NAWM/DAWM/remWM/demWM	0.85/0.05	<u>0.76</u>	T2-contrast, T2-dissimilarity
NAWM/DAWM	0.92/0.11	<u>0.72</u>	T2-contrast, T2-ASM, T2-Entropy filter
Normal WM/NAWM	0.83/0.1	<u>0.67</u>	T2-entropy filter, Diffusion ASM & entropy, MTR
Type I/Type III	0.80/0.10	0.6	T2-correlation, T2-entropy filter
NAGM/demGM	0.89/0.05	0.56	T2-contrast, T2-dissimilarity, T2-entropy filter,
remWM/demWM/remGM//demGM	0.86/0.03	0.55	T2-contrast, T2-dissimilarity, MTR
NAGM/remGM/demGM	0.85/0.04	0.49	T2-contrast, T2-dissimilarity, T2-entropy filter
Type III/Type IV	0.72/0.10	0.44	T2-dissimilarity, T2-ASM, T2-correlation
Type I/Type II	0.86/0.09	0.42	T2-ASM, T2-correlation
Type I/Type IV	0.71/0.10	0.42	T2-correlation, Diffusion entropy
Type I/II/III/IV	0.59/0.09	0.41	T2-contrast, T2-ASM, T2-correlation

Notes: RF-RFE: random forest-recursive feature elimination; and Std: standard deviation. The kappa values represent: Moderate accuracy: 0.41–0.60; Substantial accuracy (underlined): 0.61–0.80; and Almost Perfect accuracy (bold): 0.81–1.00.

Table 4.3. Multi-label classification accuracy and Kappa on unseen data

Tissue groups	Accuracy	Kappa
NAWM/DAWM/remWM/demWM	0.89	0.79
remWM/demWM/remGM//demGM	0.87	0.53
NAGM/remGM/demGM	0.85	0.56
Type I/II/III/IV	0.48	0.24

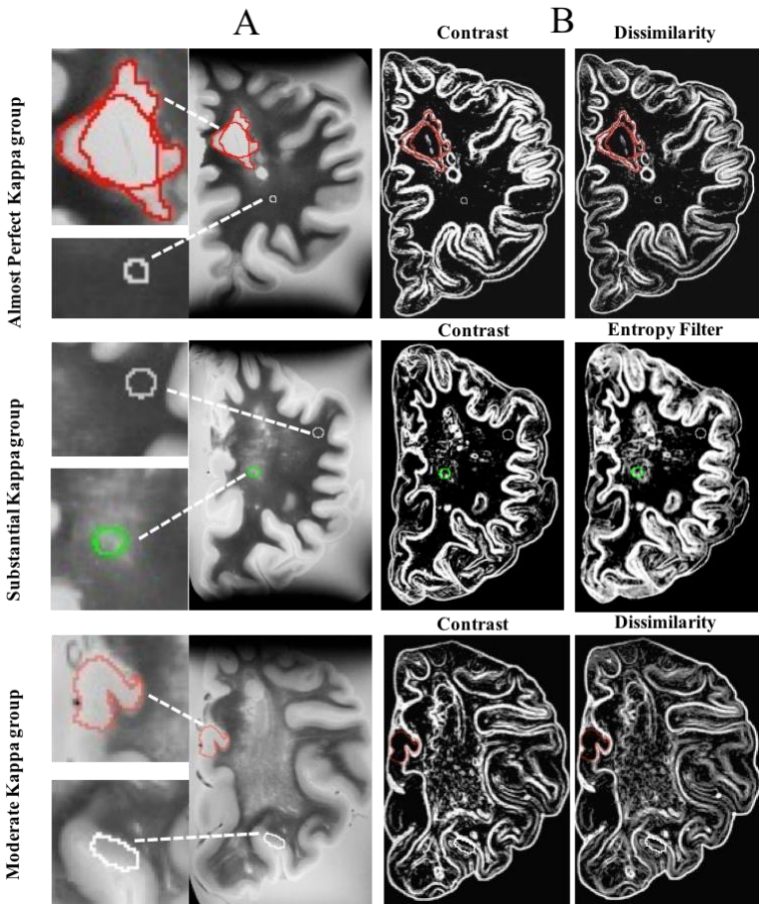

Supplementary Figure 3.1. Example T2-weighted MRI (A), and top selected feature maps (B) from tissue groups (bottom labels of the plots) with moderate, substantial or almost perfect Kappa performance (bottom to top row) in RF classifications. ROIs with the shade of white and red are normal appearing and lesions in grey and white matter, respectively. Green ROI represents diffusely abnormal white matter.

Supplementary Table 3.1. Sensitivity and specificity for unbalanced data classification tasks

Moderate to perfect Kappa groups	Sensitivity	Specificity
NAWM-DAWM	0.77	0.95
NAWM-demWM	0.93	0.98
DAWM-demWM	0.83	0.97
NAWM/DAWM/remWM/demWM	0.56	0.93
Normal WM- NAWM	0.78	0.87
NAGM-demGM	0.95	0.59
NAGM/remGM/demGM	0.51	0.81
Type I- Type II	0.96	0.43
Type I- Type III	0.77	0.8
Type I- Type IV	0.67	0.69
Type III- Type IV	0.64	0.76
Type I/II/III/IV	0.47	0.85
remWM/demWM/remGM//demGM	0.21	0.74

Supplementary Table 3.2. Sensitivity and specificity for balanced data classification tasks

Moderate to perfect Kappa groups	Sensitivity	Specificity
NAWM-DAWM	0.77	0.95
NAWM-demWM	0.96	1
DAWM-demWM	0.85	0.97
NAWM/DAWM/remWM/demWM	0.56	0.93
Normal WM- NAWM	0.79	0.87
NAGM-demGM	0.95	0.58
NAGM/remGM/demGM	0.5	0.8
Type I- Type II	0.96	0.45
Type I- Type III	0.81	0.79
Type I- Type IV	0.69	0.72
Type III- Type IV	0.66	0.77
Type I/II/III/IV	0.48	0.85
remWM/demWM/remGM//demGM	0.39	0.85

4.4.3 Selected features contributing to moderate to almost perfect classification

RFE assessment showed that texture features ranked the highest in each of the 13 classification tasks showing moderate to almost perfect performance, particularly T2 MRI texture measures (Table 3.2; Figure 3.4). Among texture features, T2- GLCM contrast (T2-contrast) and T2- GLCM dissimilarity (T2-dissimilarity) were most frequently selected. Out of the directional texture measures, the average and maximum T2 MRI texture of all 4 directions were chosen the most (Table 3.4). Further, the average features were selected slightly more than the maximum features based on the top-ranked features (T2-contrast and T2-dissimilarity), and therefore were used in subsequent analyses.

In classifying WM tissue types of MS, T2-contrast and T2-dissimilarity were the most selected RFE features, with T2-contrast chosen most frequently. FA was selected once in classifying NAWM from DAWM. Between control white matter and NAWM in MS, diffusion texture measures (ASM and entropy), T2-entropy filter, and MTR were the top selected features.

In GM tissue type classifications, T2-contrast, T2-dissimilarity, and T2-entropy filter were the most frequently selected RFE features, either across all 3 tissue types or between NAGM and demGM in MS (see Table 2). Between demGM types (I-IV), T2- GLCM correlation (T2-correlation) was the top feature in each classification scheme, followed by T2- GLCM ASM (T2-ASM), and then other T2 and diffusion texture features. Between de- and re-myelinated lesions from both grey and white matter, T2 texture features (T2-contrast and T2-dissimilarity) stayed as top classifying features, followed by MTR.

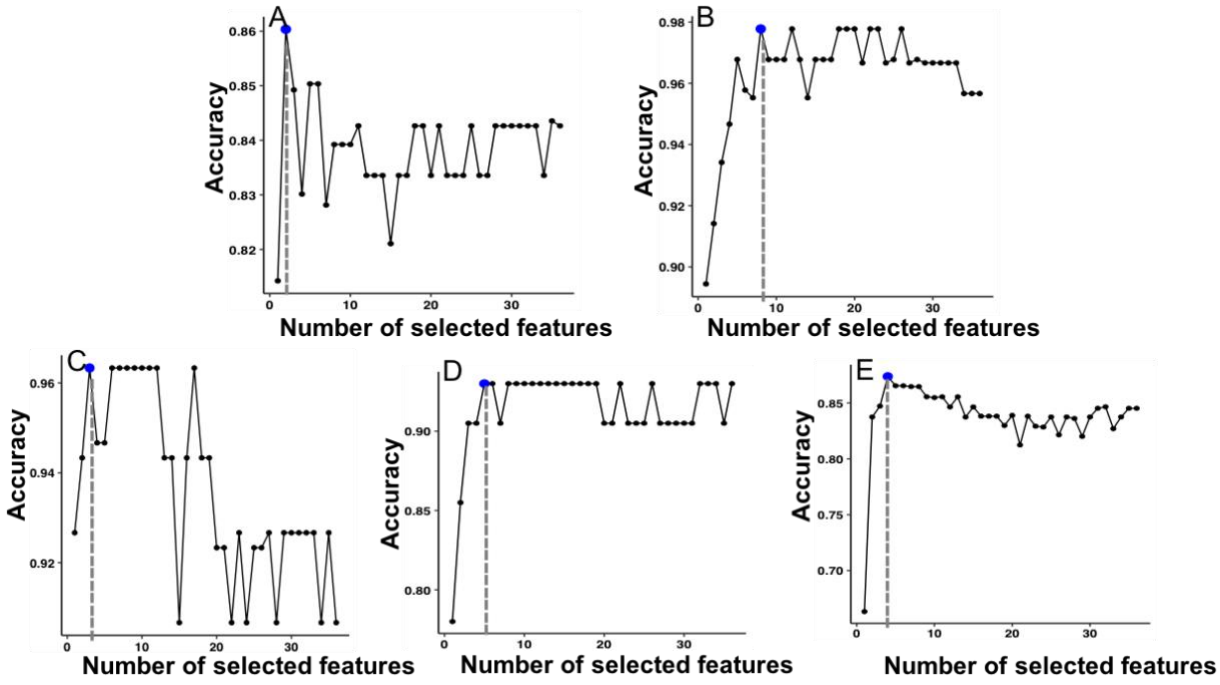

Figure 4.4. Outcomes of the recursive feature elimination method. Shown are results from 5 tissue groups with substantial to almost perfect Kappa performance in random forest classifications. The vertical dash lines indicate the locations of accuracy thresholds used to select the top-ranking variables. The plotted tissue groups are: NAWM/DAWM/remWM/demWM (A), NAWM/demWM (B), DAWM/demWM (C), NAWM/ DAWM (D), and normal white matter/NAWM (E). Note: NAWM=normal appearing white matter; DAWM=diffusely abnormal white matter; remWM and demWM=re- and de-myelinated white matter lesions.

Table 4.4. The frequency of GLCM features selected by RF-RFE.

Feature	**0**	**45**	**90**	**135**	**Average**	**Max**
T2-contrast	2	2	1	3	5	3
T2-dissimilarity	-	-	1	2	2	1
T2-entropy	-	-	-	-	-	-
T2-ASM	2	2	-	1	-	1
T2-correlation	2	1	3	1	1	3
Total	6	5	4	7	8	8

Note: Average = mean value of all 4 directions; Max = maximum value of all 4 directions.

4.4.4 Classification performance based on individual imaging modalities

Based on results in feature selection analysis, T2-contrast and T2-dissimilarity were the top 2 ranked texture features. Therefore, these 2 features were used to compare with the advanced MRI measures: MTR and FA, based on the balanced data approach. In both binary and multi-label classification tasks, both texture features performed better than MTR or FA, where the latter did not show considerable difference (Table 3.5). Further, no models based on single feature alone, texture-based or not, performed better than the corresponding models based on combined features (Table 3.2; Supplementary Tables 3.1&3.2).

Table 4.5. Binary and multi-label classification accuracy and Kappa based on individual modality features with data following balance adjustment

Tissue groups	Contrast (Accuracy/Kappa)	Dissimilarity (Accuracy/Kappa)	MTR (Accuracy/Kappa)	FA (Accuracy/Kappa)
NAWM-demWM	1.00/1.00	1.00/1.00	0.68/0.36	0.45/-0.11
NAWM/DAWM/remWM/demWM	0.75/0.59	0.78/0.63	0.53/0.24	0.28/-0.13
NAWM-DAWM	0.87/0.51	0.86/0.54	0.76/0.2	0.77/0.36
NAGM-demGM	0.82/0.39	0.83/0.41	0.72/-0.04	0.79/0.15
NAGM/remGM/demGM	0.78/0.38	0.79/0.39	0.66/0.05	0.58/-0.07
DAWM-demWM	0.8/0.35	0.85/0.42	0.7/-0.1	0.7/-0.1
remWM/demWM/remGM//demGM	0.74/0.34	0.76/0.3	0.64/0.03	0.63/-0.09
Normal WM/NAWM	0.53/0.05	0.46/-0.05	0.55/0.09	0.5/-0.01
Type III- Type IV	0.51/0.04	0.57/0.15	0.48/-0.02	0.46/-0.08
Type I- Type III	0.51/0.03	0.59/0.18	0.45/-0.09	0.44/-0.1
Type I/II/III/IV	0.31/0.01	0.39/0.11	0.24/-0.05	0.33/0.06
Type I- Type II	0.69/0	0.71/0.02	0.72/0.02	0.69/-0.03
Type I- Type IV	0.47/-0.05	0.51/0.03	0.58/0.17	0.53/0.07

4.4.5 Group comparison outcomes based on selected features

Texture features outperformed MTR and FA in classifying white matter tissue types

Considering all combinations of white matter tissue groups, there were 6 RFE features chosen: 4 from T2 MRI texture analysis (contrast, dissimilarity, ASM, entropy filter), and 2 from advanced MRI: MTR and FA (see Table 3.2). Kruskal-Wallis tests showed that T2-texture features differentiated more white matter tissue groups than MTR (2 groups) and FA (1 group). Further, T2-contrast and T2-dissimilarity were the only features that differentiated NAWM from DAWM, and DAWM from demWM significantly. Likewise, T2-ASM and T2-entropy filter significantly differentiated NAWM from all other white matter tissue types. Between normal white matter and MS NAWM, while the RFE selected 3 types of features (2 diffusion-texture, 1 T2-texture, and MTR), only diffusion ASM and diffusion entropy achieved significance in this step. Furthermore, the direction of changes in texture values was more consistent in texture measures than MTR or FA. T2-ASM was descending from the NAWM to DAWM and to remWM, then to demWM. Conversely, changes in tissue complexity-associated measures (T2-contrast, T2-dissimilarity, and T2-entropy filter) showed the opposite direction. The features were ascending from the NAWM to DAWM and to remWM, then to demWM (Figure 3.5). Additionally, using the top-ranked features: contrast and dissimilarity, texture analysis of the down-sampled T2-weighted images showed the same trend in comparing WM tissue types. The most difference remained between NAWM and demWM (Figure 3.6 & Figure 3.7).

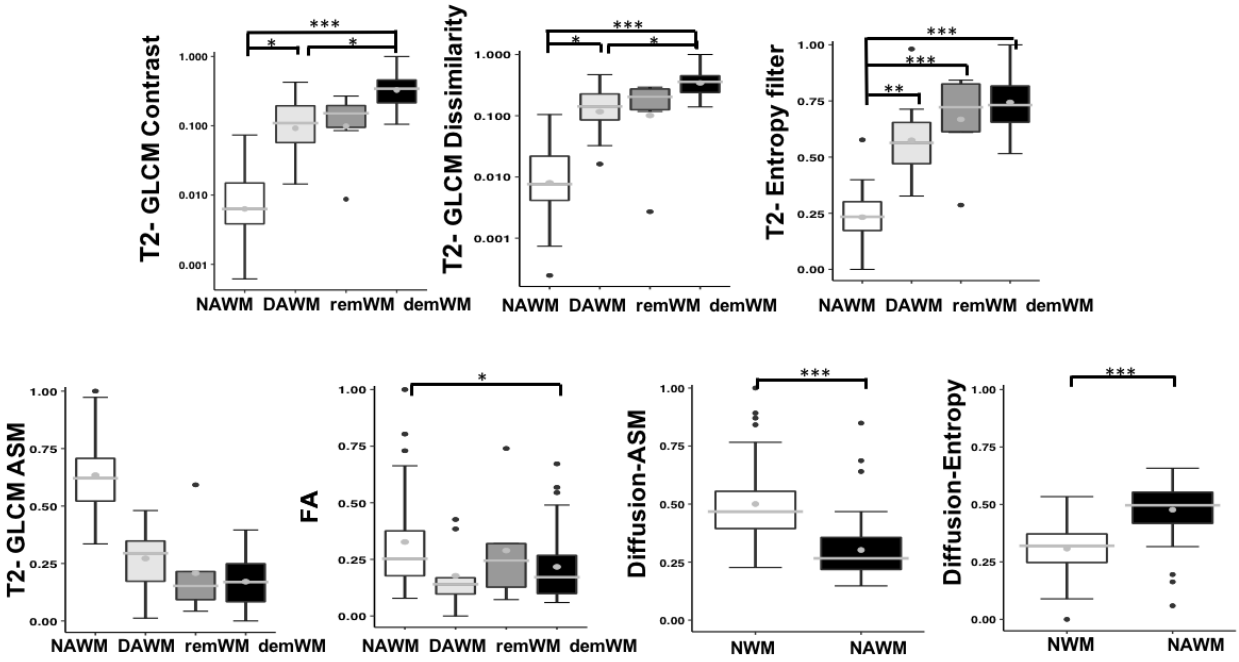

*Figure 4.5. Group comparison of tissue types in brain white matter of MS patients (first 5 plots) and controls (the last 2 plots). Shown are parameters that show significance after being selected by the recursive feature ranking algorithm. The Y-axis of T2- GLCM contrast and T2- GLCM dissimilarity is in the logarithmic scale to increase visibility of the differences. Note: ASM= angular second moment; NAWM= normal-appearing white matter; DAWM= diffusely abnormal white matter; remWM= remyelinated lesions; demWM= demyelinated lesions; NWM= normal white matter. The stars indicate significance values: *p<0.05; **p<0.01; ***p<0.001. The boxes are interquartile range (IQR), the lines are the median, and the grey dots are the mean.*

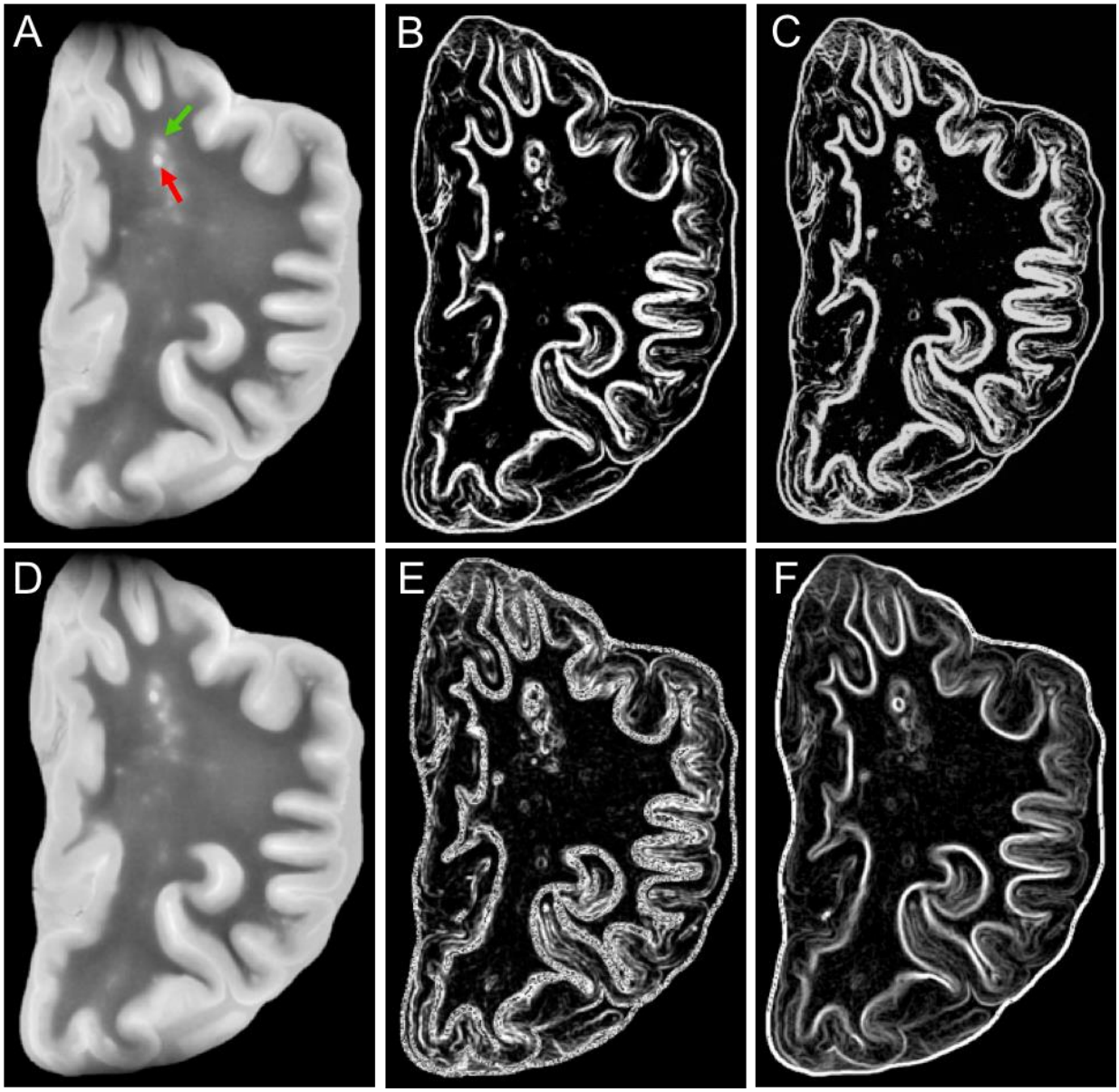

Figure 4.6. Example original (top) and down-sampled (bottom) T2-weighted MRI and the associated texture maps from postmortem brain samples used in this study. Images in A and D represent original images. The arrows in A indicate white matter lesion areas without (red arrow) and with (green arrow) remyelination. The texture maps represent T2- GLCM contrast (B) and T2- GLCM dissimilarity (C) from original and from down-sampled (E & F) T2-weighted MRI, respectively, averaged from all 4 directions of the GLCM. The texture maps derived from down-sampled MRI (pixel size=1 x 1) still show the same pattern as those computed from the original high resolution T2-weighted MRI (pixel size=0.1 x 0.1).

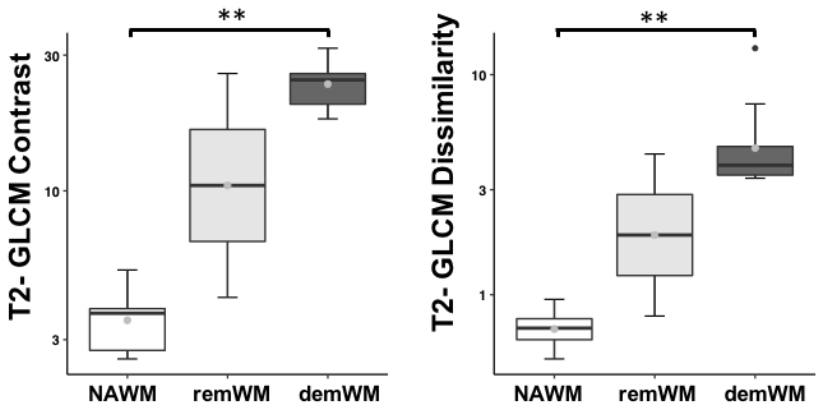

*Figure 4.7. Texture comparison between WM tissue groups of three MS subjects using down-sampled T2-weighted images. The differences in T2- GLCM contrast and T2- GLCM dissimilarity between WM tissue groups maintain the same trend as using original images (see figure 3.5). NAWM= normal-appearing white matter; remWM= remyelinated lesions; demWM= demyelinated lesions; NWM= normal white matter. The stars indicate significance values: *p<0.05; **p<0.01; ***p<0.001. The boxes are interquartile range (IQR), the lines are the median, and the grey dots are the means.*

T2 texture features alone differentiated grey matter tissue types

In classifying different combinations of grey matter tissue types, the top rankings in RFE included T2 texture features only (contrast, dissimilarity, and entropy filter). Kruskal-Wallis analysis revealed that all the 3 T2 texture features were significant in differentiating NAGM from demGM, and NAGM from remGM, where the features were significantly lower in the NAGM than demGM and remGM. Between demGM and remGM, these T2 texture features were not significantly different (p=0.20 to 0.70; Figure 3.8).

Among the 4 demGM subtypes, 3 of the 6 RFE features showed significance in pair-wise comparisons. Specifically, T2-ASM and T2-entropy filter each differentiated 3 tissue pairs after

correction for multiple comparisons, more than T2-correlation that discriminated 2 pairs. The significance of differentiation was also greater in the former than the latter, particularly T2-ASM (see Figure 3.8).

T2 texture features differentiated de- and re-myelinated lesions in the white matter

Out of the 3 RFE features (T2-contrast, T2-dissimilarity, and MTR) that classified de- and re-myelinated lesions combined from grey and white matter, only the 2 T2 MRI texture features retained significance in Kruskal-Wallis analysis, not MTR (p=0.9). In post-hoc assessments using the Dunn test, both the texture features were significant in separating demWM from remWM, yet not demGM from remGM (p=1.0 and 0.8; Figure 3.9).

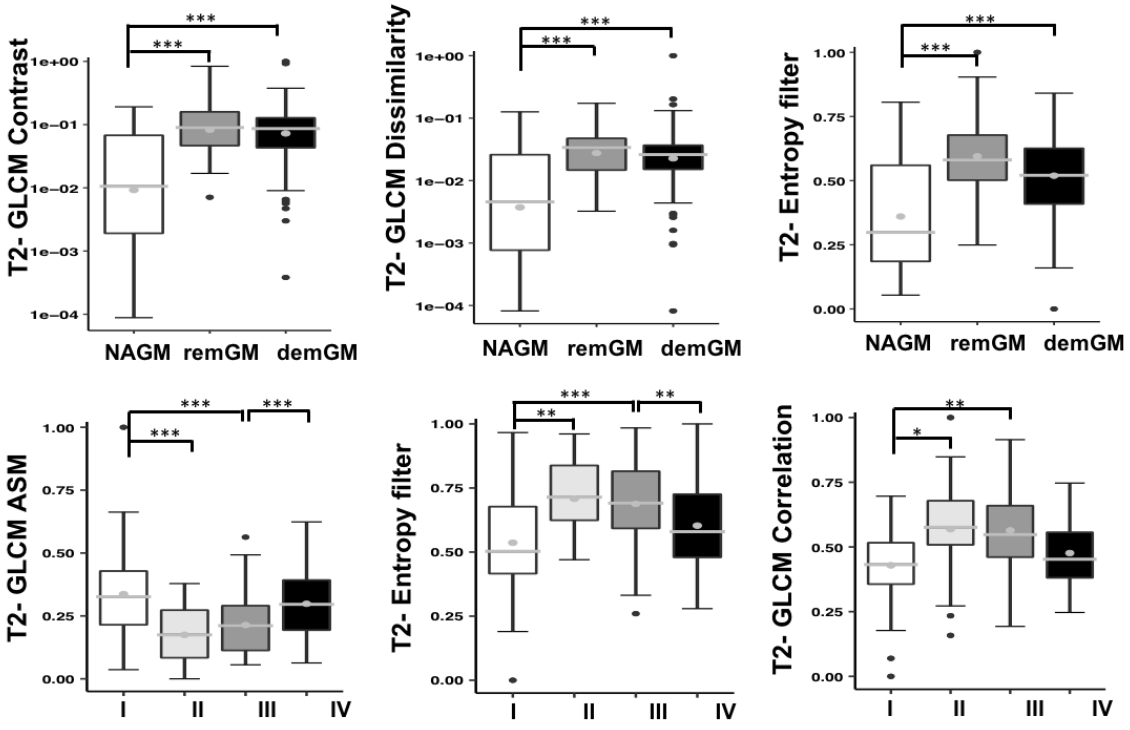

Figure 4.8. Group comparison of tissue types in brain grey matter of MS patients. Shown are parameters that show significance after being selected by the recursive feature ranking algorithm.

*The Y-axis of T2-GLCM contrast and T2-GLCM dissimlarity is in the logarithmic scale to increase visibility of the differences. Note: ASM= angular second moment; NAGM= normal-appearing grey matter; remGM= remyelinated grey matter lesions; demGM= demyelinated grey matter lesions; Type (I-IV): cortical lesion types. *p<0.05; **p<0.01; ***p<0.001. The boxes are interquartile range (IQR), the lines are the median, and the grey dots are the mean.*

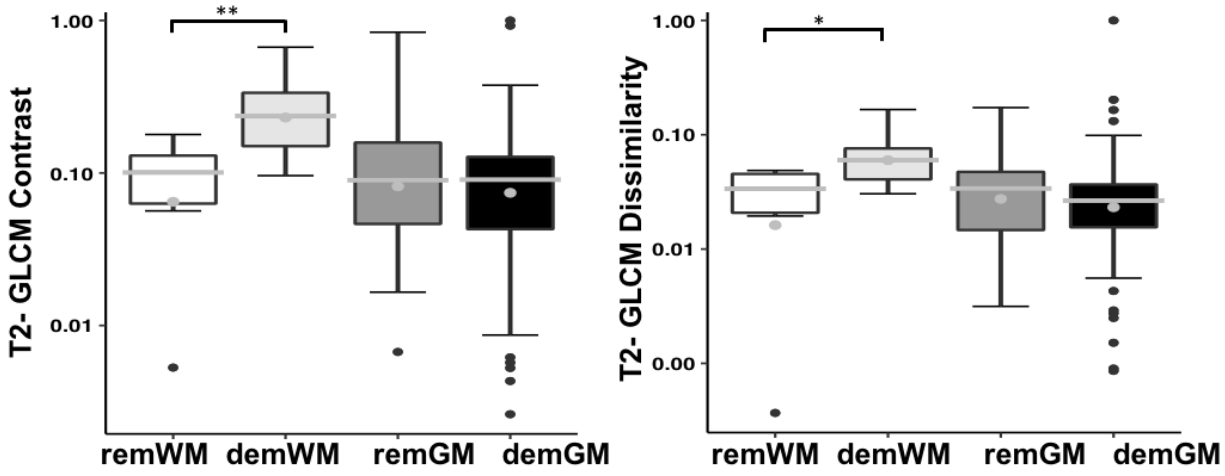

*Figure 4.9. Group comparison of remyelinated and demyelinated lesions in both grey and white matter of MS brains. Shown are parameters that show significance after being selected by the recursive feature ranking algorithm. The Y-axis is in the logarithmic scale to increase visibility of the differences. Note: remWM and demWM = remyelinated and demyelinated white matter lesion; remGM and demGM = remyelinated and demyelinated grey matter lesion. The stars indicate significance values: *p<0.05; **p<0.01. The boxes are interquartile range (IQR), the lines are the median, and the grey dots are the mean.*

4.5 Discussion

Using pathology-verified brain MRI scans, this study assessed the potential of texture analysis using T2-weighted and diffusion images for differentiating tissue types in MS as compared to 2 common advanced MRI measures. In particular, through upsampling of diffusion MRI directions,

this study provided new measures of DTI texture. Overall RF-based analyses suggested that MRI texture measures outperformed MTR and FA, and that T2 texture features were greater than diffusion texture features, with or without adjustment of data balance. Further, based on balanced data, the multi-label classification models performed equivalently in predicting unseen data to the cross-validated models, and models based on multi-modality features were superior to models using a single modality feature for both binary and multi-label classifications. In subsequent group-based assessments, T2 texture features were still significant in dividing lesions from non-lesion areas, subtypes of demGM, and demyelinated from remyelinated lesions.

The GLCM is one of the most commonly used statistical texture analysis methods. Based on second-order texture features, numerous investigations have shown the promise of GLCM to characterize tissue abnormalities including that occurs in MS [16, 108], but few with pathological confirmation. In this study, our T2-MRI analysis focused on 5 recommended second-order GLCM features, among which T2-contrast, T2-dissimilarity, and T2-entropy filter showed the most importance in distinguishing demyelinated lesions from non-lesion areas seen in both grey and white matter. GLCM features reflect changes not only in image signal intensity, but also in signal distribution patterns, which in theory reflects the structural integrity of the underlying tissue. Previous evidence has already shown close relationships between MRI signal intensity and the degree of myelination [173]. In MS, tissue damage increases from the NAWM to DAWM, and to demWM, and demyelination was found to be more severe than axonal loss in the DAWM [174]. Consistently, our top-ranked T2 texture measures in this study were worst in demWM, and worse in DAWM than NAWM, suggesting their sensitivity to the pattern of structural organizations, including myelin integrity. Further, our preliminary experiments using the down-sampled brain

MRI revealed comparable results, although not all analyses reached significance, likely due in part to the small sample size tested. It is worth noting that texture analysis is typically more sensitive to structural differences than image signal intensity alone but is not necessarily specific. The encouraging performance of our texture measures could be due to several factors, including the joint use of machine learning algorithms (the RFs), which have the ability to achieve optimal decisions using even weakly specific variables [175]. Our preliminary leave-one-out analysis showed similar results, indicating that our findings were primarily due to imaging feature differences at the tissue type level rather than variations at the patient level.

MT imaging and DTI are two of the most commonly used methods in assessing tissue pathology in neurological diseases including MS [176]. Therefore, comparing model performance with features from these two modalities is reasonable. In the current study, MTR was among the RFE-significant features in classifying de- and re-myelinated lesions from grey and white matter as well as normal white matter and NAWM, whereas FA was RFE important in classifying NAWM and demWM. But they differentiated much fewer tissue groups than T2 MRI texture features. To confirm our results, we have also taken analyses using data with balance adjustment. Data imbalance is common in medical imaging and may cause bias toward the majority class that affects model outcome [177]. Our results demonstrated that when all variables were considered, the classification models performed similarly with or without data balance adjustment, despite mild improvement for the former. These findings were further verified by the multi-label models in predicting completely unseen data, where all classifications achieved competitive performance compared to models trained through cross-validation. When comparing features from each modality alone, we observed similar findings. Based on balanced data, both T2-contrast and T2-

dissimilarity performed better than MTR or FA, although models using either T2 texture feature alone did not perform as competitive as models using combined imaging features.

Similar mechanisms may apply to the comparisons between grey matter tissue types. Essentially, the same T2 texture features identified in classifying white matter tissue types also differentiated NAGM from remGM or demGM. Between subtypes of demGM, T2-correlation showed the most consistency in RF classifications. Likewise, in subsequent group comparisons, only T2 texture measures showed significance. Compared to white matter pathology, cortical lesions possess slightly different pathological changes including demyelination, axonal transection, neuronal/glial loss, and inflammation [159]. In addition, Type I lesions hold relatively high myelin density as they occupy both grey and white matter, and type III lesions are under the pial surface that has low myelin density. Therefore, the detection of significant differences between types I and III lesions by T2-ASM, T2-entropy filter and T2-correlation may suggest their sensitivity to myelin content, although inflammation may also play a role. This is because type I lesions are the only subtype that involves white matter that is known to be more severe in the infiltration of inflammatory cells than grey matter in MS, which could make type I lesions more inflammatory than type II and type III lesions [178]. In a prior post-mortem study, type I lesions showed higher MTR, suggesting greater myelin content, than type III lesions [159]. In the present study, however, no advanced MRI measures showed significance in differentiating grey matter pathology. Further, our T2-ASM and T2-entropy filter measures also classified type III and type IV lesions. Because these 2 types of lesions seem to have similar inflammatory involvement, and type IV lesions extend to the higher myelin density area, the separation between types III and IV lesions might also highlight the

relevance of T2-ASM and T2-entropy filter with myelin content. Nonetheless, no measures differentiated types II and III or types I and IV lesions, deserving further investigation.

Differentiating de- and re-myelinated lesions has been a long-term challenge in demyelinating diseases including MS. To provide proof-of-concept evidence, we combined all available grey and white matter lesions in the analyses based on all computed imaging measures. While both T2 MRI texture features (T2-contrast, T2-dissimilarity) and MTR ranked high in RFE, only the T2 texture measures showed significance, particularly in comparing white matter de- and re-myelination. Histopathologically, MS lesions with myelin repair may have contributed to a more uniform tissue pattern than those without [179], resulting in lower T2-contrast and T2-dissimilarity. In addition, myelin debris is abundant in demyelinated lesions, which should also cause increased MRI texture inhomogeneity, as compared to debris clearance in remyelinated lesions [180]. In the grey matter, while RF models classified de- and re-myelinated lesions with competitive performance, the significance was lost in post-hoc analyses. The unique entities of tissue structure and pathology in the grey matter might have played a role. For instance, there is a greater density of oligodendrocytes, higher number of myelin internodes, and lower degree of inflammation and therefore less clearance of myelin debris in the grey matter [181], which could lead to more complex patterns of lesion texture than the white matter. Moreover, the myelin content is considerably lower in the grey matter, making precise detection of feature pattern differences more challenging using MRI than white matter. In the literature, several studies support the utility of texture analysis for studying de- and re-myelination. Using an animal model of MS [153], the authors not only detected texture changes in demyelination induced by a toxic diet in different brain regions, but also occurrence of remyelination, based on a statistical texture feature selected

by a stepwise machine learning approach. In a post-mortem study of MS patients [173], texture spectral magnitude over low-frequency scales was greater in demyelinated than remyelinated lesions in brain white matter, indicating the relevance of texture heterogeneity with myelin content. However, these experiments were mainly descriptive. Our findings in the present study suggest that combined application of texture analysis and machine learning algorithms is likely a useful means for distinguishing de- and re-myelinated lesions. But caution should be taken in interpreting these data as our results were mainly significant with an increased sample size when considering both grey and white matter lesions.

Considering patient versus control assessment, the RFE detected 4 measures, including MTR, but only 2 diffusion texture features (ASM and entropy) survived subsequent analyses in group comparisons. Both these features showed significance in differentiating NWM from NAWM. In this study, we used a novel approach to compute high-resolution diffusion texture, which used orientation-interpolated DTI data per pixel, as opposed to in-plane texture calculations within a parametric map as typically done. Prior studies using a similarly new technique showed a greater ability than FA in characterizing white matter integrity following traumatic brain injury [18]. Tissue injury in NAWM is less than MS lesions and DAWM but is evident, including inflammation, gliosis, demyelination, and axonal damage [174]. These changes would increase diffusion magnitude and orientation, and therefore decrease diffusion ASM and increase diffusion entropy. In a recent diffusion MRI study [182], advanced analysis of diffusion signals using a composite hindered and restricted model of diffusion (CHARMED) has also shown a greater ability in differentiating normal white matter from MS NAWM than traditional DTI measures,

including FA. Further, our overall findings also suggest that the new diffusion texture measures are mainly sensitive to NAWM pathology. Their utility in assessing NAGM remains unclear.

This study has a few limitations. First, the number of ROIs is different between tissue types and subjects. Yet the overall sample size is reasonable compared to the literature, and our overall analyses suggest that the classification results are mainly due to tissue pathology differences rather than patient-level variances. Second, the signal intensity of ex vivo MRI used here may be different from in vivo MRI. However, texture patterns are shown to be robust to signal intensity changes [141], and therefore our focus on texture pattern analysis should have helped mitigate this potential limitation. Third, the resolution of our T2-weighted MRI in this study is higher than their counterpart acquired typically in vivo, raising a suspicion about applications in a clinical setting. While deserving further evaluation, various studies using GLCM or alternative texture analysis methods have shown the promise to characterize tissue pathology using common clinical scans in MS and similar diseases [108, 141]. Further, our pilot experiment suggests the similarity between texture outcomes derived from super high-resolution brain MRI versus low-resolution and clinically equivalent images. Fourth, the ability of our texture analysis methods for differentiating partial demyelination from remyelination was unknown, because those tissue types were not characterized histologically for confirmation. The texture heterogeneity of partial demyelination could be higher than remyelination due to clearance of myelin debris in the latter process but that deserved confirmation. Fifth, texture improvement in MS lesions could be also due to other pathological changes such as resolution of inflammation or edema but those were not assessed histologically. Nonetheless, the contribution of recovering inflammation was found to be much less than myelin integrity in prior postmortem studies, and the extent of inflammation was expected

to be minimal in progressive MS as studied here compared to other subtypes of MS. In the future, we plan to validate our findings using data with different types of pathologies characterized, assess texture outcomes from in vivo imaging especially that with clinical MRI-equivalent resolution, and compare outcomes with other quantitative approaches originated from either conventional or advanced MRI.

In conclusion, this study demonstrates the utility of robust MRI texture analysis and machine learning methods in differentiating critical grey and white matter pathology types in the brain of MS patients. In particular, several texture features from T2-weighted MRI have shown the potential to distinguish demWM and remWM, and among demGM subtypes. Both are long standing challenges in MS research in the context of imaging, and therefore findings of this study may stimulate new advancement in the evaluation of both disease activity and treatment responses. In addition, given the wide availability of conventional MRI in clinical practice, our method can be replicated in MS or similar diseases.

Chapter 4: Characterizing severely demyelinated and highly remyelinated brain magnetic resonance imaging lesions in multiple sclerosis participants using histology-verified texture analysis measures

5.1 Background

In vivo characterization of lesion severity using MRI is invaluable for improved characterization of disease activity and discovering new therapies. However, robust in vivo metrics are missing. As confirmed in Chapter 3, texture analysis of conventional MRI showed the most promise in distinguishing brain MS pathology types, including lesions with de- or re-myelination, where GLCM-contrast and GLCM-dissimilarity performed the best. Based on these MRI texture features, the objective of this chapter was to develop a new method for identifying brain MS lesions that had the most de- or re-myelination in vivo. Specifically, this study used a commonly applied percentile approach, with recognized thresholds such as the 25^{th} and 75^{th} percentiles of texture values to define brain MRI lesion types, namely, highly remyelinated and severely demyelinated, respectively. Imaging measures of these 2 identified lesion types were further assessed for their relationship with clinical outcomes of the same MS participants. Part of the results in this chapter has been published at an international conference as an abstract [21].

5.2 Introduction

MS is a common inflammatory and disabling disease of the central nervous system characterized by several pathological changes including demyelination and remyelination [149]. Focal lesions are critical indicators of disease activity in MS, and the prevalence of damaging and reparative lesions is associated with the degree of disability in MS participants [183, 184], particularly those with relapsing-remitting MS (RRMS). However, lesion pathology is heterogeneous, even within a subject [185, 186], posing significant challenges for in vivo assessment. A practical method for improved understanding of lesion type remains a critical need in MS research and care.

Magnetic resonance imaging (MRI) is a promising in vivo method for assessing neuropathology and has shown the potential for identifying lesion severity in MS along with data aggregation methods [133, 187, 188]. Currently much effort has been driven by advanced MRI. Based on macro- and micro-scale measures of tissue damage using diffusion MRI from 59 MS participants (53 RRMS), one study differentiated brain MS lesions into two types using a k-means clustering algorithm, and showed that lesions with greater diffusion changes correlated with worse clinical outcomes [133]. Likewise, using MR Spectroscopy and diffusion imaging, another study evaluated a subgroup of 59 RRMS participants and divided brain MS lesions into mild and severe types based on the median of radial diffusivity (RD), where only the mild lesions showed metabolite changes in favor of repair [188]. However, advanced MRI techniques have yet to be fully applicable to clinical practice and they do not always outperform methods based on conventional MRI. For instance, in assessing the change of a lesion as an indicator of neuroprotection and repair, a study investigated magnetization transfer ratio and mean diffusivity, as well as conventional MRI indices such as signal intensity and T1/T2 ratio assisted by a percentile categorization approach.

Through mixed-effects modeling, they discovered that the 25th percentile (25%^{ile}) of normalized proton density-weighted signal intensity had the greatest sensitivity in sample size estimation among all conventional and advanced MRI measures [137].

Conventional MRI is widely available. While pathologically non-specific in MS [189], conventional MRI contains rich textural information, making it a potential candidate for improved measurement of lesion severity. Visually, the texture of T1 hypointense lesions reflects the persistence of tissue damage in MS [190]. Quantitatively, texture analysis using conventional MRI detects subtle structural abnormalities invisible to the human eye [20]. Examples include characterizing white matter remodeling in the brain following traumatic brain injury [18], and separating transient and persistent T1 hypointense lesions at onset in MS [17]. In addition, based on texture analysis using a localized gray level co-occurrence matrix (GLCM) method and statistical machine learning using T2-weighted MRI of postmortem brain samples, a prior study verified that texture metrics performed the best in classifying brain MS pathologies as compared to advanced MRI measures such as fractional anisotropy (FA) and magnetization transfer ratio (MTR) [146]. Nonetheless, a criterion for identifying lesion injury and repair in MS is still lacking in clinical imaging and the relationship between such lesion metrics with clinical variables is unclear.

The goal of this study was to determine the de- and re-myelination type of MS brain lesions in living participants using histology-verified MRI texture measures. The specific aims were to: 1) conduct whole brain texture analysis in RRMS using an optimized GLCM technique; 2) classify

the de- and re-myelination type of each MS lesion using a percentile ranking approach; and 3) evaluate differences between lesion types and their relationships with age and sex.

5.3 Materials and methods

5.3.1 Participants

This study used archived data from a clinical trial of domperidone as a candidate repair therapy in RRMS (clinicaltrials.gov; identifier: NCT024993049). The trial screened 237 participants initially but the current study used a convenient sample of 200 participants. Seventeen of the 200 people had at least one gadolinium-enhancing lesion on brain MRI, who became the trial participants and who also received domperidone as an add-on treatment to their routine disease modifying therapies. However, all screened participants continued regular clinical care without add-on treatment. The clinical trial results will be reported in a separate paper and therefore are outside the scope of the current report. This study was approved by the University of Calgary Conjoint Health Research Ethics Board, and all participants provided written informed consent.

5.3.2 Imaging protocol

All MR images were acquired at a 3T scanner (Discovery750, GE Healthcare, Milwaukee, USA). The MRI protocol included clinical MRI such as T1-weighted and FLAIR images. Acquisition of T1-weighted MRI used a gradient recalled sequence, with the following parameters: repetition time (TR)/echo time (TE) = 8.1/3.1ms, field of view (FOV) = 250×250mm^2, matrix = 256×256, and slice thickness = 1mm. FLAIR MRI acquisition used a spin echo sequence, with TR/TE = 7000/128ms, FOV = 240×240mm^2, matrix = 512×512, and slice thickness = 1mm. The imaging

protocol also included other anatomical sequences and advanced MRI but are out of the scope of the current study.

5.3.3 Image preparation

The MRI scans underwent several pre-processing steps to improve quality and uniformity. The process started with brain extraction, followed by linear co-registration from FLAIR to T1-weighted MRI, using the FSL software (Oxford, UK). The next step was noise reduction done using the ImageJ software (version 1.50i, NIH, USA), which involved median and mean filtering to remove salt and pepper and Gaussian noise, respectively, as commonly seen in MRI scans [92]. The last step was image intensity normalization to the range 0-255, using the Min-Max normalization method.

5.3.4 Lesion segmentation

Focal lesions were identified using an automatic toolbox known as lesion segmentation tool (LST, v3.0.0) built in an image analysis software, SPM12 [191]. Lesion regions of interest (ROIs) were detected based on the co-registered FLAIR and T1-weighted MRI scans. After the automatic procedure, all lesion ROIs were reviewed by a neuroradiologist and manually corrected where applicable. In particular, lesions with pixels overlapping with the cerebral ventricles were adjusted to minimize partial volume effect or other undesired artifacts [192]. For similar reasons, lesions with area smaller than 5 pixels (~5 mm^2) were excluded (Figure 4.1 and 4.2).

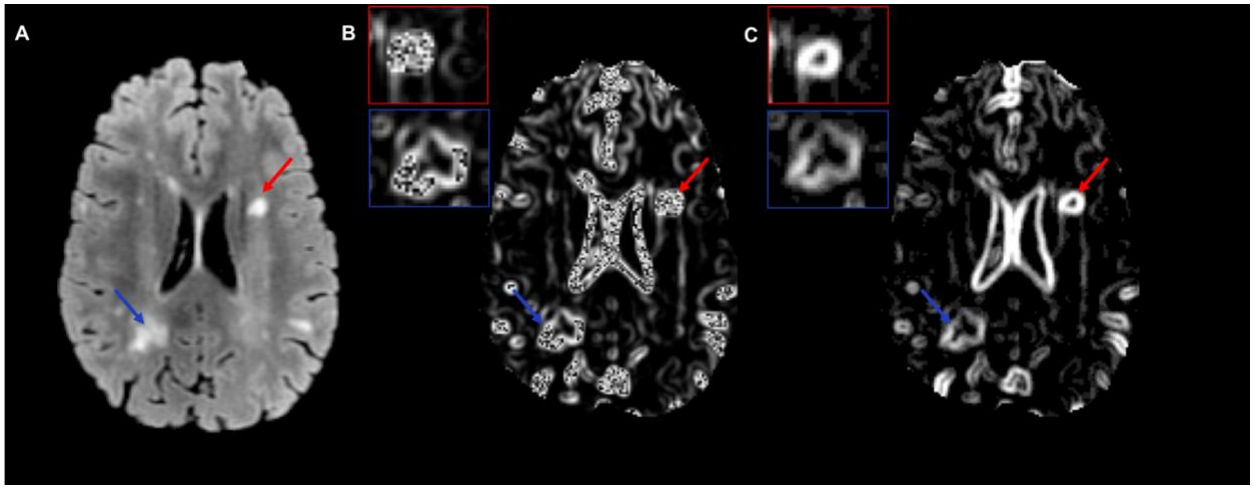

Figure 5.1. Example lesion types defined in this study from a RRMS participant. The images represent an example FLAIR MRI (A) and the corresponding texture maps on GLCM-contrast (B) and GLCM-dissimilarity (C). Red and blue arrows (and boxes) indicate severely demyelinated and highly remyelinated lesions, respectively. In the GLCM images, the brighter areas indicate coarser texture and darker regions reflect finer texture.

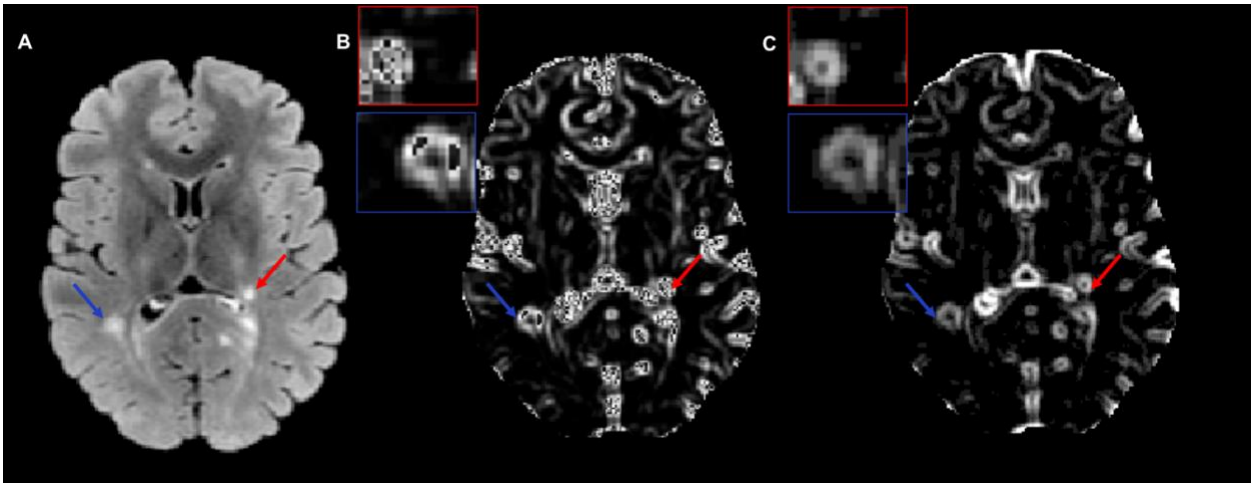

Figure 5.2. Example lesion types defined in this study from another RRMS participant. The images represent an example FLAIR MRI (A) and the corresponding texture maps on GLCM-contrast (B) and GLCM-dissimilarity (C). Red and blue arrows (and boxes) indicate severely demyelinated and highly remyelinated lesions, respectively. In the GLCM images, the brighter areas indicate coarser texture and darker regions reflect finer texture.

5.3.5 Image texture analysis

Texture analysis employed the prepared FLAIR images where lesions were most distinguishable, where calculation applied the GLCM method based on an optimized sliding-window approach. This study focused on 2 GLCM measures: contrast and dissimilarity, which showed the best performance in classifying de- and re-myelinated lesions in brain white matter using histology-informed T2-weighted MRI [146]. In addition, to ensure that the texture measures were equivalent based on T2-weighted versus FLAIR MRI, a comparison experiment was done. Using the same texture analysis procedures, texture maps were computed using both imaging sequences from five participants and quantitatively compared using 2 well-recognized metrics: structural similarity index measure (SSIM) and peak signal-to-noise ratio (PSNR). The SSIM values were between 0 and 1, the higher the greater similarity. The PSNR values were supposed to be between 30-50 for 8-bit data, and higher was better [193]. The GLCM evaluates the occurrence frequency of image pixels located in a certain distance and orientation relative to the neighboring pixels [106]. Prior research showed that a distance of 1 (one) pixel was ideal for detecting fine image texture [194], and the average texture from all 4 common directions (0°, 45°, 90°, or 135°) of GLCM demonstrated the most promise in classifying lesion types [146, 195]. Texture GLCM-contrast was a measure of local variation in grey-level intensity, highlighting tissue coarseness, while dissimilarity computed the difference between grey-level pairs, indicating tissue heterogeneity. These measures were calculated from each sliding window sized 3 by 3; iterating through the whole image provided the corresponding texture maps (see Figure 4.1). The GLCM analysis used the scikit-image library implementation in Python (version 2.7).

5.3.6 Lesion type Definition

Classifying lesion types used a percentile thresholding approach. This was based on prior evidence suggesting that the coarseness of MRI texture was significantly greater in MS lesions with tissue damage than those with repair [17, 141]. Texture contrast and dissimilarity were 2 typical measures of tissue coarseness and their decreases suggested tissue repair as verified in this thesis (Chapter 3). Further, to maximize understanding, this study considered two lesion types expected to have the highest texture differences: severely demyelinated (sDEM), and highly remyelinated (hREM). Lesion texture maps from GLCM-contrast and GLCM-dissimilarity across all 200 participants were computed, at all 4 directions as mentioned above, with the distance between pixels set at 1 (one) in each direction. The average map of the four directions per feature was calculated, and the mean texture value per lesion was used for percentile analysis in categorizing lesion types. Lesions with mean texture values ranked $\geq 75\%^{ile}$ were considered sDEM, and $\leq 25\%^{ile}$ as hREM.

5.3.7 Lesion Type Analysis

Lesion size-based analysis

The average size of individual lesions per type was measured in each participant and then averaged across all participants. Additionally, the combined volume of each lesion type per subject was computed, which was normalized by the grand total lesion volume of the corresponding subject. The normalization was done because lesion volume differs largely between patients. Without normalization by an internal reference, the comparison between lesion volumes might not reflect the actual differences between cohorts. This total normalized volume of sDEM and hREM was used in statistical analyses.

Lesion texture-based analysis

The mean texture value of each lesion type per subject was evaluated. In addition, principal component analysis (PCA) was performed to further explore the roles and relationships of the texture measures computed. This step included PCA variable correlation analysis, which indicated how the variables, such as GLCM-contrast and GLCM-dissimilarity, were related in lesion classification: positively or negatively correlated, or uncorrelated. Positively correlated variables would be grouped together, negatively correlated variables would be shown in opposing quadrants, and completely uncorrelated variables would be seen orthogonal to each other. Further, the contribution of each variable to the first and second PCs were calculated to evaluate how each measure reflected the degree of the underlying pathology.

Lesion distribution mapping

To characterize the distribution of the identified lesion types in the brain, we generated lesion probability maps. Specifically, following brain extraction, the T1-weighted MRI of each subject was firstly linear (affine)- and nonlinear- registered to a common space, which was the MNI152 1-mm T1-weighted MRI template [196]. The resulting transformations from these co-registration steps were then applied with nearest neighbor interpolation to the respective T1-aligned lesion masks. In this way, the lesion masks from each subject were aligned with the common MNI space. Averaging the masks across subjects for each lesion type generated the corresponding lesion probability maps by location of each brain voxel. Finally, a threshold of 0.1 was applied such that lesions with a probability ≥10% was kept at a location to improve reliability.

5.3.8 Relationship between lesion type and clinical variables

To explore the clinical relevance of the identified lesion types, we compared the average size and total normalized volume of each lesion type between woman and man participants, and between participants who were younger and older at screening. The age groups were divided using a similar percentile approach. Participant age was ranked, and participants with an age $\leq 25\%^{ile}$ were classified into the younger group and $\geq 75\%^{ile}$ into the older group. Further, the relationship between the average lesion size and total normalized lesion volume of each type and other clinical measures including disease duration and expanded disability status scale (EDSS) score at screening were assessed.

5.3.9 Statistical analysis

All statistical analyses used R (version 3.6.3) [172]. Data normality assessments employed the Shapiro-Wilk test. Outcome comparisons between two groups used the Wilcoxon signed-rank test, including comparisons between lesion types and between clinical variables. Pearson correlation was used for the correlation analysis. A $p<0.05$ was considered significant.

5.4 Results

5.4.1 Sample characteristics

A total of 5140 lesions was evaluated from the 200 RRMS participants, ranging 1-190 lesions per subject. The lesion size ranged from 5-342 mm^2. Participant age ranged 20.4 to 60.3 years; it was 20.4-60.3 years for women and 21-60 years for men. Across the whole group, the disability score as measured by the EDSS ranged 0-6.5, and disease duration ranged 1.4-35.6 years (Table 4.1).

The participants were under treatment with different types of disease modifying therapies, such as glatiramer acetate, interferon-beta, fingolimod, dimethyl fumarate or teriflunomideide.

Table 5.1. Demographic Table RRMS participants

Variable	Mean	SD
Age (years)	44.4	8.8
Sex (female/male)	148/52	-
Lesion volume (mm^3)	2290	3216
Lesion number (all types)	25.5	24.6
EDSS	2.25	1.51
Disease duration	11.75	7.28

5.4.2 lesion type outcomes

Based on the percentile-thresholding approach, 193 of 200 RRMS participants (96.5%) had both sDEM and hREM lesions detected; 143 were women. Four of the 200 participants had only sDEM lesions (all women), and three had only hREM lesions (one woman). Overall, there were 1285 sDEM (25%), and 1282 hREM (24.94%) in the whole cohort. Groupwise, there were 1003 (78%) sDEM and 893 (69.65%) hREM in women, and 282 (21.94%) sDEM and 389 (30.34%) hREM in men.

The sDEM had a smaller average size but larger total normalized volume than hREM

The average lesion size at a participant basis varied for each lesion type. It was between 5.72-25.11 mm^2 for sDEM lesions and 5.4-119.8 mm^2 for hREM lesions across the corresponding cohorts. Wilcoxon signed-rank test revealed that the sDEM possessed a significantly smaller average size

than the hREM (350.42 mm^2 vs 660.17 mm^2, $p < 0.001$). Conversely, the total normalized lesion volume was significantly larger in sDEM than hREM (78.24% vs. 71.34%, $p< 0.001$) (Figure 4.3).

The sDEM had higher texture values than hREM

Based on the averaged FLAIR texture value per lesion type per participant, the mean GLCM-contrast was significantly greater in sDEM than hREM (38.59 versus 21.66; $p< 0.001$). Similarly, the mean GLCM-dissimilarity was also greater in sDEM than hREM (9.86 versus 3.82; $p< 0.001$) (Figure 4.4). PCA analysis of the texture from individual lesions showed that the sDEM lesions were clearly separable from the hREM lesions based on either GLCM-contrast or GLCM-dissimilarity (Figure 4.5). The first PC explained 64.2% of the variance, whereas the second PC carried 35.8% of the variation. Further, the two texture variables appeared almost orthogonal and therefore showed a weak or no correlation with each other. Moreover, the contribution of the 2 texture variables to the PCs was approximately 50% each (see Figure 4.5). Further, our preliminary experiments demonstrated that the texture maps between T2-weighted and FLAIR MRI were similar. Quantitatively, the mean SSIM was 0.89 and PSNR was 38.89 between T2 GLCM-contrast and FLAIR GLCM-contrast, and SSIM was 0.93 and PSNR was 43.09 between T2 GLCM-dissimilarity and FLAIR GLCM-dissimilarity (Figure 4.6).

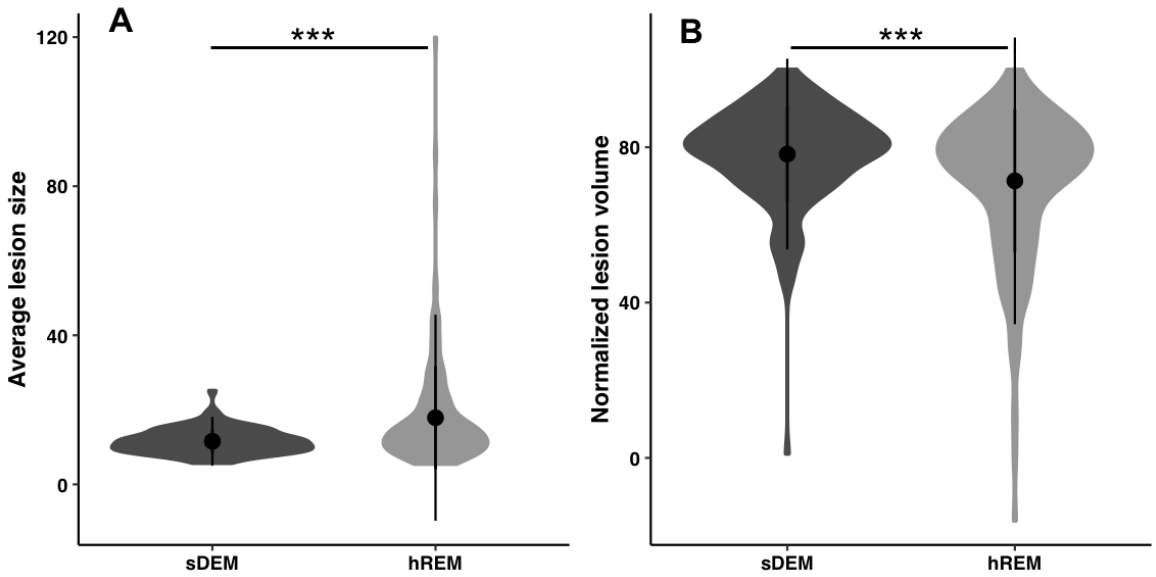

*Figure 5.3. Average size and normalized volume of the two identified lesion types patient-wise. Shown are violin plots of the mean, standard deviation, and range (density) of the measurements. sDEM= severely demyelinated, hREM=highly remyelinated lesions. *p<0.05; **p<0.01; ***p<0.001.*

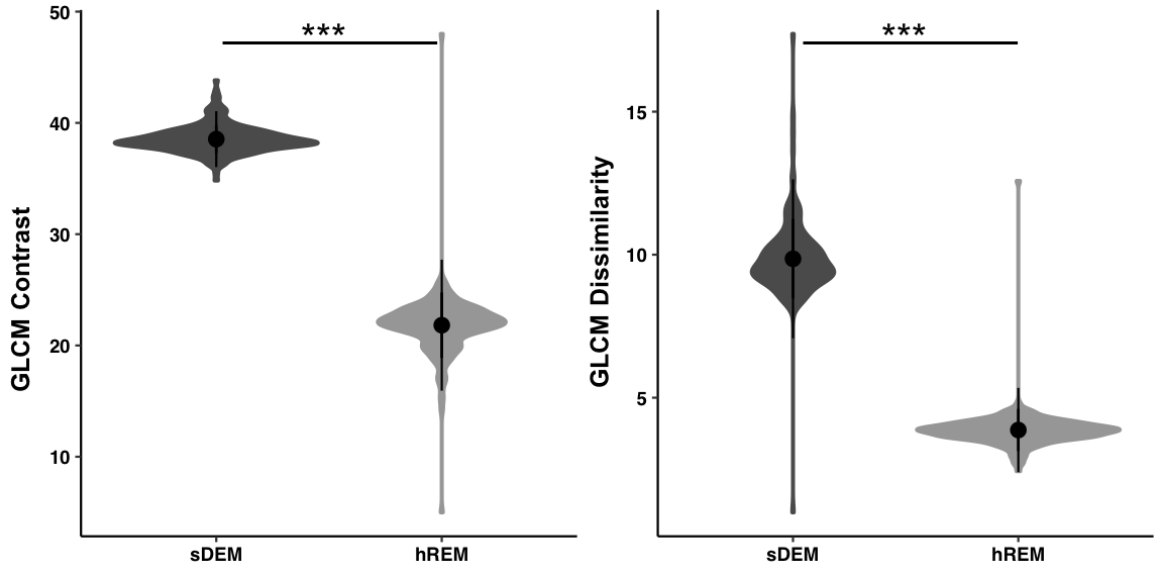

*Figure 5.4. Mean texture values of each lesion type by patient. Shown are violin plots of the mean, standard deviation, and range (density) of the measurements. sDEM= severely demyelinated, hREM=highly remyelinated lesions. *p<0.05; **p<0.01; ***p<0.001.*

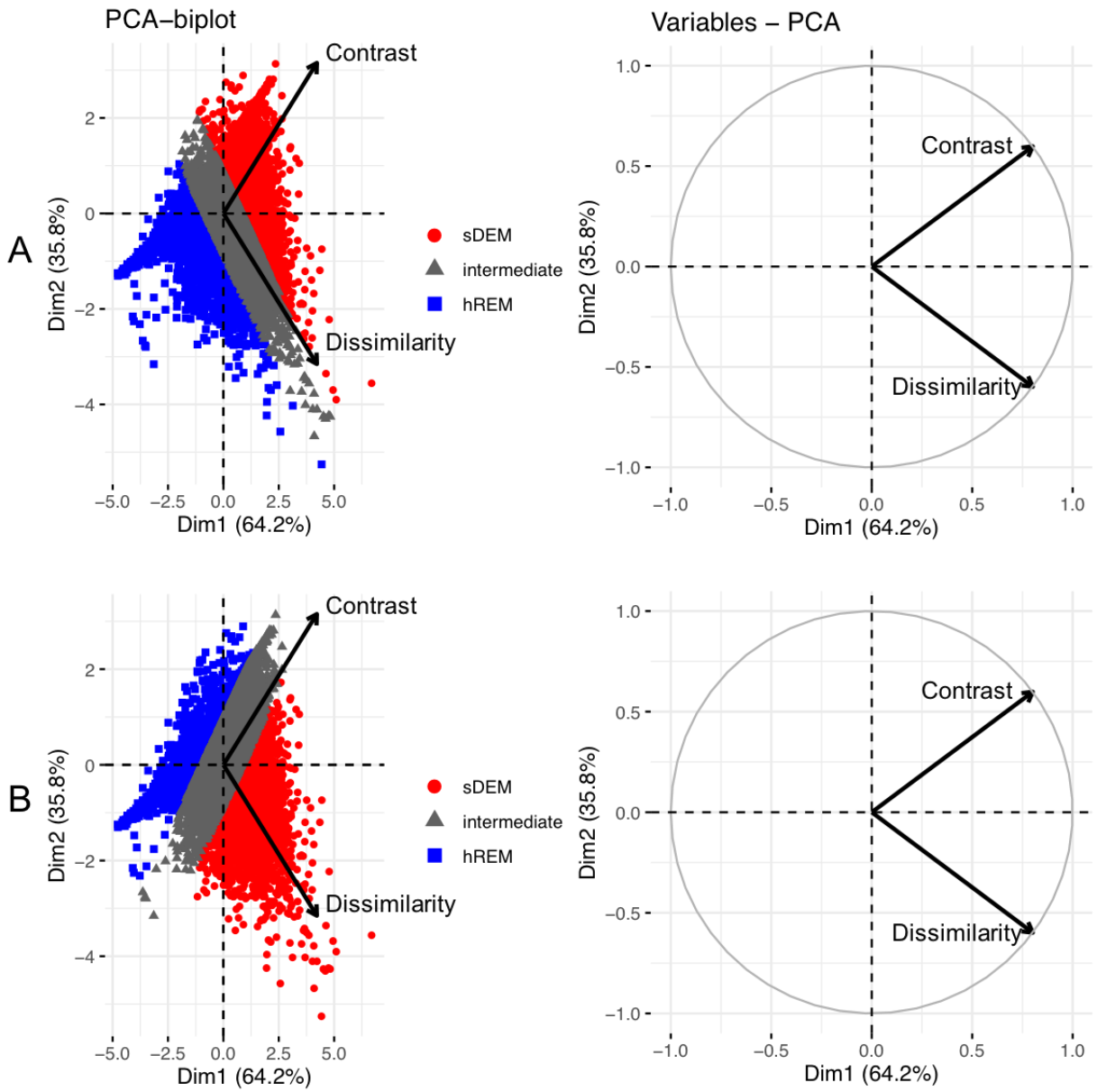

Figure 5.5. Principal component analysis biplot and variable plot. PCA biplot (left) shows the clusters of the data based on their similarity and how strongly each feature influences a principal component. PCA variable plot (right) shows the correlation and contribution of the features. The plots highlight percentile selected lesions based on GLCM-contrast (A) and GLCM-dissimilarity (B). Note: sDEM= severely demyelinated, hREM=highly remyelinated, intermediate: other intermediate lesions.

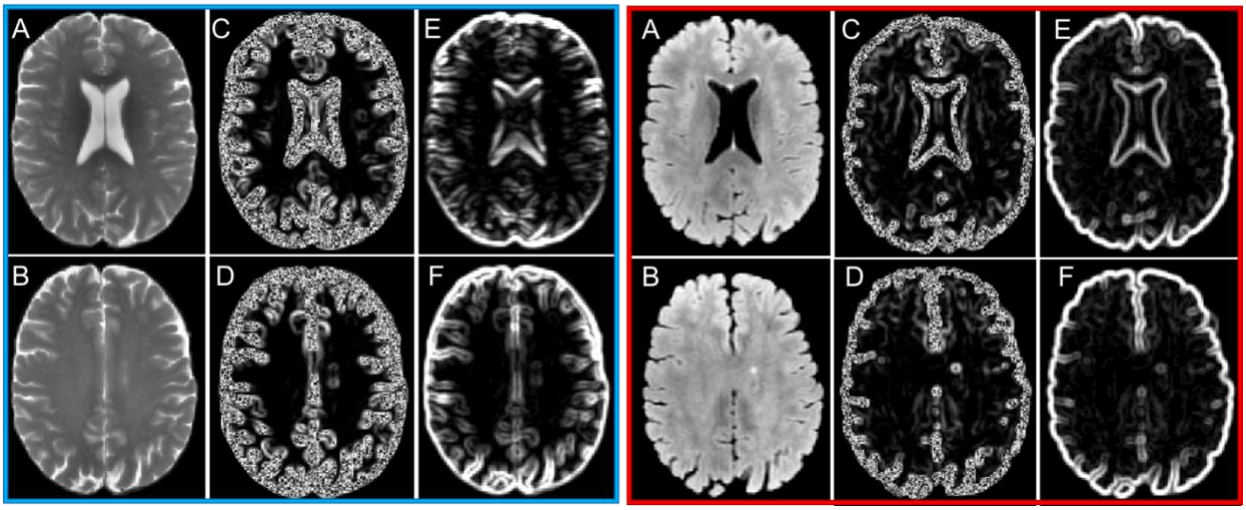

Figure 5.6. Example RRMS patient's T2-weighted (blue box) and FLAIR (red box) images and the associated texture maps of two different slices. The blue box Shown are: a T2-weighted MR image from axial brain MRI (A,B), and the related T2 GLCM-contrast (C,D), and T2 GLCM-dissimilarity (E,F), averaged from all 4 directions of the GLCM calculation. The red box Shown are: a FLAIR MRI (A,B), and the related FLAIR GLCM-contrast (C,D), and FLAIR GLCM-dissimilarity (E,F), averaged from all 4 directions of the GLCM calculation. Note: RRMS: relapsing remitting multiple sclerosis.

Probability distribution of the identified lesion types

The implementation pipeline for lesion distribution maps is shown in Figure 4.7. Both lesion types showed high probabilities in distribution at the periventricular and deep white matter regions of the brain, along with substantial overlap in location (Figure 4.8). At type-specific lesion probability maps, the hREM lesions showed a much more concentrated distribution than the sDEM lesions. Specifically, the hREM lesions were seen mainly around the lateral ventricles, corpus callosum, and subcortical regions. On average, up to 1% of the lesions from either type was distributed in the cerebellum and brainstem areas (Figure 4.8).

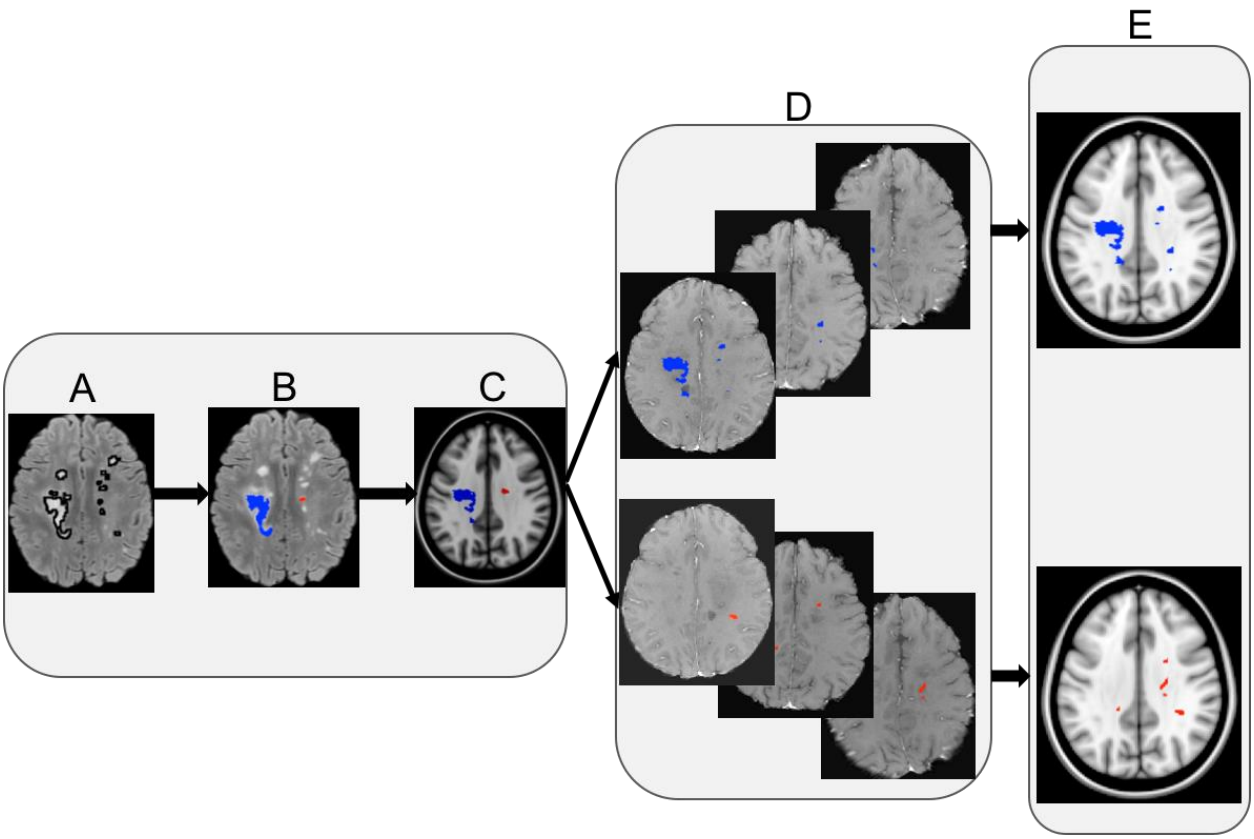

Figure 5.7. The implementation pipeline for lesion distribution maps. The left panel shows example FLAIR lesions segmented initially (A), the two identified lesion types (B), and Affine and non-linear registrated lesion masks to the MNI152 1mm T1-weighted template (overlaid on MNI template) (C). The middle panel (D) shows example lesion masks per subject/type registered to MNI template, and the right panel (E) shows the final maps averaged across subjects and thresholded.

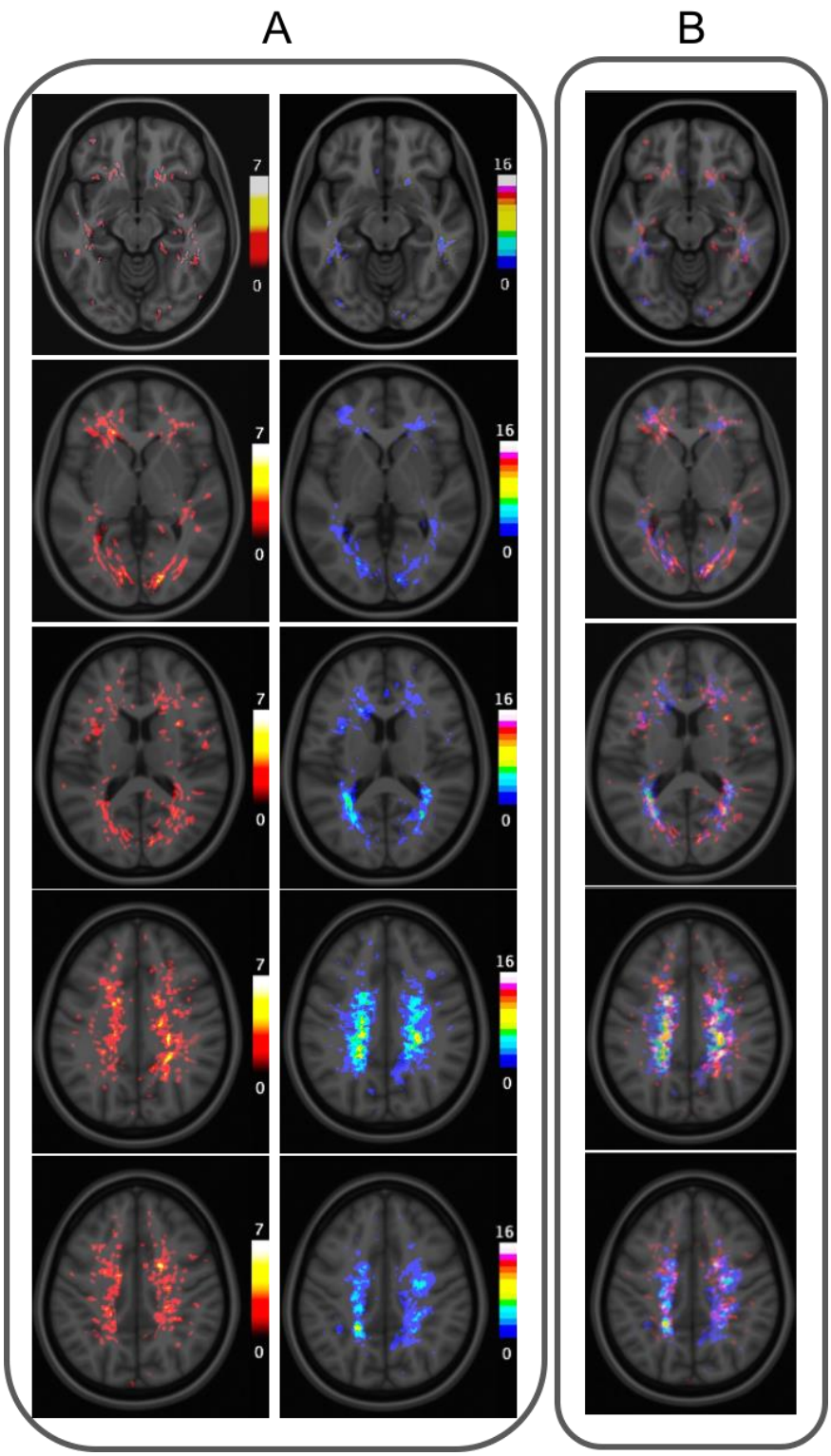

Figure 5.8. Example lesion distribution maps from the whole cohort. Severely demyelinated (red) and highly remyelinated (blue) are overlaid on MNI template (A), both lesion types are shown together on MNI template (B).

5.4.3 Lesion type outcomes in relation to clinical measures

Man participants had a significantly higher total normalized volume of sDEM lesions (p=0.01) than woman participants. Conversely, woman participants had a higher total normalized volume of hREM lesions than man participants (p=0.02; Figure 4.9). There was a trend for larger average lesion size in hREM in men than women. In sDEM, the average lesion size was not significantly different between women and men (p=0.13). There were no significant differences between youngest and oldest participants in either average lesion size or total normalized volume of the two identified lesion types. In addition, there was no correlation between average lesion size and total normalized lesion volume of either lesion type and clinical measurements.

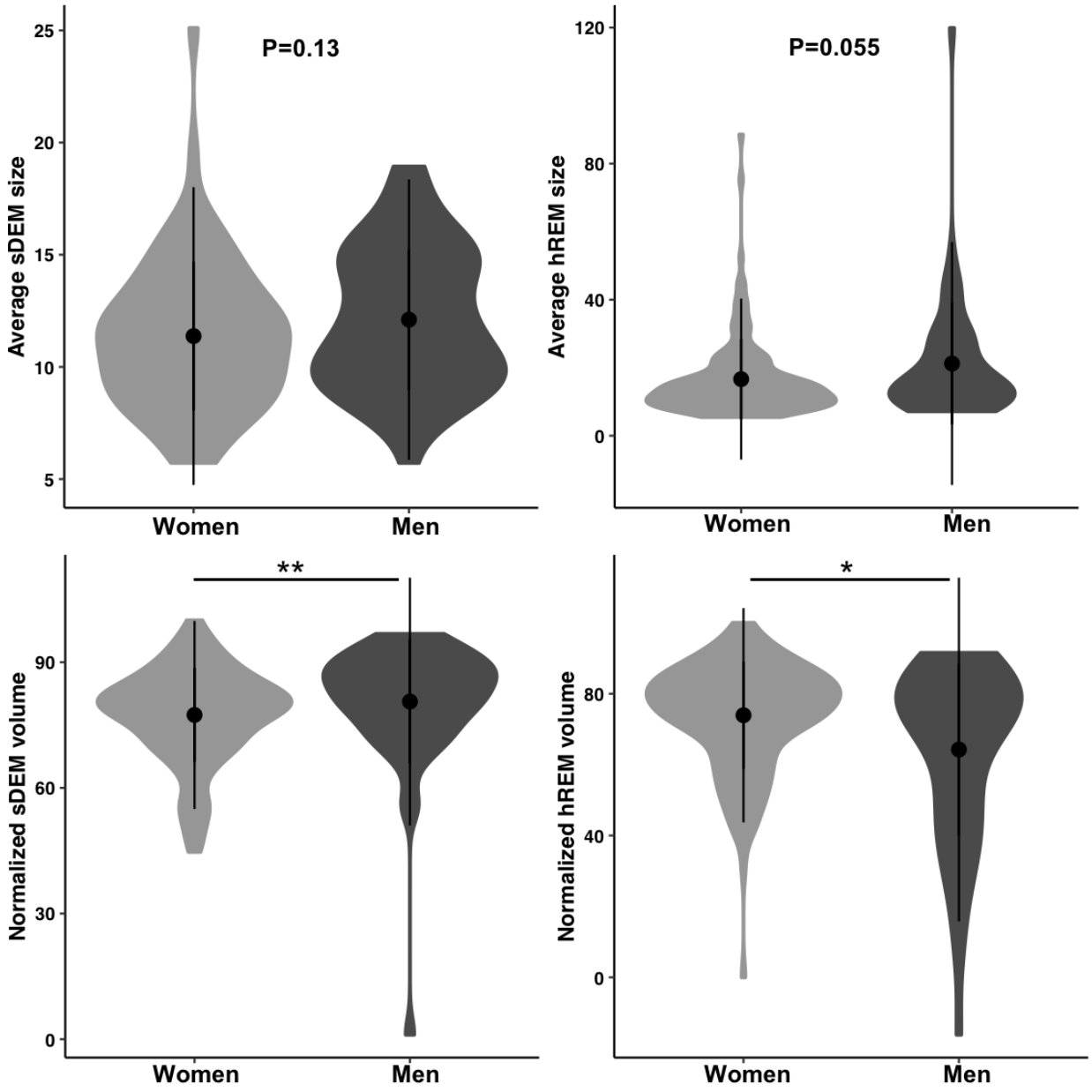

*Figure 5.9. The average size and normalized volume of different lesion types in women and men participants. Shown are violin plots of the mean, standard deviation, and range (density) of the data. Note: sDEM= severely demyelinated, hREM=highly remyelinated lesions. *p<0.05; **p<0.01.*

5.5 Discussion

In this study, we developed a percentile thresholding approach to identify 2 critical lesion types in MS participants based on histology-verified texture measures of conventional MRI. Using recognized percentile thresholds, this study found that most of the RRMS participants had both the sDEM and hREM lesions. Group-wise, the total normalized volume and mean texture of sDEM were greater than hREM, but the average size of hREM was larger than sDEM. Based on the PCA, GLCM-contrast and GLCM-dissimilarity were uncorrelated and contributed similarly in lesion separations. Further, the lesions from both types showed a high likelihood of distribution in the periventricular and deep white matter, with the hREM more aggregated than sDEM. While there was no significant age impact, the woman participants displayed less sDEM but more hREM than man participants, with men showing a trend for hREM to be larger than women.

Percentile statistics has shown enormous promise in classifying tissue types or disease activity in various studies, including those in MS [68, 137, 138]. Based on MTR signal intensity inhomogeneity, a previous study used the same $25\%^{ile}$ and $75\%^{ile}$ thresholds to define tissues of highly repairing and damaging potential in MS lesions and normal appearing white matter [139]. In another study, by comparing different thresholds, the investigators showed that the $25\%^{ile}$ and $75\%^{ile}$ thresholds of GLCM-contrast and GLCM-dissimilarity were most feasible in differentiating de-and re-myelinated lesions using T2-weighted MRI following histology verification [21]. Similarly, the percentile approach has also shown utility in differentiating disease activities in MS. One study divided relapsing and progressive MS by using lesion and brain volume, and lesional myelin water fraction (MWF), and they discovered that the median, $25\%^{ile}$, and $75\%^{ile}$ of MWF, and $75\%^{ile}$ of lesion volume were the top ranking features [140]. Another study differentiated the

severity of RRMS participants based on their 25%^{ile} and 75%^{ile} of lesion load, where the 2 groups showed significant differences in brain microstructure as measures by diffusion MRI [138]. In the present study, we adopted the 25%^{ile} and 75%^{ile} thresholds based on two top-performing GLCM features (contrast and dissimilarity) as verified in histology. The observation that most of our RRMS participants showed both sDEM and hREM lesions is in accordance with a recent study showing that both lesion types exist in most MS subjects, with only some presenting with a dominant lesion type [133].

Texture is an intrinsic characteristic of a tissue and can be determined by the degree of coarseness, fineness, irregularity, and complexity. Image textural information has shown to be valuable for tissue discrimination and classification [106]. In general, a repaired tissue is expected to exhibit a fine texture pattern in MRI, whereas a damaged tissue such as demyelination would create a heterogeneous texture [20, 28]. GLCM-contrast and GLCM-dissimilarity are leading measures of texture coarseness and heterogeneity [106, 152]. Indeed, we detected greater GLCM-contrast and GLCM-dissimilarity in sDEM than hREM lesions in the present study. Our PCA analyses further showed that the two GLCM texture features were independent and contributed similarly to the first PCs in lesion identification based on individual lesion texture values, suggesting that using either texture feature alone may be feasible in similar studies.

With respect to lesion type analyses, this study detected a smaller average lesion size but greater total normalized lesion volume in sDEM than hREM. One of the critical reasons for sustained disease progression in MS is the lack of remyelination or repair [197, 198]. Therefore, it was not surprising to find in this study that the total normalized lesion volume of sDEM was significantly

greater than hREM. This is also consistent with prior evidence. Based on diffusion MRI measures of 59 MS participants (53 being RRMS), a study performed cluster analysis that grouped lesions into 2 severity types. They found that the volume of more severe lesions was higher than less severe lesions [133]. On the other hand, larger lesions would be expected to have more heterogeneous structure due to the higher likelihood of possessing inhomogeneous pathology across the lesion area. However, areas of remyelination might also more likely be present in larger lesions, given the evidence of preferably uneven repair in lesion regions in MS as documented in histology [8, 199]. Additionally, sDEM lesions could have a high degree of tissue loss, causing an atrophic change and therefore smaller size, which did not allow enough capacity for remyelination. Combined results might have contributed to the relatively better MRI texture regularity in hREM than sDEM. Nonetheless, a prior study involving two participants based on postmortem brains of progressive MS participants had also reported that smaller lesions might remyelinate more effectively than larger ones, although the sample size was small and disease phenotypes was different [200], deserving further investigation.

Our implementation of lesion distribution maps served as another valuable means to understand the identified lesion types. Previously, several studies have used lesion distribution maps to investigate lesion development in MS. One of them compared the pattern of lesion distribution between RRMS and SPMS participants [201]. They showed that the periventricular area was more subject to severe tissue injury than other brain white matter regions and the damage was more pronounced in SPMS than RRMS participants. Another study analyzed the change in spatiotemporal patterns of active lesions over time in RRMS participants, where they found that there was a reduction of active lesion development in major white matter tracts such as

corticospinal tract after treatment [202]. Nevertheless, there was lack of information on the distribution of de- and re-myelinated lesions in MS along with in vivo detection. In the current study, our probability distribution maps highlighted that both the sDEM and hREM lesions were highly distributed in the periventricular and deep white matter regions, with the hREM appearing mainly with a central brain localization as seen around the lateral ventricles and corpus callosum. While previous studies indicated that remyelination occurred more frequently in the subcortical than periventricular brain white matter in MS [203, 204], our findings suggest that strong remyelination may also happen in other brain areas. On the other hand, results of this study may not be completely contrary to prior evidence because our hREM would only represent lesions with the most degree of remyelination, not lesions with intermediate or mild degrees of repair. Another finding of this study was the limited brainstem lesions of both lesion types identified. This might be due to several factors, including the inherent lack of occurrence of MS lesions in the brainstem, and the challenge of imaging brainstem lesions [205]. Furthermore, brainstem lesions showed signs of early apoptotic oligodendrocyte changes [206] and significant volume loss was also evidenced in the brainstem of RRMS patients [207]. These pathological alterations might have resulted in a non-permissive environment in the brainstem for remyelination, consistent with the low number of brainstem hREM lesions detected in this study.

This study detected significant differences in total normalized lesion volume between sexes but not between age groups. Besides the strong differences in disease prevalence between sexes in MS, women and men also seem to show distinct disease outcome. Once initiated, the disease is likely to worsen faster in men than women [208, 209]. While various factors may play a role, our findings suggest that the higher total normalized volume of sDEM but lower total normalized

volume of hREM may indicate reduced repair in men. This may be contributory to the non-favorable disease course in men. Further, because the average size of hREM lesions was relatively larger in men than women, our findings also suggest indirectly that men have fewer hREM than women. The evidence on the impact of age on disease activity is mixed in the literature. Various studies have reported that the repair potential decreases in older MS participants than young ones [210, 211]. However, a recent study did not support this [212]. In that longitudinal study of 30 RRMS participants, the authors investigated the effect of age on intralesional tissue evolution using different MRI measures including neurite density and orientation dispersion indices, MTR, and T1 relaxometry. They divided participants into young (age<25th percentile) and older (age>75th percentile) groups and discovered that age did not affect the repair pattern of MS lesions in MRI [212]. Regarding clinical relevance, the literature evidence is scarce. Previously, a study classified brain white matter lesions of 53 RRMS and six progressive MS into two lesion types, respecting lesion severity and based on quantitative diffusion measurements. They found that the number and volume of the more severe lesion type were associated with disease severity and cognitive decline [133]. Nonetheless, the participant characteristics, sample size, and MR measurements are different between prior and current studies, and therefore direct comparison of results is difficult. Overall, the relationship between the identified lesion types and clinical measures deserves further investigation.

Our study has limitations. The focus was mainly on cerebral white matter lesions. While lesion injury and repair may be present in other parts of the brain including grey matter, the main purpose of this study was to investigate whether and how a method for lesion type characterization can be derived. Given the prevalence of inflammatory changes across the brain in RRMS, studying white

matter pathology seems reasonable. In addition, it was not possible to differentiate partial versus complete remyelination such as lesions fell between the two defined thresholds in this study. This was mainly due to the expected subtlety of structural changes associated with those lesion types or lesions based on intermediate thresholds, especially given the lack of pathological validation for living participants. Likewise, there was a lack of histological confirmation of the lesion types identified. Nonetheless, the MRI texture measures used here were well recognized and had previously been histology verified, increasing the likelihood of pathological specificity. Further, this study was limited to RRMS participants. Combining other participant groups would broaden the scope of the study. However, RRMS is the phenotype that has the most lesions with active de- and re-myelination. In the future, we seek to verify our findings using different datasets, assess other types and areas of lesions, and correlate MRI results with disease development or intervention.

In summary, characterization of lesion severity in vivo is fundamental for a thorough understanding of disease evolution and therapeutic impact in MS. Using histology verified brain MRI texture measures and a simple percentile thresholding approach, this study shows the potential to address an ongoing challenge in MS management. Specifically, conventional clinical imaging protocols can identify the number and location of MS lesions and determine the amount of de- and re-myelination. This is useful for treatment decisions and monitoring. It may also be useful in clinical trials as a measure of lesion repair.

Chapter 5: Statistical texture mapping of clinical brain MRI indicates repair in acute brain lesions of people with multiple sclerosis following domperidone add-on treatment

6.1 Background

The ability to characterize tissue changes in MS lesions over time is crucial for monitoring disease progression and treatment response. However, despite the strong effort in method development, there is still lack of MRI methods satisfying the above purpose in vivo. In this project, based on both postmortem and in vivo studies, previous chapters have shown the potential of GLCM texture features from T2/FLAIR brain MRI for differentiating de- and re-myelinated lesions in MS. Using the two top-performing GLCM features, GLCM-contrast and GLCM-dissimilarity, the goal of this chapter was to evaluate how tissue changes in acute brain MRI lesions in RRMS participants imaged over time. This study took advantage of a local clinical trial, where eligible participants were followed over 32 weeks with and without add-on treatment with a candidate remyelination agent, domperidone. Part of the results in this chapter has been published at an international conference as an abstract [213].

6.2 Introduction

Multiple sclerosis (MS) is an inflammatory demyelinating and neurodegenerative disease of the central nervous system (CNS) [149], impacting more than 2.8 million people worldwide [1]. Particularly, MS is a lifelong disease starting primarily with young adults, causing paramount

physical and cognitive impairments [214]. Focal lesions remain to be the hallmark of MS pathology [149]. Following tissue damage such as demyelination, remyelination happens in MS lesions [4], especially in the acute ones [6, 7]. In addition to restoring the myelin sheath that improves nerve conduction, remyelination also provides trophic support to the axons, which foster neuroprotection. With pertinent treatment, it is possible to further enhance these benefits of remyelination [4, 5]. However, assessing tissue repair in MS in vivo is challenging [10].

Magnetic resonance imaging (MRI) is an important imaging modality for measuring MS. Towards assessment of specific tissue changes, much effort is manifest using advanced MRI, such as magnetization transfer, myelin water, and diffusion imaging [215]. Chen et al. used magnetization transfer ratio (MTR) for evaluating de- and re-myelination in gadolinium-enhancing lesions and they reported significant decrease and increase in MTR consistent with de- and re-myelination, respectively [68]. In a longitudinal study of myelin water fraction in two MS participants with active disease, myelin water fraction showed decrease with myelin loss, whereas its recovery was consistent with repair [3]. Diffusion imaging-derived fractional anisotropy (FA) is also sensitive to myelin. In a study by Friedrich et al. FA revealed various correlations with myelin content and axonal density in human corpus callosum [151]. However, the utility of advanced MRI techniques for measuring remyelination or repair needs further validation. Further, in many clinical settings, these advanced techniques are not part of the standard imaging protocols. Conventional MRI is common and has an established role in the diagnosis and management of MS. Together with advanced image analysis techniques, conventional MRI may play an important role in assessing tissue injury and repair [17], overcoming the typical issue of lower pathological specificity based on image signal intensity alone [216].

Previous research suggests that the texture of MRI is highly associated with the degree of MS tissue integrity [17, 20]. Higher tissue heterogeneity creates greater coarse texture, where in MS, the underlying substrates may include demyelination, inflammation, and axonal injury [17]. Employing a statistical texture analysis approach known as grey level co-occurrence matrix (GLCM), previous research has shown that GLCM-contrast and GLCM-dissimilarity in T2-weighted MRI discriminate histology-confirmed MS lesion types with de- versus re-myelination [146]. Also the texture measures were lower in remyelinated lesions than demyelinated lesions [141, 146, 217].

This study aimed to assess repair utilizing the identified GLCM measures in acute brain MRI lesions from people with relapsing-remitting MS (RRMS). The objectives included characterizing texture changes over time following treatment with domperidone as an add-on reparative therapy; comparing texture outcomes between treated and control groups, and compare between enhancing and non-enhancing lesions.

6.3 Materials and Methods

6.3.1 Participants

We used 3T brain MRI scans acquired from 17 RRMS participants recruited in a clinical trial of domperidone (clinicaltrials.gov identifier NCT024993049). The trial screening included 237 RRMS participants (173 females), age at screening: 18-60 years, age at onset: 7-56 years, Expanded disability status scale (EDSS) ranged 0-8.5 years, and disease duration ranged 1.4-35.6 years. As one of the key eligibility criteria, each participant had at least one gadolinium-enhancing

lesion on screening brain MRI (baseline), which indicated the acute nature of the lesions. At follow up, each subject also underwent 2 additional brain MRI scans at 16 weeks and 32 weeks respectively. Through a 2:1 randomization scheme, 12 participants received domperidone for 16 weeks as an add-on to their existing disease modifying therapies (DMTs), and 5 participants received regular DMTs only without add-on treatment as controls. Moreover, participants were split into two groups of low and high responses regarding the level of the prolactin hormone and were analyzed respectively. The high group had four times more prolactin response than the low group.

6.3.2 Imaging protocol

The MRI acquisition was performed on a 3T scanner (GE Healthcare, Discovery MR750, Milwaukee, United States). Imaging protocols included both conventional and advanced MRI. This study focused on the former, especially T1-weighted and FLAIR MRI. The protocol for FLAIR was: repetition time (TR) / echo time (TE) = 7000/128 ms, field of view (FOV) = 240×240 mm^2, matrix = 512×512, and slice thickness = 1mm. For T1-weighted MRI, the protocol was: TR/TE = 6.5/2.9 ms, FOV = 192×256 mm^2, matrix = 192×256, and slice thickness = 1mm. The total imaging time is within one hour.

6.3.3 Image pre-processing

The MRI scans were pre-processed in several steps to improve quality and consistency. The first step was brain extraction using the BET method included in the FSL software (Oxford, UK). This was followed by intra-subject co-registration with FLIRT algorithm of FSL. FLAIR images of each subject at baseline were co-registered to the pre-contrast T1. The co-registered baseline

FLAIR scans were then used for lesion segmentation. Subsequently, FLAIR images at follow up scans were also registered to the baseline pre-contrast T1 for further analysis. The next step was image denoising using median and mean filters, built-in ImageJ (version 1.50i, NIH, USA), The median filter is a non-linear filter which is used for denoising various types of noises, including Gaussian noise, and preserves image sharp details [92]. Whereas mean or average filter is a linear filter and is applied to remove the speckle noise [92]. The last step was image signal intensity normalization, scaled to the range 0-255 with an in-house program.

6.3.4 Lesion segmentation

Lesion segmentation was done on co-registered FLAIR images employing the automatic lesion segmentation tool (LST, v3.0.0, SPM12) [191]. The LST is freely available and has shown to be a competitive lesion identification method in both cross-sectional and longitudinal studies [218]. After the automatic process, the segmented lesions were manually corrected to improve accuracy. This includes removal of areas overlapping with the cerebral ventricles to reduce partial volume effects or other undesired impact such as motion artifact. For similar reasons, lesions smaller than 5 pixels (5 mm^2) were also eliminated (Figure 5.1). Lesion segmentation results, including the presence of gadolinium-enhancing lesions were confirmed by a neuroradiologist.

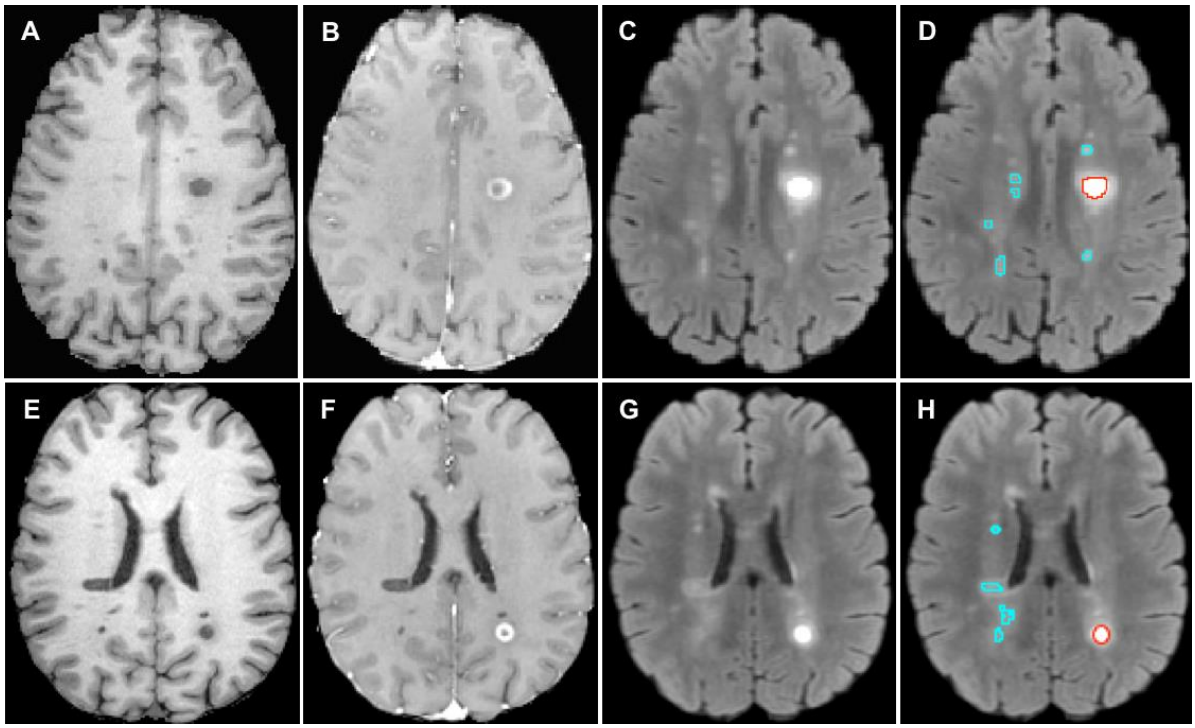

Figure 6.1. Example MR images and the segmented lesions from two RRMS participants. Shown are the pre-contrast T1 (A, E), post-contrast T1 (B, F), and FLAIR images without (C, G), and with (D, H) overlay of lesion outlines. Red and blue outlines indicate enhancing and non-enhancing lesions, respectively. Note: RRMS: relapsing remitting multiple sclerosis.

6.3.5 Image texture analysis

Texture analysis used the GLCM technique focusing on FLAIR MRI as it detects the most MS lesions [219]. The GLCM is a statistical texture analysis technique that calculates how often pairs of pixels separated by a specified distance with alignment in a certain direction occur in an image. Given that small distances were preferred for detecting fine structures [165], this study used a distance of one pixel. In addition, GLCM features can be quantified in four orientations: 0°, 45°, 90°, and 135° [106], with each direction associated with fourteen features initially [20]. The current study used the average texture from all four directions with a concentrated on two features: contrast

and dissimilarity. Prior evidence suggested that these feature options provided the most promise in texture classification [195], including differentiation of de- and re-myelinated lesions in MS as verified using histology-informed brain MRI [146]. Further, based on a scikit-image implementation in Python (version 2.7), our GLCM computation took a sliding window approach. A small window sized of 3x3 pixels was used, which allowed to detect fine textural information [220]. Repeating this process led to the creation of texture maps per image slice, covering the whole brain (Figure 5.2-5.4). GLCM-contrast detected local signal intensity variation reflecting the coarseness of a tissue structure, whereas GLCM-dissimilarity measured the variation of grey-level pixel pairs, highlighting image heterogeneity [221]. For comparison, texture analysis in both enhancing and non-enhancing MS lesions were conducted. Outcomes were assessed both group-wise and participant-wise over time.

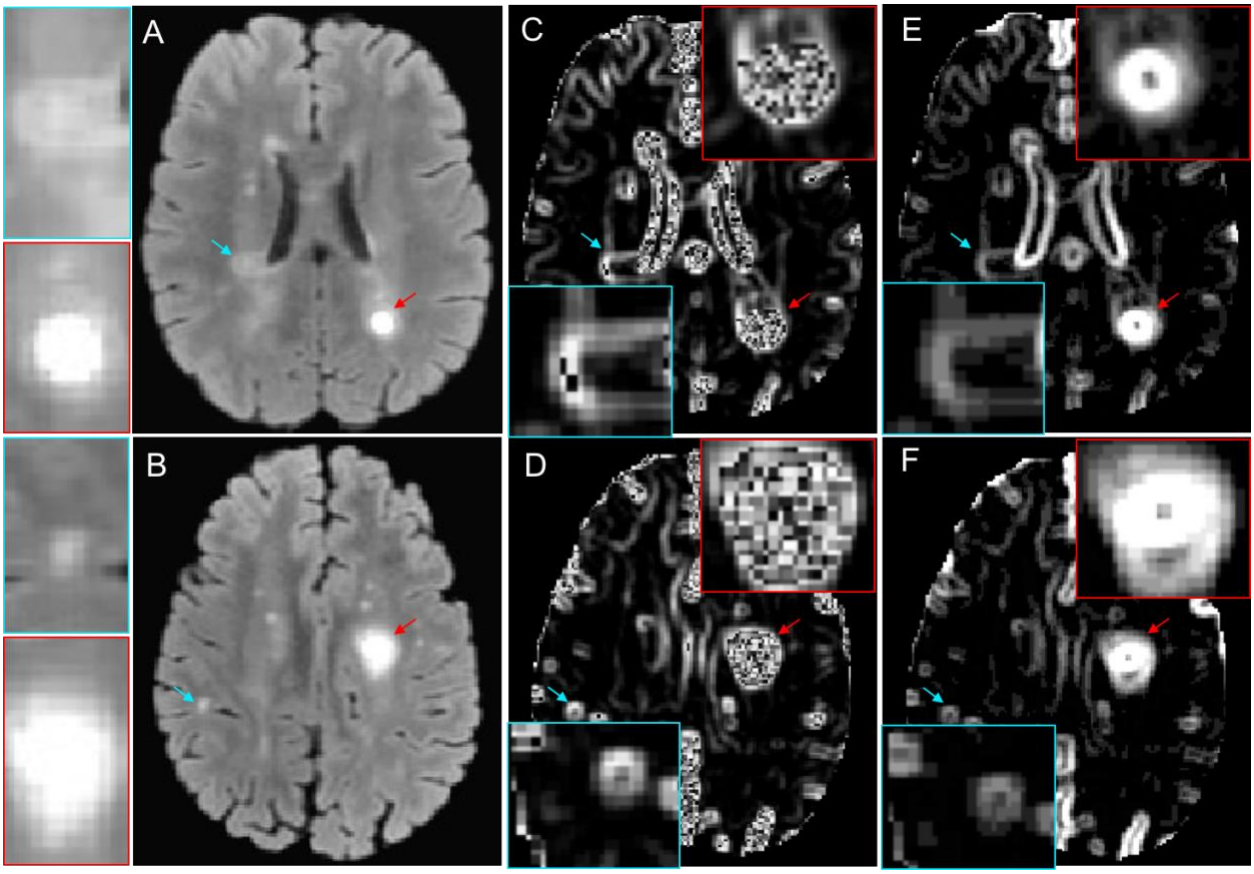

Figure 6.2. Examples FLAIR images and the associated texture maps at baseline from two RRMS participants (one row per participant). Shown are axial brain FLAIR MRI (A,B), and GLCM-contrast (C,D) and GLCM-dissimilarity (E,F) averaged from all 4 directions of the texture calculation. The red and blue arrows represent enhancing and non-enhancing lesions, respectively, so do the color matching boxes for an enlarged view of them derived from FLAIR (left most column) and texture images (insets in C-F) . Note: RRMS: relapsing remitting multiple sclerosis.

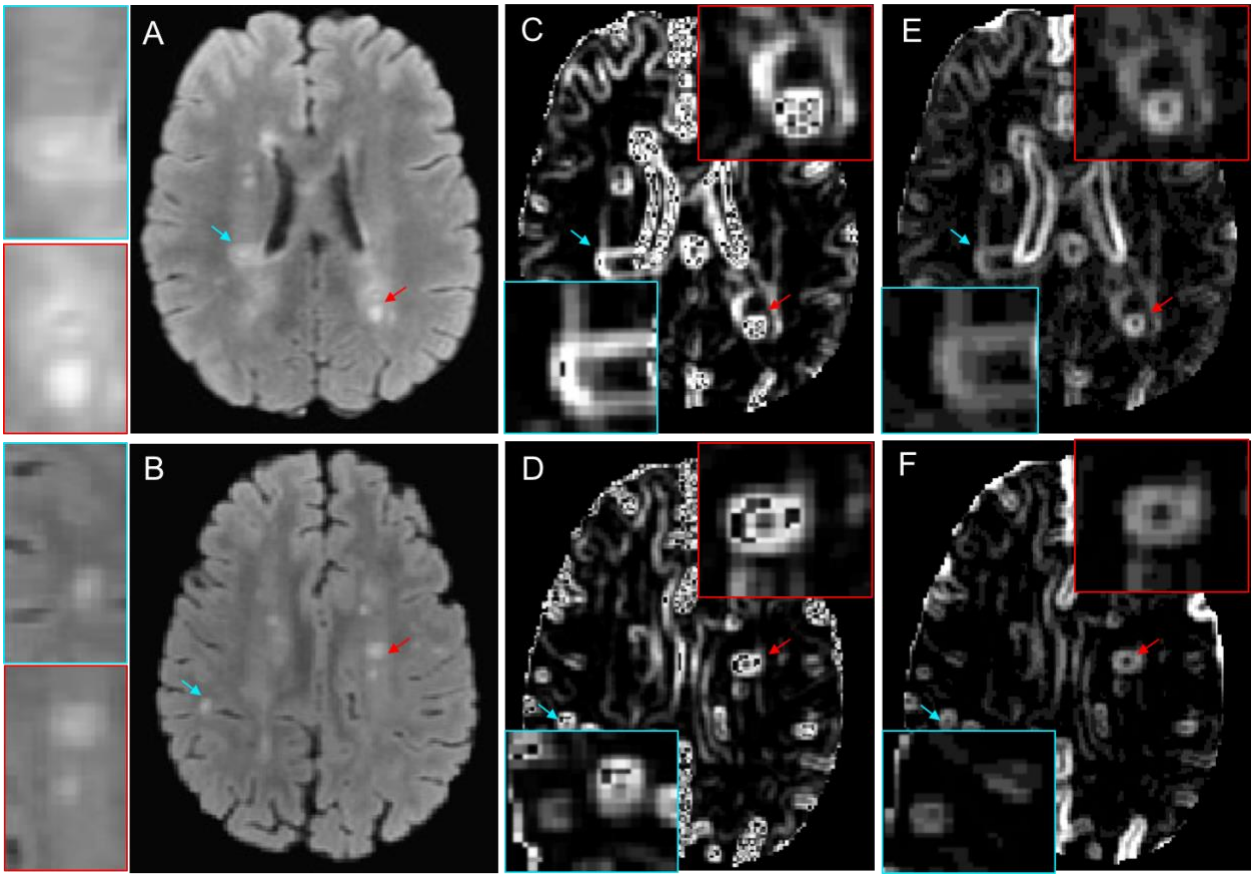

Figure 6.3. Examples FLAIR images and the associated texture maps at week16 from two RRMS participants (one row per participant). Shown are axial brain FLAIR MRI (A,B), and GLCM-contrast (C,D) and GLCM-dissimilarity (E,F) averaged from all 4 directions of the texture calculation. The red and blue arrows represent enhancing and non-enhancing lesions, respectively, so do the color matching boxes for an enlarged view of them derived from FLAIR (left most column) and texture images (insets in C-F) . Note: RRMS: relapsing remitting multiple sclerosis.

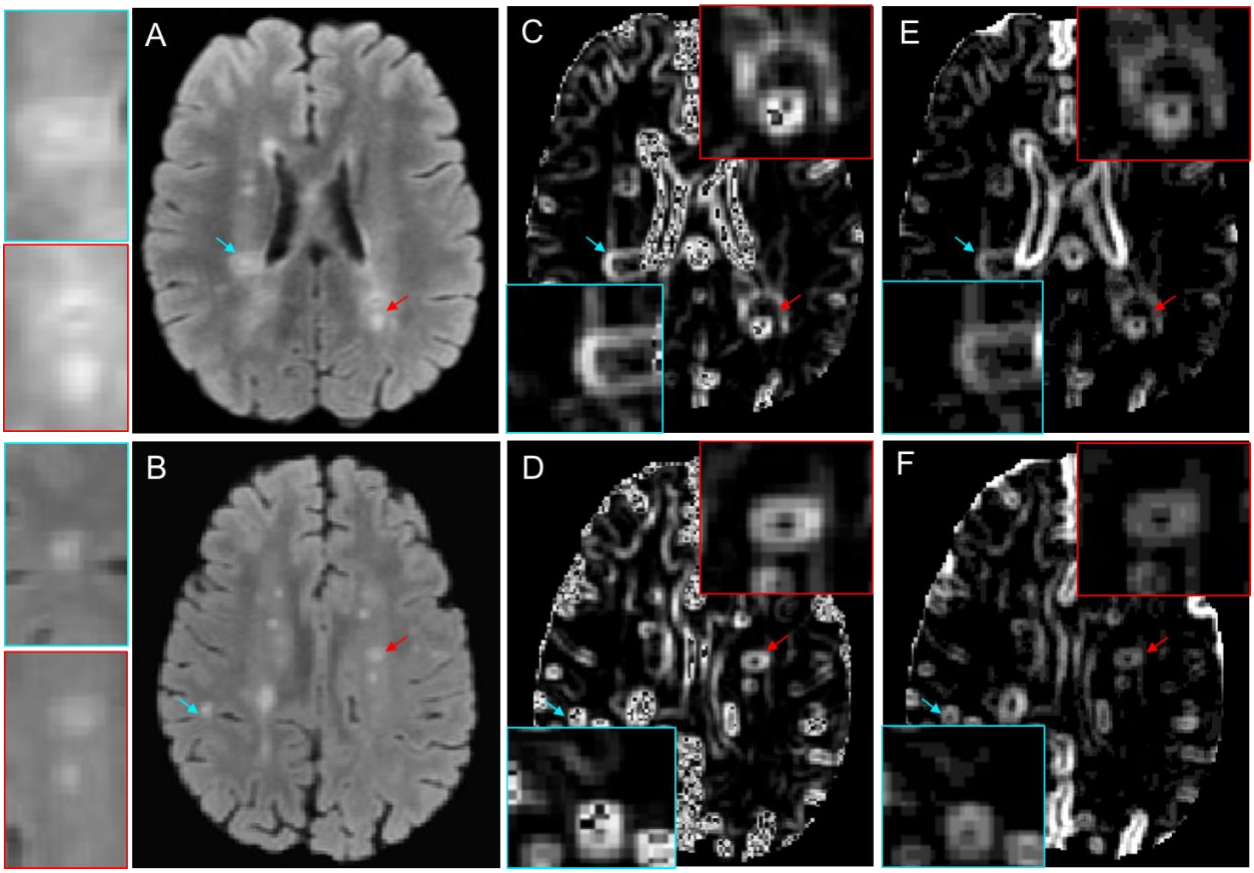

Figure 6.4. . Examples FLAIR images and the associated texture maps at week32 from two RRMS participants (one row per participant). Shown are axial brain FLAIR MRI (A,B), and GLCM-contrast (C,D) and GLCM-dissimilarity (E,F) averaged from all 4 directions of the texture calculation. The red and blue arrows represent enhancing and non-enhancing lesions, respectively, so do the color matching boxes for an enlarged view of them derived from FLAIR (left most column) and texture images (insets in C-F) . Note: RRMS: relapsing remitting multiple sclerosis.

6.3.6 Statistical analysis

A linear mixed effect model was used to assess texture changes over time within individual groups, and between groups at different timepoints. The fixed variables were GLCM-contrast and GLCM-dissimilarity, and random effects included subjects and ROIs. In each test, the mean texture values

per lesion were used. A p value ≤ 0.05 was set for statistical significance. Additionally, the effect size, which is a measure of the mean difference, was also calculated for the treatment groups using Cohen's F statistics [222]. The effect size represented the strength of the significance, such as differences between variables. It does not depend on the sample size and therefore could be a valuable metric to compare outcomes across different studies [223]. The Cohen's F statistics was defined by 3 criteria, with f^2 = 0.02, 0.15, and 0.35 indicating small, medium, and large effect respectively [222]. The R software (version 3.6.3) was used for all statistical analyses [172].

6.4 Results

6.4.1 Sample Characteristics

There were 38 gadolinium-enhancing lesions identified from the 17 RRMS participants. Data for texture analysis were available from these participants at all three timepoints. At baseline, each patient had 1(one) to 9 gadolinium-enhancing lesions. The enhancing lesion size ranged 5-75 mm^2. Regarding non-enhancing lesions, there were 592 lesions in total, ranging from 14.98-34.43 mm^2 per patient. Of the 17 participants, the mean age was 40.88 years, disease duration was 12.48 years, and disability (EDSS) score was 2.08 (Table 5.1). Between groups, the mean age (years), disease duration (years), and EDSS were 41.94, 13.35, and 1.79 for the 12 participants treated with the domperidone add-on, and 38.34, 10.42, and 2.8 for non-add-on treatment participants. Between the high and low prolactin groups, the age (years), disease duration (years), and EDSS were 39.96, 12.06, 2.5 versus 44.04, 14.12, and 1, respectively.

Table 6.1: Demographic data

MS case	Age at screen (quartile)	MS duration (quartile)	EDSS	Sex	Active lesions	Total lesions
1	1st	1st	2	female	3	23
2	4th	3rd	1	female	1	50
3	3rd	4th	2	female	1	16
4	1st	1st	2	female	1	16
5	1st	1st	3	female	1	22
6	4th	4th	4	female	1	38
7	1st	2nd	1.5	female	6	19
8	1st	3rd	2.5	female	1	37
9	1st	2nd	1	female	3	36
10	3rd	2nd	3.5	male	1	51
11	2nd	3rd	1.5	female	2	24
12	4th	3rd	1.5	female	1	23
13	4th	4th	0	female	1	26
14	1st	2nd	4	male	1	13
15	1st	2nd	3	female	9	60
16	2nd	3rd	1.5	male	4	94
17	2nd	4th	1.5	female	1	82
Mean/Std	40.88/9.57 **(**years)	12.48/6.28 **(**years)	2.08/1.1	-	2.23/2.25	36.3/23.53

Note: Quartiles are used for age and disease duration representations.

6.4.2 Outcomes on gadolinium-enhancing lesions

For the domperidone add-on treatment group, both GLCM-contrast and GLCM-dissimilarity was significantly lower at follow up scans than baseline. Compared to baseline, it was 21.11 versus

27.17 (p=0.04) at week16 and 17.51 versus 27.17 (p=0.0006) at week32 for GLCM-contrast. For GLCM-dissimilarity, it was 3.5 versus 7.89 and 2.86 versus 7.89 at week16 and week32, respectively (p=0.0001 for both timepoints). Cohen's F statistics found that the $f^2 = 0.41$ for GLCM-dissimilarity and $f^2 = 0.32$ for GLCM-contrast, indicating high and medium effect sizes. For the control group, the GLCM-contrast was lower at week32 than baseline: 18.39 versus 32.94 (p=0.003). In addition, GLCM-dissimilarity was lower at both follow up scans than at baseline, and it was 4.14 versus 14.13 and 2.7 versus 14.13 at week16 and week32, respectively (p=0.0001). Cross-sectionally, there were no significant differences in GLCM-contrast between control and treatment groups at any time points. The GLCM-dissimilarity was higher in the control than in the treatment group at baseline only (7.89 versus 14.13, p=0.0011). We found no significant difference between week16 and week32 texture in any measure in either treatment group (Figure 5.5).

Participant-wise analysis showed a similar trend except that the GLCM-contrast outcomes at week16 and week32 versus baseline were not significant in the domperidone add-on treatment group, and the change in controls was only significant at wee32 from baseline (35.04 (standard deviation = 3.48) versus 17.02 (standard deviation = 11.89), p = 0.04). Regarding GLCM-dissimilarity, it was significantly lower at follow up in both controls (3.7 (standard deviation = 1.71) versus 14.37 (standard deviation = 7.05) at week16, p = 0.008; and 2.6 (standard deviation = 1.16) versus 14.37 (standard deviation = 7.05) at week32, p = 0.005), and the treatment group (4.34 (standard deviation = 1.49) versus 7.78 (standard deviation = 4.92) at week16, p = 0.02; and 3.52 (standard deviation = 1.87) versus 7.78 (standard deviation = 4.92) at week32, p = 0.006; Figure 5.6 & Figure 5.7).

6.4.3 Outcomes on Non-enhancing lesions

In non-enhancing lesions, there was no significant difference between follow up and baseline scans in any texture measure in any group. Specifically, in the treatment group, the GLCM-contrast was 26.93, 26.68, and 26.41 at baseline, week16, and week32, respectively (baseline versus week16: p=0.9, and baseline versus week32: p=0.3). GLCM-dissimilarity was 5.2, 5.3, and 5.3 at baseline, week16, and week32 (baseline versus week16: p=0.9, and baseline versus week32: p=0.8). For the control group, contrast was 30.56, 29.17, and 29.34 at baseline, week16, and week32, respectively (baseline versus follow up scans (week16 and week32): p=0.5). Furthermore, GLCM-dissimilarity was 6.12, 5.58, and 5.67 at baseline, week16, and week32 (baseline versus week16: p=0.5, and baseline vs week32: p=0.6). Cross-sectionally, GLCM-contrast was lower at week32 in the treatment than control group (26.41 versus 29.34, p=0.04) (Figure 5.8).

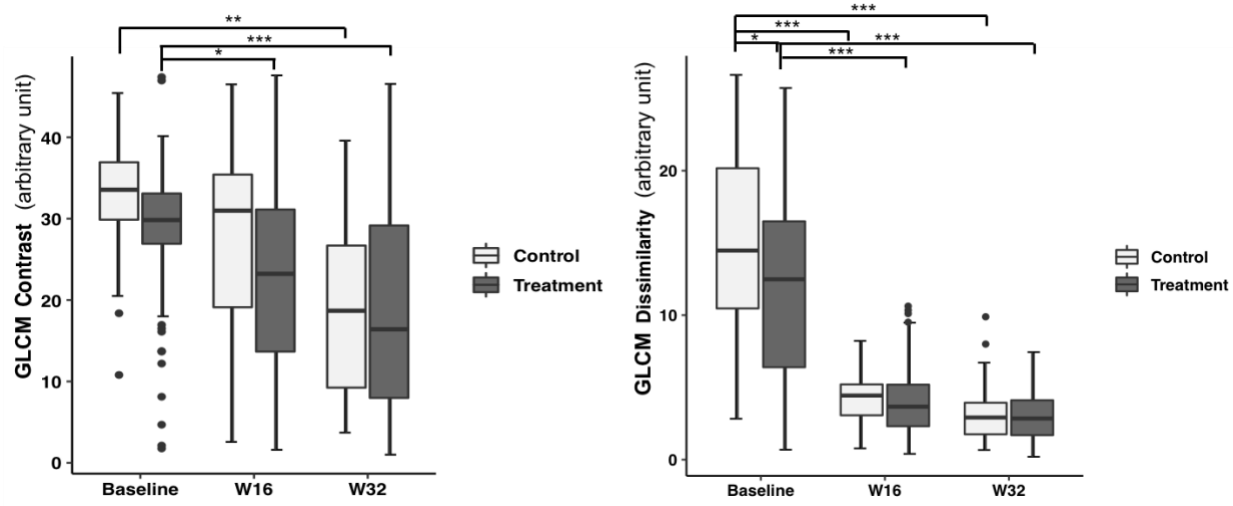

*Figure 6.5. Longitudinal texture analysis outcomes of gadolinium-enhancing lesions by group. Shown are GLCM-contrast and GLCM-dissimilarity texture acquired from FLAIR MRI and measured at baseline and at week16, and week32. The stars indicate significance levels: *p<0.05; **p<0.01; ***p<0.001. The boxes indicate interquartile range (IQR), the lines represent the median, and the grey dots represent the mean.*

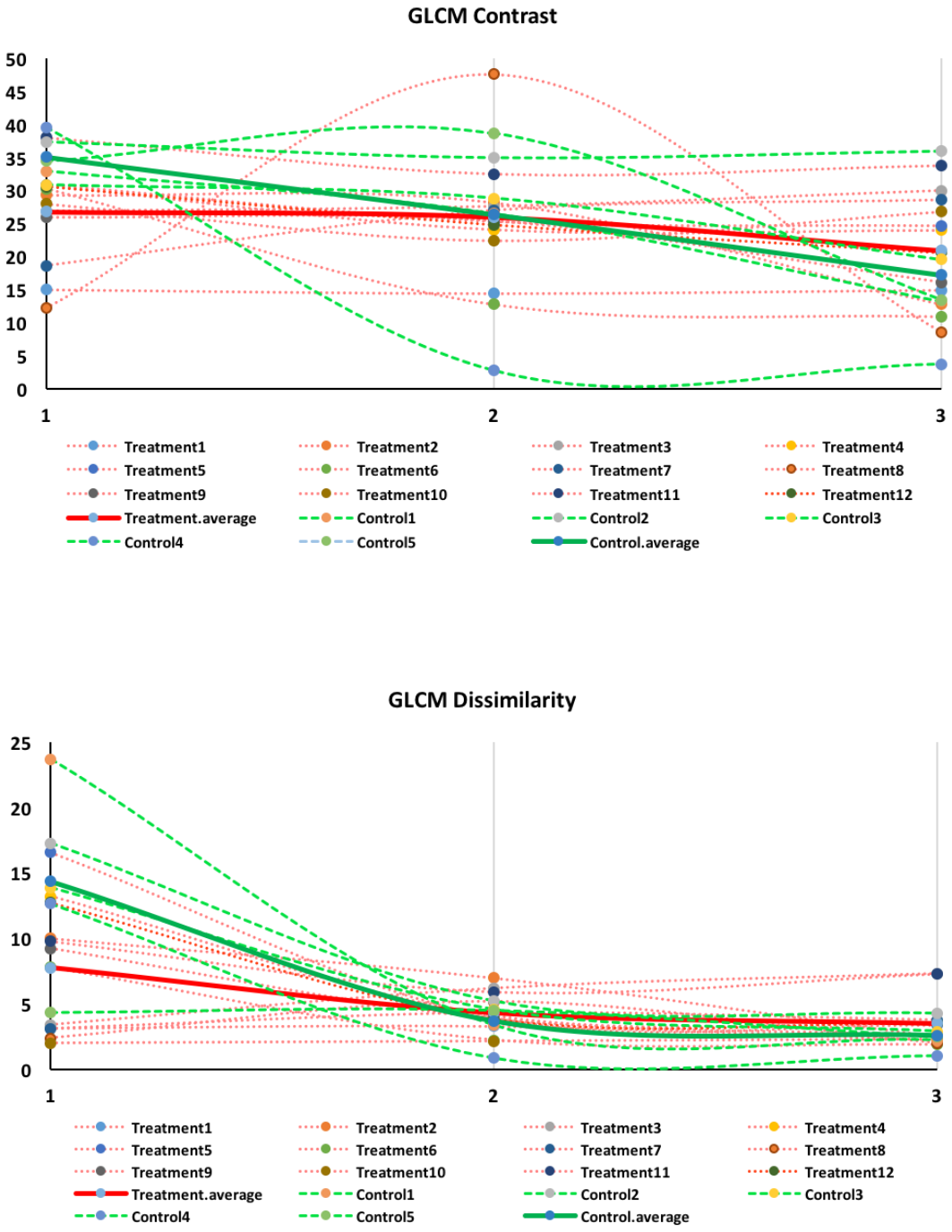

Figure 6.6. Participant-wise longitudinal texture changes of gadolinium-enhancing lesions by group. Most of the participants showed texture recovery (GLCM-contrast and GLCM-dissimilarity decrease) overtime with more pronounced changes from baseline to week32. The solid lines indicate the mean values across control (green) and treatment (red) groups.

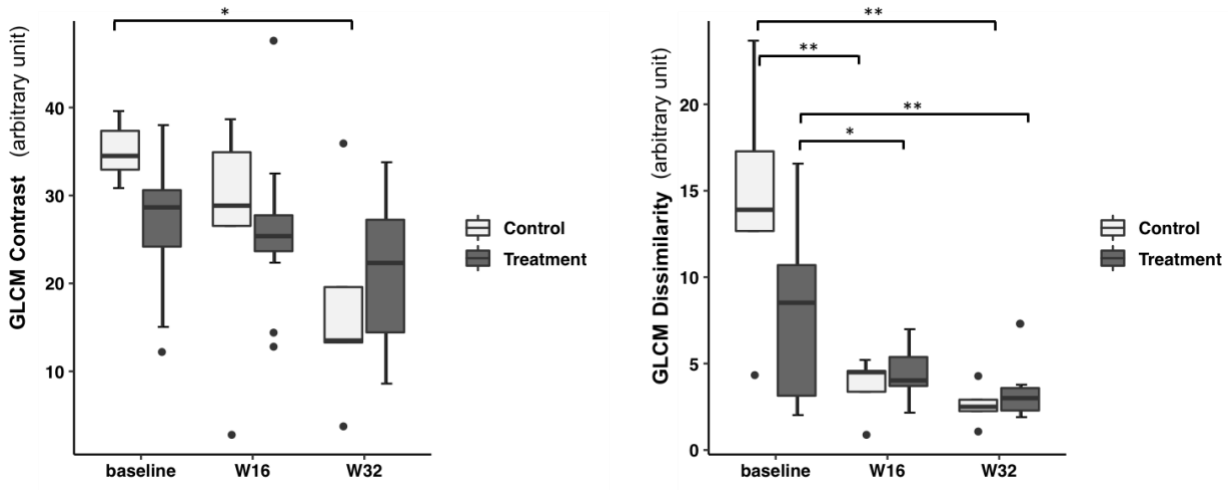

*Figure 6.7. Participant-wise longitudinal texture analysis outcomes of gadolinium-enhancing lesions by group. Shown are GLCM-contrast and GLCM-dissimilarity texture acquired from FLAIR and measured at baseline and at week16, and week32. The stars indicate significance levels: *p<0.05; **p<0.01; ***p<0.001. The boxes indicate interquartile range (IQR), the lines represent the median, and the grey dots represent the mean.*

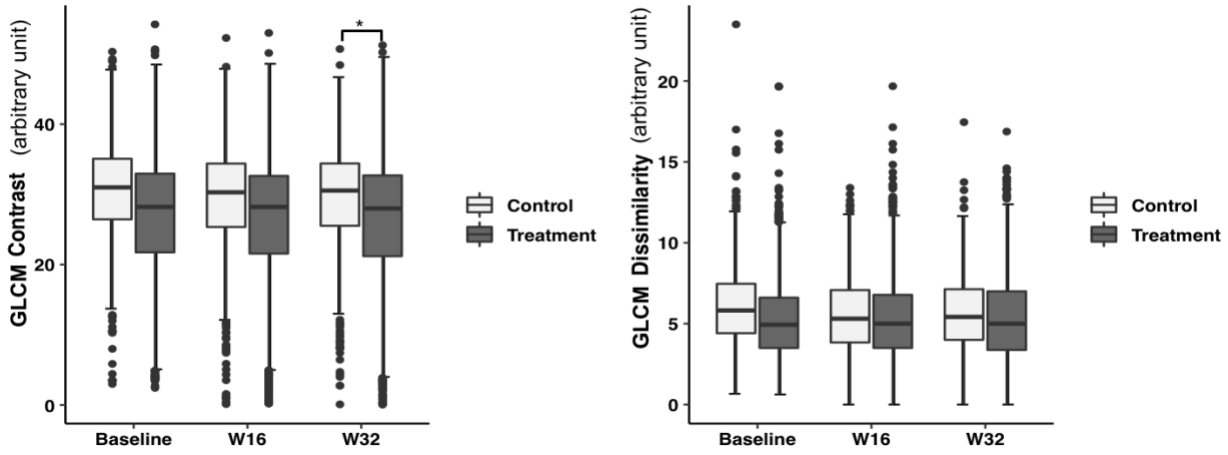

*Figure 6.8. Longitudinal texture analysis outcomes of non-enhancing lesions by group. Shown are GLCM-contrast and GLCM-dissimilarity texture acquired from FLAIR and measured at baseline and at week16, and week32. The stars indicate significance levels: *p<0.05; **p<0.01; ***p<0.001. The boxes indicate interquartile range (IQR), the lines represent the median, and the grey dots represent the mean.*

6.4.4 Outcomes on high and low prolactin groups

This analysis focused only on enhancing lesions of the domperidone add-on treatment group as there was no significant change over time in non-enhancing lesions of the participants as shown above. In the high prolactin group, GLCM-contrast was lower at both week16 (17.09 versus 26.72 p=0.011) and week32 (15.49 versus 26.72 p=0.003) than baseline. But the measure did not change significantly over time from baseline in the low prolactin group (p=0.9 and p=0.1 at week16 and week32, respectively). Regarding GLCM-dissimilarity, the high prolactin group demonstrated lower values at week16 and week32 than baseline, measured at 3.28 versus 7.4 (p=0.002) and 2.6 versus 7.4 (p=0.0005) over time. The low prolactin group had also shown significantly lower GLCM-dissimilarity at week16 and week32 than baseline. It was 3.85 versus 8.64 (p=0.01) at week16 and 3.25 versus 8.64 at week32 (p=0.004). Cross-sectionally, GLCM-contrast was significantly lower in the high prolactin group compared to the low prolactin group at week16 (17.09 versus 27.33, p=0.04) (Figure 5.9).

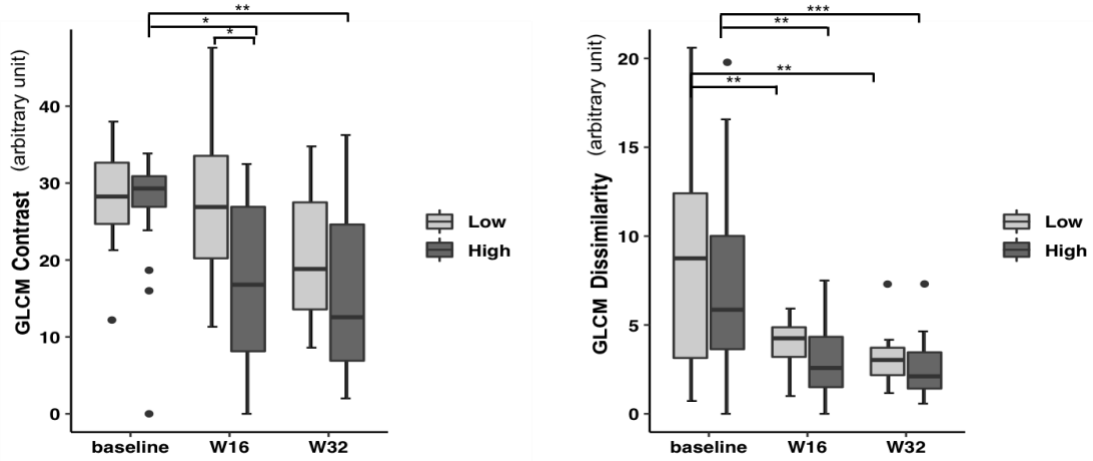

Figure 6.9. Longitudinal texture analysis outcomes of gadolinium-enhancing lesions in high and low prolactin groups. Shown are GLCM-contrast and GLCM-dissimilarity texture acquired from FLAIR MRI and measured at baseline and at week16, and week32. The stars indicate significance

*levels: *p<0.05; **p<0.01; ***p<0.001. The boxes indicate interquartile range (IQR), the lines represent the median, and the grey dots represent the mean.*

6.5 Discussion

In this study, we employed a texture-mapping approach of GLCM to assess tissue structural alterations in acute brain MRI lesions from RRMS participants with and without domperidone add-on treatment. Both GLCM-contrast and GLCM-dissimilarity in FLAIR MRI demonstrated significant improvement over time compared to baseline in the acutely enhancing lesions, more prominent in the add-on than control group. In comparison, the changes in non-enhancing lesions were not significant in either variable. Among the add-on treatment group, while dissimilarity improved in both high and low prolactin subgroups, only the high prolactin subgroup showed significant recovery in GLCM-contrast based on enhancing lesion analysis.

Texture is a characteristic that dictates the pattern and regularity of a tissue structure [105]. Different methods exist for quantifying image texture in brain MRI [20]. The GLCM is a well-recognized second order statistical texture analysis technique that assesses the joint probability of pixel pairs as texture features [105]. Injured tissues such as demyelinated lesions in MS contain diverse pathological components that would cause heterogenous texture patterns. Remyelination or repair in the lesions such as myelin sheath restoration and clearance of myelin debris should result in improvement in tissue regularity and hence fine texture patterns, more similar to that of a normal tissue [179, 180]. Both GLCM contrast and dissimilarity reflect tissue heterogeneity. While the reduction in inflammation and edema can also contribute to lesion recovery [224, 225], the sequential improvement in our histology-verified texture measures in acute MS lesions shown in

the current study suggests repair such as remyelination. These results are consistent with prior findings in brain MRI texture analysis in MS, which showed using a local time-frequency based method that coarse texture recovers with resolution of acute MS lesions [141]. Further, using postmortem brain samples of MS participants, another study confirmed that the degree of texture heterogeneity was strongly associated with the extent of demyelination and axonal injury, and at a lesser extent, with neuroinflammation [27].

The significant improvement in image texture over time is manifest only in the acutely enhancing lesions, not the non-enhancing lesions. In MS, various studies have demonstrated that acute lesions have the most capacity to repair [6, 7]. Acute lesions feature more pro-remyelinating inflammatory changes and a higher density of oligodendrocyte cells due to accelerated differentiation of oligodendrocytes precursor cells compared to non-acute MS lesions, fostering a permissive repair environment [226]. Notably, most of the texture improvement occurred over the period of 16 weeks from baseline in the examined acute MS lesions. The GLCM-contrast and GLCM-dissimilarity appeared to be stable at 32 weeks compared to 16 weeks, but there were no significant differences between the two timepoints in any measure. This phenomenon may be in line with findings that the repairing capacity of acute MS lesions decreases with the chronicity of the lesions [226, 227].

There were more significant texture results detected in the treatment group than the control group, where both GLCM-contrast and GLCM-dissimilarity revealed a considerable effect size, highlighting their potential in detecting invisible tissue changes. In the literature, there have been several clinical trials focusing on remyelination in MS, such as that using clemastine, opicinumab, and GNbAC1 [228]. While with benefit, the findings are not conclusive. In the present study,

domperidone served as an add-on treatment to the regular DMTs of the RRMS participants. Given the increasing efficacy of current DMTs in MS [229, 230], it may be not too surprising to observe that both treatment groups showed considerable texture recovery in acute lesions. However, the additional favorite results in the add-on group may be related to the pro-remyelinatory effect of domperidone. Domperidone is a generic medication that may promote tissue repair in MS. Domperidone elevates the prolactin level of treated relapsing-remitting and secondary progressive MS participants [231]. Prolactin is a hormone that increases during pregnancy, and that is also when MS participants experience more frequent remission than usual [232]. In an animal model of MS, Zhornitsky et al. have shown that a higher level of prolactin might enhance remyelination [233].

Between texture measures, while the improvement in GLCM-dissimilarity over time was similar between control and treatment groups, the recovery in GLCM-contrast was more pronounced, the difference was significant at week16 and week32 compared to the baseline in the treatment group. Whereas it was only significantly different between baseline and week32 in the control group. The difference between GLCM-contrast and GLCM-dissimilarity outcomes might be due to their distinct sensitivity to tissue structural changes. In a previous histology-MRI study, GLCM-contrast outperformed GLCM-dissimilarity in classifying MS pathology including de- versus remyelinated lesions [146]. Likewise, GLCM-contrast was significantly lower in enhancing lesions of high prolactin group than low prolactin group at week16 in the current study. In non-enhancing lesion analyses, only GLCM-contrast detected a significant difference between treatment and control groups seen at 32 weeks of follow up. In participant-wise analysis, however, GLCM-dissimilarity detected significant changes in more groups than texture contrast, deserving further investigation.

Additional analysis of the treatment group revealed a connection between prolactin level and texture recovery in acute lesions of the participants. People with higher prolactin response after 16 weeks of domperidone add-on treatment showed greater texture improvement than low prolactin response, particularly in the GLCM-contrast measurement. In fact, there was no significant improvement in GLCM-contrast at either 16 or 32 weeks of follow up in the low prolactin response group, suggesting the sensitivity of serum prolactin level to the add-on treatment of domperidone. The effects of prolactin on the immune system are not fully understood. It has been shown to have both pro-remyelination and anti-inflammatory, as well as pro-inflammatory characteristics [232]. However, the combination of prolactin with the immunomodulating DMTs may be beneficial because immunomodulators may prevent the pro-inflammatory impact of prolactin [233]. Therefore, the increased texture recovery outcomes of the RRMS participants with high prolactin response may be more related to the pro-remyelination than inflammatory properties of domperidone, deserving further confirmation.

We note some limitations about the study. The sample size was small. Given the effectiveness of current DMTs for RRMS participants, the presence of enhancing lesions on treatment is increasingly rare. However, this study identified significant results in several aspects, including the strong evidence of repair such as remyelination in acute MS lesions. Next, this study included only RRMS. While limited by generalization between disease phenotypes, RRMS is the cohort holding the most number of acute lesions that are the driving force for repair in MS participants. Further, due to the nature of in vivo studies, it is impossible to confirm how the recovery of lesion texture is associated with the extent of inflammation and edema, both being common in acute MS lesions, besides remyelination. Nonetheless, our results are based on histology-verified measures that have shown the potential to differentiate myelin integrity in MS lesions. Further, texture

measures are more sensitive to tissue changes than inflammatory alterations [27, 141]. Further research aims to confirm the current findings using a larger sample size, compare changes between different MS or pre-MS phenotypes, and compare with outcomes using different techniques such as advanced MRI.

In conclusion, based on data from a prospective clinical trial of RRMS participants, this study detected significant changes in brain MRI texture in acute lesions over time, particularly people with high prolactin response following domperidone add-on treatment. Given that the texture measures have shown the promise in differentiating de- and re-myelinated lesions in MS based on histology-informed brain MRI, the improvement in acute lesion texture strongly suggest repair or remyelination. Overall findings indicate the feasibility of combining advanced texture analysis with conventional MRI for assessing tissue recovery in clinical studies. With further confirmation, this approach may prove to be invaluable for improved disease monitoring, and for discovery of new neuroprotection and reparative therapies, thereby advancing the prognosis of MS participants.

Chapter 6: Discussion and conclusion

7.1 Summary and contribution

MS lesions are characterized by a variety of pathological components including demyelination and remyelination [149]. This makes lesion properties highly heterogenous [185] and difficult to characterize in vivo. Quantification of tissue injury and repair in MS is crucial for accurate characterization of disease activity and development of new treatment strategies. This is particularly important for the discovery of neuroprotective or repair therapies as tissue repair is insufficient in many MS participants. The latter represents one of the key reasons for relentless disease progression in MS. There are various studies searching for MRI biomarkers of de- and re-myelination in MS, mainly using advanced MRI [133, 187]. However, there is still lack of imaging measures of lesion severity for clinical use. Based on either conventional or advanced MRI, texture analysis has been shown to be a useful technique for characterizing subtle tissue structural changes, with or without integrating with other analytics methods such as machine learning. In this thesis I have developed new approaches to evaluate MS pathology particularly related to injury and repair in MS lesions based on conventional and advanced MRI. Further, I have taken a translational approach that involves brain MRI from both postmortem samples and living MS participants as seen in the three different aims. My research is associated with several innovative points. For example, I have advanced the image pre-processing techniques for diffusion MRI including the addition of new noise reduction methods, which has allowed robust conduction of texture analysis using the typically challenging postmortem images of the modality. Related to this direction, I have also implemented the new texture calculation approach for diffusion MRI in MS. In contrast to the in-plane computation method done typically, my implementation uniquely assesses image

texture across individual diffusion directions around each pixel, which is expected to have improved sensitivity to tissue structural changes. Notably, this process also involves a novel diffusion interpolation method allowing to increase diffusion directional resolution to an almost arbitrary degree. The fact that increasing diffusion directions from 30 to 90 as done in this thesis without adding extra imaging time would be attractive for many clinical studies in the future.

First Aim, used pathology-informed brain MRI scans to validate the capability of MRI texture analysis measures for differentiating different MS pathologies and compared the metrics to common advanced MRI measurements. I calculated texture features using one of the most commonly used statistical approaches from classical T2-weighted MRI and diffusion MRI scans. Diffusion texture analysis utilized a novel approach to compute high-resolution diffusion texture, focusing on the distribution of diffusion along all directions per image pixel. This method has the advantage of taking full account of the angularity of diffusion within the microstructure of a voxel, which has been enhanced following orientation-interpolation of the original DTI data. This contrasts with the traditional method that analyzes parametric maps one slice at a time that doesn't take full account of the angularity of diffusion within each pixel and might be less sensitive to tissue alteration. Based on joint analysis with random forest models as a common type of machine learning algorithms, texture analysis in clinical brain MRI revealed the most promising indices in classifying different pathological types in the grey and white matter of MS brain. In particular, the GLCM-contrast and GLCM-dissimilarity in T2-weighted MRI has shown to be the most important imaging features for differentiating de- and re-myelinated lesions, driven primarily by those in brain white matter. Overall, this aim attests that texture measurements from T2-weighted MRI were more competitive in classifying tissue injury and repair, particularly those related to de- and

re-myelination in MS brain, compared to other advanced MRI measures studied, such as FA and MTR. Among all texture measures, T2-contrast and T2-dissimilarity were the most informative features in classifying lesion subtypes in white matter. However, in grey matter, T2-correlation was also selected as one of the most important features for tissue classification besides T2-contrast and T2-dissimilarity. The ex vivo MRI used here possess higher resolution than typical in vivo MRI. To confirm the findings, I have also done pilot experiments to compare texture outcomes from Aim1 using T2-weighted MRI with those derived using low, clinically equivalent, resolution MRI achieved by down-sampling the same images. The results have shown a similar trend in texture measures based on high- and low- resolution images, suggesting the utility of the texture analysis methods applied in this research. This is in line with the literature demonstrating the promise of texture analysis in tissue characterization using clinical MR images [16, 141, 234].

In the second aim, I developed a method using standard brain MRI from clinical MS participants based on the verified texture analysis approach from Aim1. The goal was to identify two critical types of MS lesions: sDEM and hREM and gain a preliminary understanding of how these lesion types are different between age groups and sexes. Texture analysis in this aim used FLAIR images given their greater utility in clinical studies for lesion detection than other MRI sequences in MS and similar studies. Based on MRI physics, FLAIR is highly similar to T2-weighted MRI in many ways and therefore their texture characteristics are expected to be equivalent. However, for confirmation purposes, I have done additional experiments. Through side-by-side comparisons using images from the same RRMS participants, I have found that texture patterns generated from T2-weighted and FLAIR MRI are indeed similar as shown by the 2 well-recognized image similarity comparison indices: SSIM and PSNR. Based on T2 FLAIR MRI from 200 RRMS

subjects participated in a screening process for a local clinical trial, this aim conducted texture analysis using an optimized GLCM method by focusing on two top-performing histology-verified metrics in differentiating de- and re-myelinated brain MS lesions: GLCM-contrast and GLCM-dissimilarity. In addition, I developed a percentile approach based on the ranking of texture values for lesion categorization. Then, based on the 2 groups of lesions classified, I also implemented a robust approach for characterizing the probability of lesions located in individual pixels of brain MRI. Using a similar scheme of percentile threshold, the MS participants under study were also classified into young (bottom 25%^{ile}) and old (top 25%^{ile}) groups.

The results showed that the sDEM lesions had a greater normalized volume, GLCM-contrast, and GLCM-dissimilarity but a smaller average size than hREM lesions. Both lesion types were detected in most participants and were highly distributed at deep white matter and periventricular areas. Further, the normalized volume of sDEM lesions was greater, while that of hREM lesions was smaller in males than females. None of these measures were different between age groups suggesting that the role of age in repair process in MS deserves further confirmation. The smaller size of sDEM compared to hREM might be due to a higher likelihood of tissue loss in the severely damaged lesions. Instead, the larger total normalized volume of sDEM than hREM may indicate the general notion of damage-dominance as well as lack of remyelination in many MS subjects. The worse finding in men compared to women in this study is consistent with the findings of other studies showing worse disease prognosis in men than women [235], as well as a higher tendency for pronounced remyelination in women than men [204].

Overall, percentile statistics of robust MRI GLCM measures showed promise for probing lesion pathology by identifying two distinct lesion types in living MS participants, critical for precise monitoring of disease activity and treatment impact. The different characteristics of sDEM and hREM lesions between males and females may help interpret the distinct disease progression trajectories between the sexes.

Further, in Aim3, I conducted a longitudinal analysis of MS participants examined at three time points to assess changes in MS lesions seen in brain MRI. This study focused on acute brain MS lesions that have shown the potential to repair more rigorously than non-acute lesions, from 17 RRMS participants eligible for the clinical trial of domperidone as an add-on treatment to the regular DMTs of the participants. For comparison, non-enhancing lesions from the same MS participants were also assessed. Based on T2 FLAIR brain MRI scans, this aim also focused on the two top-performing histology-verified texture measures: GLCM-contrast and GLCM-dissimilarity, as done above. Further, participants treated with domperidone were compared with the control group, and the treated participants were further assessed by subgroups based on their response to domperidone in terms of the low versus high serum prolactin levels.

The results demonstrate that in enhancing lesions, GLCM-contrast was lower at both week16 and week32 than baseline in the treatment group, but it was lower only at week32 in controls. GLCM-dissimilarity was lower in enhancing lesions in both treatment and control groups at weeks16 and 32 than baseline. In non-enhancing lesions, no texture measure showed significant changes over time in either group. Cross-sectionally, at week32, the treatment group revealed a lower GLCM-contrast than control group.

Regarding the 2 subgroups of domperidone treatment, the GLCM-contrast decreased at both week16 and week32 from baseline in the high prolactin group, but not in the low prolactin group. GLCM-dissimilarity decreased at both high and low prolactin groups at the follow up scans. In theory, tissue repair leads to decreased texture heterogeneity. In MS, restoring myelin sheath and clearance of myelin debris happening in the repair process can all improve the uniformity of tissue structure and its image organization [179, 180], leading to decreased GLCM contrast and dissimilarity. Therefore, our findings of significantly lower GLCM contrast and dissimilarity at week16 and week32 than baseline in the enhancing MS lesions may suggest tissue repair over time, although the role of other reparative mechanisms including resolution of inflammation and edema cannot be completely excluded [224, 225]. Further, the much stronger significance seen with gadolinium-enhancing lesions at follow-up than the non-enhancing lesions appears to be consistent with prior evidence showing that acute MS lesions have the strongest capacity to repair [6, 7]. Collective findings may indicate the potential of texture analysis to detect remyelination in acute MS lesions following treatment with a pro-reparative agent such as domperidone, deserves further investigation.

7.2 Limitations of the thesis

There are some limitations in this thesis project. First, in postmortem studies of the research, the sample size was limited, and there were different numbers of ROIs per tissue type and subject. Notwithstanding the relatively limited sample, this work offers valuable insights into MS lesion characterization. Second, there was no histology done to differentiate partial demyelination from remyelination (e.g. shadow plaques), and therefore it is not possible to test the utility of the image

analysis techniques in characterizing those types of pathology. However, evidence from both the literature [141, 153] and current thesis (e.g. Aim1) demonstrate the potential of texture analysis for identifying de- and re-myelinated lesions in MS. In addition, there was also lack of staining for inflammation, and therefore the role of its resolution in texture improvement is unclear. Nevertheless, the postmortem samples are obtained mainly from progressive MS participants, who typically contain much less inflammation than relapsing MS. Third, given the inherent differences between in vivo and ex vivo MRI, the absolute value of imaging features between them may be different, which is unavoidable in these types of studies. However, our focus of analysis on the pattern of imaging signal may have helped lessen the impact of this limitation. Furthermore, in prior studies, texture analysis has been successfully used in vivo, using clinical scanners to study lesions and NAWM in MS as well as normal white matter in control [16, 17]. Fourth, the high resolution of postmortem T2-weighted MRI used herein compared to in vivo clinical MR scans may raise a utility question of the current analyzing approach in living participants. However, my pilot experiments have shown the similarity between texture patterns derived using super-high resolution images versus relatively low, clinically equivalent resolution images. Further, various studies using this or alternative texture analysis methods have shown the promise to characterize tissue pathology using clinical MRI in MS and similar diseases [108, 141].

In the cross-sectional studies of in vivo MS participants, there were also a few limiting points. First, the scope of in vivo data analysis was limited to white matter lesions and lacked the assessment of lesions in other areas, such as grey matter lesions. Nevertheless, white matter lesions are still the prominent target area in MS assessment. Moreover, this study was focused on the RRMS subtype of MS, while assessing other types of MS might provide more insight into MS

tissue pathology, RRMS participants involve the most active de- and re-myelinated lesions. Besides, given the nature of in vivo studies, there was no direct confirmation for the two identified lesion types. Nevertheless, the implemented texture analysis measures were histology-confirmed in the former aim. Further, the sex-based analysis results showing worse outcomes in the respective lesion types seemed to be consistent with the worse disease prognosis in males than females.

Regarding the longitudinal part of the research, one limitation was the small sample size, however, despite the limited sample size, this study demonstrated significant results supporting repair, including remyelination in enhancing MS lesions. Furthermore, the recovery in texture measures over time might not be exclusively due to remyelination. As noted above, other underlying pathologies, such as the resolution of inflammation and edema, might have also played a role. Yet, the texture features used here were validated against histology in the initial aim. Moreover, texture measurements revealed to be more sensitive to tissue alteration than inflammatory responses [141].

7.3 Future work

In the future, the texture metrics originated from Aim1 can be compared with other quantitative measurements based on either conventional or advanced MRI, texture based or not. These comparative studies will help further understanding the validity and value of the developed methods here. Furthermore, the 3D GLCM, which might provide more information respecting tissue structure due to more directionality calculation, can be implemented instead of conventional 2D GLCM computation for tissue or disease phenotype classification purposes. Moreover, the approach investigated in Aim2 for lesion characterization can be investigated for its

generalizability to different datasets for assessing lesion injury and repair using clinical brain MRI, associated with both clinical trials and routine patient care. Additionally, the ability of the GLCM texture analysis method used in Aim3 can be tested for characterizing the response of participants to new therapies aimed at neuroprotection and repair, and for monitoring or predicting disease progression in MS or related diseases. Future studies can also explore the utility of applying texture analysis on advanced MR images such as MTR, diffusion imaging, and SWI scans. Further, research could also be conducted to determine the relationship between the volume and distribution of the two identified lesion types and other clinical measures such as physical disability or cognitive decline of MS patients. The link between the spatial distribution of the two detected lesion types and clinical measurements can be further investigated in specific anatomical locations in the brain, such as major tracts, including the corticospinal tract, which may help identify new surrogate markers of disease outcomes.

7.4 Conclusions and significance

In this research, I have developed novel texture analysis approaches assisted by machine learning techniques for classifying different tissue types in grey and white matter of MS brain based on clinical MRI, particularly regarding tissue injury and repair in focal lesions. I have then validated the approaches using different strategies ranging from postmortem brain samples to in vivo datasets of MS participants, and from advanced MRI measures to their texture analysis indices. Overall approaches proposed here may help open up new avenues of clinical research in MS, and the derived texture analysis measures may become new MRI biomarkers of lesion injury and repair, which would be invaluable for monitoring both disease progression and treatment response.

Finally, with further validation, the methods and measurements developed here can be translated to other neurological diseases other than MS for similar study purposes.

Acknowledgements

This research wouldn't be possible without the efforts of our following collaborators:

- The scientists, MRI and autopsy teams of the Netherland Brain Bank that we jointly published the data from the third chapter of this thesis. The author also thank the donors of the brain donation program.

- Involved clinicians, scientists, imaging and data collection teams in domperidone trial. The data was used in chapter 4 and 5 of this thesis and the manuscripts are being prepared for submission.

Funding: This research was supported in part by the Natural Science and Engineering Council of Canada (NSERC), which invests annually over $1 billion in people, discovery, and innovation, MS Society of Canada, and Alberta Innovates (YZ), as well as supported in part by the National MS Society USA [RG4916A2/1] to MI.

References:

[1] *The Multiple Sclerosis International Federation, Atlas of MS, 3rd Edition,* September 2020.

[2] J. Correale and M. F. Farez, "The role of astrocytes in multiple sclerosis progression," *Frontiers in neurology,* vol. 6, p. 180, 2015.

[3] I. Vavasour *et al.*, "Longitudinal changes in myelin water fraction in two MS patients with active disease," *Journal of the neurological sciences,* vol. 276, no. 1-2, pp. 49-53, 2009.

[4] J. R. Plemel, W.-Q. Liu, and V. W. Yong, "Remyelination therapies: a new direction and challenge in multiple sclerosis," *Nature reviews Drug discovery,* vol. 16, no. 9, pp. 617-634, 2017.

[5] E. Bernitsas *et al.*, "Multimodal MRI Response to Fingolimod in Multiple Sclerosis: A Nonrandomized, Single Arm, Observational Study," *Journal of Neuroimaging,* vol. 31, no. 2, pp. 379-387, 2021.

[6] K. Heß *et al.*, "Lesion stage-dependent causes for impaired remyelination in MS," *Acta neuropathologica,* vol. 140, no. 3, pp. 359-375, 2020.

[7] C. S. Raine and E. Wu, "Multiple sclerosis: remyelination in acute lesions," *Journal of Neuropathology & Experimental Neurology,* vol. 52, no. 3, pp. 199-204, 1993.

[8] T. Kuhlmann, S. Ludwin, A. Prat, J. Antel, W. Brück, and H. Lassmann, "An updated histological classification system for multiple sclerosis lesions," *Acta neuropathologica,* vol. 133, no. 1, pp. 13-24, 2017.

[9] D. M. Chari, "Remyelination in multiple sclerosis," *International review of neurobiology,* vol. 79, pp. 589-620, 2007.

[10] C. Lubetzki, B. Zalc, A. Williams, C. Stadelmann, and B. Stankoff, "Remyelination in multiple sclerosis: from basic science to clinical translation," *The Lancet Neurology,* vol. 19, no. 8, pp. 678-688, 2020.

[11] F. Barkhof, "Imaging of remyelination," *Multiple Sclerosis Journal,* vol. 3, no. 2, pp. 129-132, 1997.

[12] M. Filippi, P. Preziosa, and M. A. Rocca, "MRI in multiple sclerosis: what is changing?," *Current opinion in neurology,* vol. 31, no. 4, pp. 386-395, 2018.

[13] M.-E. Dounavi *et al.*, "Fluid-attenuated inversion recovery magnetic resonance imaging textural features as sensitive markers of white matter damage in midlife adults," *Brain Communications,* vol. 4, no. 3, p. fcac116, 2022.

[14] A. Kassner and R. Thornhill, "Texture analysis: a review of neurologic MR imaging applications," *American Journal of Neuroradiology,* vol. 31, no. 5, pp. 809-816, 2010.

[15] J. Zhang, L. Tong, L. Wang, and N. Li, "Texture analysis of multiple sclerosis: a comparative study," *Magnetic resonance imaging,* vol. 26, no. 8, pp. 1160-1166, 2008.

[16] C. P. Loizou, S. Petroudi, I. Seimenis, M. Pantziaris, and C. S. Pattichis, "Quantitative texture analysis of brain white matter lesions derived from T2-weighted MR images in MS patients with clinically isolated syndrome," *Journal of Neuroradiology,* vol. 42, no. 2, pp. 99-114, 2015.

[17] Y. Zhang, A. Traboulsee, Y. Zhao, L. M. Metz, and D. K. Li, "Texture analysis differentiates persistent and transient T1 black holes at acute onset in multiple sclerosis: a preliminary study," *Multiple Sclerosis Journal,* vol. 17, no. 5, pp. 532-540, 2011.

[18] N. Fozouni *et al.*, "Characterizing brain structures and remodeling after TBI based on information content, diffusion entropy," *PLoS One,* vol. 8, no. 10, p. e76343, 2013.
[19] G. Pridham, M. D. Steenwijk, J. J. Geurts, and Y. Zhang, "A discrete polar Stockwell transform for enhanced characterization of tissue structure using MRI," *Magnetic resonance in medicine,* vol. 80, no. 6, pp. 2731-2743, 2018.
[20] Y. Zhang, "MRI texture analysis in multiple sclerosis," *International Journal of Biomedical Imaging,* vol. 2012, 2012.
[21] Z. O. Hosseinpour, Olayinka; Soleymani, Mahshid; Pike G, Bruce; Zhang, Yunyan., "Characterization of multiple sclerosis lesion types with texture analysis of advanced and conventional MRI," *Proc. Intl. Soc. Mag. Reson. Med. 29 (2021)*.
[22] W. J. Huang, W. W. Chen, and X. Zhang, "Multiple sclerosis: Pathology, diagnosis and treatments," *Experimental and therapeutic medicine,* vol. 13, no. 6, pp. 3163-3166, 2017.
[23] C. Walton *et al.*, "Rising prevalence of multiple sclerosis worldwide: Insights from the Atlas of MS," *Multiple Sclerosis Journal,* vol. 26, no. 14, pp. 1816-1821, 2020.
[24] S. V. Ramagopalan, R. Dobson, U. C. Meier, and G. Giovannoni, "Multiple sclerosis: risk factors, prodromes, and potential causal pathways," *The Lancet Neurology,* vol. 9, no. 7, pp. 727-739, 2010.
[25] S. G. Waxman, "Membranes, myelin, and the pathophysiology of multiple sclerosis," *New England Journal of Medicine,* vol. 306, no. 25, pp. 1529-1533, 1982.
[26] S. J. Pittock and C. F. Lucchinetti, "The pathology of MS: new insights and potential clinical applications," *The neurologist,* vol. 13, no. 2, pp. 45-56, 2007.
[27] Y. Zhang *et al.*, "Pathological correlates of magnetic resonance imaging texture heterogeneity in multiple sclerosis," *Annals of neurology,* vol. 74, no. 1, pp. 91-99, 2013.
[28] Y. Zhang *et al.*, "Multi-scale MRI spectrum detects differences in myelin integrity between MS lesion types," *Multiple Sclerosis Journal,* vol. 22, no. 12, pp. 1569-1577, 2016.
[29] R. J. Franklin, "Regenerating CNS myelin—from mechanisms to experimental medicines," *Nature Reviews Neuroscience,* vol. 18, no. 12, pp. 753-769, 2017.
[30] G. F. Wu and E. Alvarez, "The immunopathophysiology of multiple sclerosis," *Neurologic clinics,* vol. 29, no. 2, pp. 257-278, 2011.
[31] B. F. G. Popescu, I. Pirko, and C. F. Lucchinetti, "Pathology of multiple sclerosis: where do we stand?," *CONTINUUM: Lifelong Learning in Neurology,* vol. 19, no. 4 Multiple Sclerosis, p. 901, 2013.
[32] I. Loma and R. Heyman, "Multiple sclerosis: pathogenesis and treatment," *Current neuropharmacology,* vol. 9, no. 3, pp. 409-416, 2011.
[33] J. D. Haines, M. Inglese, and P. Casaccia, "Axonal damage in multiple sclerosis," *Mount Sinai Journal of Medicine: A Journal of Translational and Personalized Medicine,* vol. 78, no. 2, pp. 231-243, 2011.
[34] A. Bitsch and W. Brück, "Differentiation of multiple sclerosis subtypes," *CNS drugs,* vol. 16, no. 6, pp. 405-418, 2002.
[35] S. Klineova and F. D. Lublin, "Clinical course of multiple sclerosis," *Cold Spring Harbor perspectives in medicine,* vol. 8, no. 9, p. a028928, 2018.
[36] U. W. Kaunzner and S. A. Gauthier, "MRI in the assessment and monitoring of multiple sclerosis: an update on best practice," *Therapeutic advances in neurological disorders,* vol. 10, no. 6, pp. 247-261, 2017.

[37] F. Barkhof *et al.*, "Remyelinated lesions in multiple sclerosis: magnetic resonance image appearance," *Archives of neurology,* vol. 60, no. 8, pp. 1073-1081, 2003.
[38] A. Rovira, C. Auger, and J. Alonso, "Magnetic resonance monitoring of lesion evolution in multiple sclerosis," *Therapeutic advances in neurological disorders,* vol. 6, no. 5, pp. 298-310, 2013.
[39] D. W. McRobbie, E. A. Moore, M. J. Graves, and M. R. Prince, *MRI from Picture to Proton*. Cambridge university press, 2017.
[40] M. A. Sahraian and A. Eshaghi, "Role of MRI in diagnosis and treatment of multiple sclerosis," *Clinical neurology and neurosurgery,* vol. 112, no. 7, pp. 609-615, 2010.
[41] M. Filippi *et al.*, "Assessment of lesions on magnetic resonance imaging in multiple sclerosis: practical guidelines," *Brain,* vol. 142, no. 7, pp. 1858-1875, 2019.
[42] M. Sahraian, E. W. Radue, S. Haller, and L. Kappos, "Black holes in multiple sclerosis: definition, evolution, and clinical correlations," *Acta Neurologica Scandinavica,* vol. 122, no. 1, pp. 1-8, 2010.
[43] D. Warakaulle and P. Anslow, "Differential diagnosis of intracranial lesions with high signal on T1 or low signal on T2-weighted MRI," *Clinical radiology,* vol. 58, no. 12, pp. 922-933, 2003.
[44] M. Calabrese, M. Filippi, and P. Gallo, "Cortical lesions in multiple sclerosis," *Nature Reviews Neurology,* vol. 6, no. 8, pp. 438-444, 2010.
[45] S. Mastrogiacomo, W. Dou, J. A. Jansen, and X. F. Walboomers, "Magnetic resonance imaging of hard tissues and hard tissue engineered bio-substitutes," *Molecular imaging and biology,* vol. 21, no. 6, pp. 1003-1019, 2019.
[46] M. Saranathan, P. W. Worters, D. W. Rettmann, B. Winegar, and J. Becker, "Physics for clinicians: Fluid-attenuated inversion recovery (FLAIR) and double inversion recovery (DIR) Imaging," *Journal of Magnetic Resonance Imaging,* vol. 46, no. 6, pp. 1590-1600, 2017.
[47] C. Egger *et al.*, "MRI FLAIR lesion segmentation in multiple sclerosis: Does automated segmentation hold up with manual annotation?," *NeuroImage: Clinical,* vol. 13, pp. 264-270, 2017.
[48] R. Khayati, M. Vafadust, F. Towhidkhah, and M. Nabavi, "Fully automatic segmentation of multiple sclerosis lesions in brain MR FLAIR images using adaptive mixtures method and Markov random field model," *Computers in biology and medicine,* vol. 38, no. 3, pp. 379-390, 2008.
[49] M. Inglese and M. Petracca, "MRI in multiple sclerosis: clinical and research update," *Current opinion in neurology,* vol. 31, no. 3, pp. 249-255, 2018.
[50] M. Absinta *et al.*, "Persistent 7-tesla phase rim predicts poor outcome in new multiple sclerosis patient lesions," *The Journal of clinical investigation,* vol. 126, no. 7, pp. 2597-2609, 2016.
[51] M. Filippi and F. Agosta, "Magnetization transfer MRI in multiple sclerosis," *Journal of Neuroimaging,* vol. 17, pp. 22S-26S, 2007.
[52] C. Laule and G. W. Moore, "Myelin water imaging to detect demyelination and remyelination and its validation in pathology," *Brain Pathology,* vol. 28, no. 5, pp. 750-764, 2018.

[53] J. Lee *et al.*, "The contribution of myelin to magnetic susceptibility-weighted contrasts in high-field MRI of the brain," *Neuroimage,* vol. 59, no. 4, pp. 3967-3975, 2012.
[54] D. Le Bihan and H. Johansen-Berg, "Diffusion MRI at 25: exploring brain tissue structure and function," *Neuroimage,* vol. 61, no. 2, pp. 324-341, 2012.
[55] P. J. Basser and E. Özarslan, "Introduction to diffusion MR," *Diffusion MRI,* pp. 2-10, 2009.
[56] P. Hagmann, L. Jonasson, P. Maeder, J.-P. Thiran, V. J. Wedeen, and R. Meuli, "Understanding diffusion MR imaging techniques: from scalar diffusion-weighted imaging to diffusion tensor imaging and beyond," *Radiographics,* vol. 26, no. suppl_1, pp. S205-S223, 2006.
[57] J. Webster and M. Descoteaux, "High Angular Resolution Diffusion Imaging (HARDI)," *Wiley Encyclopedia of Electrical and Electronics Engineering. https://doi. org/10.1002/047134608x. w8258,* 2015.
[58] E. Sbardella, F. Tona, N. Petsas, and P. Pantano, "DTI measurements in multiple sclerosis: evaluation of brain damage and clinical implications," *Multiple sclerosis international,* vol. 2013, 2013.
[59] A. L. Alexander, J. E. Lee, M. Lazar, and A. S. Field, "Diffusion tensor imaging of the brain," *Neurotherapeutics,* vol. 4, no. 3, pp. 316-329, 2007.
[60] S. M. Mustafi *et al.*, "Detecting white matter alterations in multiple sclerosis using advanced diffusion magnetic resonance imaging," *Neural regeneration research,* vol. 14, no. 1, p. 114, 2019.
[61] S. Mori and J.-D. Tournier, *Introduction to diffusion tensor imaging: And higher order models*. Academic Press, 2013.
[62] J. I. Berman, M. R. Lanza, L. Blaskey, J. C. Edgar, and T. P. Roberts, "High angular resolution diffusion imaging probabilistic tractography of the auditory radiation," *American Journal of Neuroradiology,* vol. 34, no. 8, pp. 1573-1578, 2013.
[63] D. S. Tuch, "Q-ball imaging," *Magnetic Resonance in Medicine: An Official Journal of the International Society for Magnetic Resonance in Medicine,* vol. 52, no. 6, pp. 1358-1372, 2004.
[64] S. De Santis *et al.*, "Whole brain in vivo axonal diameter mapping in multiple sclerosis," in *2019 41st Annual International Conference of the IEEE Engineering in Medicine and Biology Society (EMBC)*, 2019, pp. 204-207: IEEE.
[65] J. Cohen-Adad *et al.*, "Demyelination and degeneration in the injured human spinal cord detected with diffusion and magnetization transfer MRI," *Neuroimage,* vol. 55, no. 3, pp. 1024-1033, 2011.
[66] J. Scholz, V. Tomassini, and H. Johansen-Berg, "Individual differences in white matter microstructure in the healthy brain," in *Diffusion MRI*: Elsevier, 2014, pp. 301-316.
[67] M. Kim and M. Cercignani, "Magnetization transfer," in *Quantitative MRI of the Spinal Cord*: Elsevier, 2014, pp. 164-180.
[68] J. T. Chen, D. L. Collins, H. L. Atkins, M. S. Freedman, D. L. Arnold, and C. M. B. S. Group, "Magnetization transfer ratio evolution with demyelination and remyelination in multiple sclerosis lesions," *Annals of neurology,* vol. 63, no. 2, pp. 254-262, 2008.
[69] A. M. Weber, C. Torres, and A. Rauscher, "Imaging the role of myelin in concussion," *Neuroimaging Clinics,* vol. 28, no. 1, pp. 83-90, 2018.

[70] I. M. Vavasour, C. Laule, D. K. Li, A. L. Traboulsee, and A. L. MacKay, "Is the magnetization transfer ratio a marker for myelin in multiple sclerosis?," *Journal of Magnetic Resonance Imaging,* vol. 33, no. 3, pp. 710-718, 2011.
[71] P. Sprawls, *Magnetic resonance imaging: principles, methods, and techniques*. Medical Physics Publishing Madison, 2000.
[72] W. S. Vargas *et al.*, "Measuring longitudinal myelin water fraction in new multiple sclerosis lesions," *NeuroImage: Clinical,* vol. 9, pp. 369-375, 2015.
[73] S. Kolind *et al.*, "Myelin water imaging reflects clinical variability in multiple sclerosis," *Neuroimage,* vol. 60, no. 1, pp. 263-270, 2012.
[74] C. Laule *et al.*, "Water content and myelin water fraction in multiple sclerosis," *Journal of neurology,* vol. 251, no. 3, pp. 284-293, 2004.
[75] V. Sehgal *et al.*, "Clinical applications of neuroimaging with susceptibility-weighted imaging," *Journal of Magnetic Resonance Imaging: An Official Journal of the International Society for Magnetic Resonance in Medicine,* vol. 22, no. 4, pp. 439-450, 2005.
[76] C. Liu, W. Li, K. A. Tong, K. W. Yeom, and S. Kuzminski, "Susceptibility-weighted imaging and quantitative susceptibility mapping in the brain," *Journal of magnetic resonance imaging,* vol. 42, no. 1, pp. 23-41, 2015.
[77] Y. Wang *et al.*, "Clinical quantitative susceptibility mapping (QSM): Biometal imaging and its emerging roles in patient care," *Journal of Magnetic Resonance Imaging,* vol. 46, no. 4, pp. 951-971, 2017.
[78] U. Vovk, F. Pernus, and B. Likar, "A review of methods for correction of intensity inhomogeneity in MRI," *IEEE transactions on medical imaging,* vol. 26, no. 3, pp. 405-421, 2007.
[79] S. Song, Y. Zheng, and Y. He, "A review of methods for bias correction in medical images," *Biomedical Engineering Review,* vol. 1, no. 1, 2017.
[80] N. J. Tustison *et al.*, "N4ITK: improved N3 bias correction," *IEEE transactions on medical imaging,* vol. 29, no. 6, pp. 1310-1320, 2010.
[81] S. M. Smith, "Fast robust automated brain extraction," *Human brain mapping,* vol. 17, no. 3, pp. 143-155, 2002.
[82] Y. Wang *et al.*, "Knowledge-guided robust MRI brain extraction for diverse large-scale neuroimaging studies on humans and non-human primates," *PloS one,* vol. 9, no. 1, p. e77810, 2014.
[83] B. Zitova and J. Flusser, "Image registration methods: a survey," *Image and vision computing,* vol. 21, no. 11, pp. 977-1000, 2003.
[84] M. Wang and P. Li, "A review of deformation models in medical image registration," *Journal of Medical and Biological Engineering,* vol. 39, no. 1, pp. 1-17, 2019.
[85] Y. Fu, Y. Lei, T. Wang, W. J. Curran, T. Liu, and X. Yang, "Deep learning in medical image registration: a review," *Physics in Medicine & Biology,* vol. 65, no. 20, p. 20TR01, 2020.
[86] S. Gu and R. Timofte, "A brief review of image denoising algorithms and beyond," *Inpainting and Denoising Challenges,* pp. 1-21, 2019.
[87] A. Sharma and V. Chaurasia, "A review on magnetic resonance images denoising techniques," in *Machine Intelligence and Signal Analysis*: Springer, 2019, pp. 707-715.
[88] L. Kanwal, "A Review on MRI Denoising Methods," *LGUJLS,* vol. 3, no. 3, pp. 132-139, 2019.

[89] M. T. Mahmood, Y.-H. Chu, and Y.-K. Choi, "Rician noise reduction in magnetic resonance images using adaptive non-local mean and guided image filtering," *Optical Review,* vol. 23, no. 3, pp. 460-469, 2016.
[90] A. A. Samsonov and C. R. Johnson, "Noise-adaptive nonlinear diffusion filtering of MR images with spatially varying noise levels," *Magnetic Resonance in Medicine: An Official Journal of the International Society for Magnetic Resonance in Medicine,* vol. 52, no. 4, pp. 798-806, 2004.
[91] J. S. Lim, "Two-dimensional signal and image processing," *Englewood Cliffs,* 1990.
[92] I. S. Isa, S. N. Sulaiman, M. Mustapha, and S. Darus, "Evaluating denoising performances of fundamental filters for t2-weighted MRI images," *Procedia Computer Science,* vol. 60, pp. 760-768, 2015.
[93] J. V. Manjón, J. Carbonell-Caballero, J. J. Lull, G. García-Martí, L. Martí-Bonmatí, and M. Robles, "MRI denoising using non-local means," *Medical image analysis,* vol. 12, no. 4, pp. 514-523, 2008.
[94] Y.-C. Heo, K. Kim, and Y. Lee, "Image Denoising Using Non-Local Means (NLM) Approach in Magnetic Resonance (MR) Imaging: A Systematic Review," *Applied Sciences,* vol. 10, no. 20, p. 7028, 2020.
[95] G. Collewet, M. Strzelecki, and F. Mariette, "Influence of MRI acquisition protocols and image intensity normalization methods on texture classification," *Magnetic resonance imaging,* vol. 22, no. 1, pp. 81-91, 2004.
[96] C. P. Loizou, M. Pantziaris, I. Seimenis, and C. S. Pattichis, "Brain MR image normalization in texture analysis of multiple sclerosis," in *2009 9th International Conference on Information Technology and Applications in Biomedicine*, 2009, pp. 1-5: IEEE.
[97] A. Carré *et al.*, "Standardization of brain MR images across machines and protocols: bridging the gap for MRI-based radiomics," *Scientific reports,* vol. 10, no. 1, pp. 1-15, 2020.
[98] J. Haneda *et al.*, "A Comparison of Techniques for Correcting Eddy-current and Motion-induced Distortions in Diffusion-weighted Echo-planar Images," *Magnetic Resonance in Medical Sciences,* vol. 18, no. 4, p. 272, 2019.
[99] S. M. Maniega, M. E. Bastin, and P. A. Armitage, "A quantitative comparison of two methods to correct eddy current-induced distortions in DT-MRI," *Magnetic resonance imaging,* vol. 25, no. 3, pp. 341-349, 2007.
[100] M. O. Irfanoglu, J. Sarlls, A. Nayak, and C. Pierpaoli, "Evaluating corrections for Eddy-currents and other EPI distortions in diffusion MRI: methodology and a dataset for benchmarking," *Magnetic resonance in medicine,* vol. 81, no. 4, pp. 2774-2787, 2019.
[101] V. Rajagopalan *et al.*, "A basic introduction to diffusion tensor imaging mathematics and image processing steps," *Brain Disord Ther,* vol. 6, no. 229, p. 2, 2017.
[102] P. Smitha, L. Shaji, and M. Mini, "A review of medical image classification techniques," in *International conference on VLSI, Communication & Intrumrnataiom*, 2011, pp. 34-38.
[103] D. Mitrea, M. Socaciu, R. Badea, and A. Golea, "Texture based characterization and automatic diagnosis of the abdominal tumors from ultrasound images using third order GLCM features," in *2011 4th International Congress on Image and Signal Processing*, 2011, vol. 3, pp. 1558-1562: IEEE.
[104] M. M. Fathima, D. Manimegalai, and S. Thaiyalnayaki, "Automatic detection of tumor subtype in mammograms based On GLCM and DWT features using SVM," in *2013*

International Conference on Information Communication and Embedded Systems (ICICES), 2013, pp. 809-813: IEEE.

[105] G. Srinivasan and G. Shobha, "Statistical texture analysis," in *Proceedings of world academy of science, engineering and technology*, 2008, vol. 36, no. December, pp. 1264-1269.

[106] R. M. Haralick, K. Shanmugam, and I. H. Dinstein, "Textural features for image classification," *IEEE Transactions on systems, man, and cybernetics,* no. 6, pp. 610-621, 1973.

[107] I. MicroImages, "Gray Level Co-occurrence Matrix Filters " 2014.

[108] V. Durgamahanthi, J. A. Christaline, and A. S. Edward, "GLCM and GLRLM based texture analysis: application to brain cancer diagnosis using histopathology images," in *Intelligent computing and applications*: Springer, 2021, pp. 691-706.

[109] A. Nunes *et al.*, "Textural information from the retinal nerve fibre layer in multiple sclerosis," in *2019 IEEE 6th Portuguese Meeting on Bioengineering (ENBENG)*, 2019, pp. 1-4: IEEE.

[110] S. Jain, N. Rajpal, and J. Yadav, "Multiple Sclerosis Identification Based on Ensemble Machine Learning Technique," *Available at SSRN 3734806,* 2020.

[111] P. Mohanaiah, P. Sathyanarayana, and L. GuruKumar, "Image texture feature extraction using GLCM approach," *International journal of scientific and research publications,* vol. 3, no. 5, pp. 1-5, 2013.

[112] M. Stankovic *et al.*, "Quantification of structural changes in acute inflammation by fractal dimension, angular second moment and correlation," *Journal of microscopy,* vol. 261, no. 3, pp. 277-284, 2016.

[113] X. Ou, W. Pan, and P. Xiao, "In vivo skin capacitive imaging analysis by using grey level co-occurrence matrix (GLCM)," *International journal of pharmaceutics,* vol. 460, no. 1-2, pp. 28-32, 2014.

[114] N. Michoux, A. Guillet, D. Rommel, G. Mazzamuto, C. Sindic, and T. Duprez, "Texture analysis of T2-weighted MR images to assess acute inflammation in brain MS lesions," *PLoS One,* vol. 10, no. 12, p. e0145497, 2015.

[115] Y. Wu, Y. Zhou, G. Saveriades, S. Agaian, J. P. Noonan, and P. Natarajan, "Local Shannon entropy measure with statistical tests for image randomness," *Information Sciences,* vol. 222, pp. 323-342, 2013.

[116] S. Waugh *et al.*, "Magnetic resonance imaging texture analysis classification of primary breast cancer," *European radiology,* vol. 26, no. 2, pp. 322-330, 2016.

[117] L. Moraru *et al.*, "Texture spectrum coupled with entropy and homogeneity image features for myocardium muscle characterization," *Current Bioinformatics,* vol. 14, no. 4, pp. 295-304, 2019.

[118] M. Maleki, M. Teshnehlab, and M. Nabavi, "Diagnosis of multiple sclerosis (MS) using convolutional neural network (CNN) from MRIs," *Global Journal of Medicinal Plant Research,* vol. 1, no. 1, pp. 50-54, 2012.

[119] P. G. Freire, M. H. Idagawa, E. M. L. de Oliveira, N. Abdala, H. Carrete, and R. J. Ferrari, "Classification of Active Multiple Sclerosis Lesions in MRI Without the Aid of Gadolinium-Based Contrast Using Textural and Enhanced Features from FLAIR Images," in

International Conference on Computational Science and Its Applications, 2020, pp. 60-74: Springer.

[120] P. Chaitra and D. R. S. Kumar, "A review of multi-class classification algorithms," *Int. J. Pure Appl. Math,* vol. 118, no. 14, pp. 17-26, 2018.

[121] I. El Naqa and M. J. Murphy, "What is machine learning?," in *machine learning in radiation oncology*: Springer, 2015, pp. 3-11.

[122] B. Mahesh, "Machine Learning Algorithms-A Review," *International Journal of Science and Research (IJSR).[Internet],* vol. 9, pp. 381-386, 2020.

[123] I. Muhammad and Z. Yan, "SUPERVISED MACHINE LEARNING APPROACHES: A SURVEY," *ICTACT Journal on Soft Computing,* vol. 5, no. 3, 2015.

[124] H. H. Patel and P. Prajapati, "Study and analysis of decision tree based classification algorithms," *International Journal of Computer Sciences and Engineering,* vol. 6, no. 10, pp. 74-78, 2018.

[125] T. Hastie, R. Tibshirani, and J. Friedman, "The elements of statistical learnin," *Cited on,* p. 33, 2009.

[126] A. L. Boulesteix, S. Janitza, J. Kruppa, and I. R. König, "Overview of random forest methodology and practical guidance with emphasis on computational biology and bioinformatics," *Wiley Interdisciplinary Reviews: Data Mining and Knowledge Discovery,* vol. 2, no. 6, pp. 493-507, 2012.

[127] L. Breiman, "Random forests," *Machine learning,* vol. 45, no. 1, pp. 5-32, 2001.

[128] V. Svetnik, A. Liaw, C. Tong, J. C. Culberson, R. P. Sheridan, and B. P. Feuston, "Random forest: a classification and regression tool for compound classification and QSAR modeling," *Journal of chemical information and computer sciences,* vol. 43, no. 6, pp. 1947-1958, 2003.

[129] T. B. Trafalis and R. C. Gilbert, "Robust classification and regression using support vector machines," *European Journal of Operational Research,* vol. 173, no. 3, pp. 893-909, 2006.

[130] S. B. Kotsiantis, I. D. Zaharakis, and P. E. Pintelas, "Machine learning: a review of classification and combining techniques," *Artificial Intelligence Review,* vol. 26, no. 3, pp. 159-190, 2006.

[131] J. A. Suykens, "Nonlinear modelling and support vector machines," in *IMTC 2001. proceedings of the 18th IEEE instrumentation and measurement technology conference. Rediscovering measurement in the age of informatics (Cat. No. 01CH 37188)*, 2001, vol. 1, pp. 287-294: IEEE.

[132] A. Roohi, K. Faust, U. Djuric, and P. Diamandis, "Unsupervised machine learning in pathology: the next frontier," *Surgical Pathology Clinics,* vol. 13, no. 2, pp. 349-358, 2020.

[133] E. Martínez-Heras *et al.*, "Characterization of multiple sclerosis lesions with distinct clinical correlates through quantitative diffusion MRI," *NeuroImage: Clinical,* vol. 28, p. 102411, 2020.

[134] S. Shukla and S. Naganna, "A review on K-means data clustering approach," *International Journal of Information and Computation Technology,* vol. 4, no. 17, pp. 1847-1860, 2014.

[135] M. Ringnér, "What is principal component analysis?," *Nature biotechnology,* vol. 26, no. 3, pp. 303-304, 2008.

[136] B. M. S. Hasan and A. M. Abdulazeez, "A review of principal component analysis algorithm for dimensionality reduction," *Journal of Soft Computing and Data Mining,* vol. 2, no. 1, pp. 20-30, 2021.
[137] D. S. Reich *et al.*, "Sample-size calculations for short-term proof-of-concept studies of tissue protection and repair in multiple sclerosis lesions via conventional clinical imaging," *Multiple Sclerosis Journal,* vol. 21, no. 13, pp. 1693-1704, 2015.
[138] O. Oladosu, W.-Q. Liu, B. G. Pike, M. Koch, L. M. Metz, and Y. Zhang, "Advanced Analysis of Diffusion Tensor Imaging Along With Machine Learning Provides New Sensitive Measures of Tissue Pathology and Intra-Lesion Activity in Multiple Sclerosis," *Frontiers in neuroscience,* vol. 15, p. 540, 2021.
[139] J. Chen, D. L. Collins, M. Freedman, H. Atkins, D. L. Arnold, and C. M. B. S. Group, "Local magnetization transfer ratio signal inhomogeneity is related to subsequent change in MTR in lesions and normal-appearing white-matter of multiple sclerosis patients," *Neuroimage,* vol. 25, no. 4, pp. 1272-1278, 2005.
[140] S. M. Hurtado Rúa *et al.*, "Lesion features on magnetic resonance imaging discriminate multiple sclerosis patients," *European Journal of Neurology,* vol. 29, no. 1, pp. 237-246, 2022.
[141] Y. Zhang, H. Zhu, J. R. Mitchell, F. Costello, and L. M. Metz, "T2 MRI texture analysis is a sensitive measure of tissue injury and recovery resulting from acute inflammatory lesions in multiple sclerosis," *Neuroimage,* vol. 47, no. 1, pp. 107-111, 2009.
[142] R. Schlaeger *et al.*, "Prediction of long-term disability in multiple sclerosis," *Multiple Sclerosis Journal,* vol. 18, no. 1, pp. 31-38, 2012.
[143] B. İ. Tiftikçioğlu, "Multiple Sclerosis Functional Composite (MSFC): Scoring Instructions," *Archives of Neuropsychiatry,* vol. 55, no. Suppl 1, p. S46, 2018.
[144] G. Bonnier *et al.*, "Advanced MRI unravels the nature of tissue alterations in early multiple sclerosis," *Annals of clinical and translational neurology,* vol. 1, no. 6, pp. 423-432, 2014.
[145] B. Aubert-Broche *et al.*, "Regional brain atrophy in children with multiple sclerosis," *Neuroimage,* vol. 58, no. 2, pp. 409-415, 2011.
[146] Z. Hosseinpour *et al.*, "Texture analysis in brain T2 and diffusion MRI differentiates histology-verified grey and white matter pathology types in multiple sclerosis," *Journal of Neuroscience Methods,* p. 109671, 2022.
[147] T. M. S. I. Federation, "Atlas of MS, 3rd Edition. September," 2020.
[148] B. Hemmer, S. Nessler, D. Zhou, B. Kieseier, and H.-P. Hartung, "Immunopathogenesis and immunotherapy of multiple sclerosis," *Nature Clinical Practice Neurology,* vol. 2, no. 4, pp. 201-211, 2006.
[149] H. Lassmann, "Multiple sclerosis pathology," *Cold Spring Harbor perspectives in medicine,* vol. 8, no. 3, p. a028936, 2018.
[150] R. Cortese, S. Collorone, O. Ciccarelli, and A. T. Toosy, "Advances in brain imaging in multiple sclerosis," *Therapeutic advances in neurological disorders,* vol. 12, p. 1756286419859722, 2019.
[151] P. Friedrich *et al.*, "The relationship between axon density, myelination, and fractional anisotropy in the human Corpus callosum," *Cerebral Cortex,* vol. 30, no. 4, pp. 2042-2056, 2020.

[152] R. T. Larue, G. Defraene, D. De Ruysscher, P. Lambin, and W. Van Elmpt, "Quantitative radiomics studies for tissue characterization: a review of technology and methodological procedures," *The British journal of radiology,* vol. 90, no. 1070, p. 20160665, 2017.
[153] O. Yu *et al.*, "Remyelination assessment by MRI texture analysis in a cuprizone mouse model," *Magnetic resonance imaging,* vol. 22, no. 8, pp. 1139-1144, 2004.
[154] L. E. Jonkman, R. Klaver, L. Fleysher, M. Inglese, and J. J. Geurts, "The substrate of increased cortical FA in MS: A 7T post-mortem MRI and histopathology study," *Multiple Sclerosis Journal,* vol. 22, no. 14, pp. 1804-1811, 2016.
[155] L. E. Jonkman and J. J. Geurts, "Postmortem magnetic resonance imaging," in *Handbook of Clinical Neurology*, vol. 150: Elsevier, 2018, pp. 335-354.
[156] I. D. Kilsdonk *et al.*, "Increased cortical grey matter lesion detection in multiple sclerosis with 7 T MRI: a post-mortem verification study," *Brain,* vol. 139, no. 5, pp. 1472-1481, 2016.
[157] L. E. Jonkman, R. Klaver, L. Fleysher, M. Inglese, and J. J. Geurts, "Ultra-high-field MRI visualization of cortical multiple sclerosis lesions with T2 and T2*: a postmortem MRI and histopathology study," *American Journal of Neuroradiology,* vol. 36, no. 11, pp. 2062-2067, 2015.
[158] E. M. M. Strijbis, E. J. Kooi, P. van der Valk, and J. J. G. Geurts, "Cortical Remyelination Is Heterogeneous in Multiple Sclerosis," (in eng), *J Neuropathol Exp Neurol,* vol. 76, no. 5, pp. 390-401, May 1 2017.
[159] L. E. Jonkman *et al.*, "Ultra-high field MTR and qR2* differentiates subpial cortical lesions from normal-appearing gray matter in multiple sclerosis," *Multiple Sclerosis Journal,* vol. 22, no. 10, pp. 1306-1314, 2016.
[160] B. B. Avants, N. Tustison, and G. Song, "Advanced normalization tools (ANTS)," *Insight j,* vol. 2, no. 365, pp. 1-35, 2009.
[161] M. Descoteaux, N. Wiest-Daesslé, S. Prima, C. Barillot, and R. Deriche, "Impact of Rician adapted non-local means filtering on HARDI," in *International Conference on Medical Image Computing and Computer-Assisted Intervention*, 2008, pp. 122-130: Springer.
[162] E. Garyfallidis *et al.*, "Dipy, a library for the analysis of diffusion MRI data," *Frontiers in neuroinformatics,* vol. 8, p. 8, 2014.
[163] M. Descoteaux, E. Angelino, S. Fitzgibbons, and R. Deriche, "Regularized, fast, and robust analytical Q-ball imaging," *Magnetic Resonance in Medicine: An Official Journal of the International Society for Magnetic Resonance in Medicine,* vol. 58, no. 3, pp. 497-510, 2007.
[164] J. L. S. Stéfan van der Walt, Juan Nunez-Iglesias, et al., "scikit-image: Image processing in Python," *PeerJ 2:e453* 2014.
[165] A. Humeau-Heurtier, "Texture feature extraction methods: A survey," *IEEE Access,* vol. 7, pp. 8975-9000, 2019.
[166] R. W. Conners and C. A. Harlow, "A theoretical comparison of texture algorithms," *IEEE transactions on pattern analysis and machine intelligence,* no. 3, pp. 204-222, 1980.
[167] A. J. Viera and J. M. Garrett, "Understanding interobserver agreement: the kappa statistic," *Fam med,* vol. 37, no. 5, pp. 360-363, 2005.

[168] A. Anand, G. Pugalenthi, G. B. Fogel, and P. Suganthan, "An approach for classification of highly imbalanced data using weighting and undersampling," *Amino acids,* vol. 39, no. 5, pp. 1385-1391, 2010.
[169] "https://www.analyticsvidhya.com/blog/2020/10/improve-class-imbalance-class-weights/."
[170] Q. Chen, Z. Meng, X. Liu, Q. Jin, and R. Su, "Decision variants for the automatic determination of optimal feature subset in RF-RFE," *Genes,* vol. 9, no. 6, p. 301, 2018.
[171] F. Degenhardt, S. Seifert, and S. Szymczak, "Evaluation of variable selection methods for random forests and omics data sets," *Briefings in bioinformatics,* vol. 20, no. 2, pp. 492-503, 2019.
[172] R. C. Team, "R: A language and environment for statistical computing. R Foundation for Statistical Computing,," 2020.
[173] Y. Zhang *et al.*, "Multi-scale MRI spectrum detects differences in myelin integrity between MS lesion types," *Multiple Sclerosis Journal,* vol. 22, no. 12, pp. 1569-1577, 2016.
[174] G. Moore *et al.*, "Dirty-appearing white matter in multiple sclerosis," *Journal of neurology,* vol. 255, no. 11, p. 1802, 2008.
[175] A. Tripathi, N. Bhoj, M. Khari, and B. Pandey, "Feature Selection and Scaling for Random Forest Powered Malware Detection System," 2021.
[176] M. Filippi, P. Preziosa, and M. A. Rocca, "Microstructural MR imaging techniques in multiple sclerosis," *Neuroimaging Clinics,* vol. 27, no. 2, pp. 313-333, 2017.
[177] M. Zhu *et al.*, "Class weights random forest algorithm for processing class imbalanced medical data," *IEEE Access,* vol. 6, pp. 4641-4652, 2018.
[178] B. F. G. Popescu and C. F. Lucchinetti, "Meningeal and cortical grey matter pathology in multiple sclerosis," *BMC neurology,* vol. 12, no. 1, p. 11, 2012.
[179] M. Podbielska, N. L. Banik, E. Kurowska, and E. L. Hogan, "Myelin recovery in multiple sclerosis: the challenge of remyelination," *Brain sciences,* vol. 3, no. 3, pp. 1282-1324, 2013.
[180] R. J. Franklin and M. R. Kotter, "The biology of CNS remyelination," *Journal of neurology,* vol. 255, no. 1, pp. 19-25, 2008.
[181] A. Chang *et al.*, "Cortical remyelination: a new target for repair therapies in multiple sclerosis," *Annals of neurology,* vol. 72, no. 6, pp. 918-926, 2012.
[182] S. De Santis *et al.*, "Evidence of early microstructural white matter abnormalities in multiple sclerosis from multi-shell diffusion MRI," *NeuroImage: Clinical,* vol. 22, p. 101699, 2019.
[183] M. Absinta *et al.*, "Association of chronic active multiple sclerosis lesions with disability in vivo," *JAMA neurology,* vol. 76, no. 12, pp. 1474-1483, 2019.
[184] E. S. Beck *et al.*, "Cortical lesion hotspots and association of subpial lesions with disability in multiple sclerosis," *Multiple Sclerosis Journal,* p. 13524585211069167, 2022.
[185] C. Lucchinetti, W. Brück, J. Parisi, B. Scheithauer, M. Rodriguez, and H. Lassmann, "Heterogeneity of multiple sclerosis lesions: implications for the pathogenesis of demyelination," *Annals of Neurology: Official Journal of the American Neurological Association and the Child Neurology Society,* vol. 47, no. 6, pp. 707-717, 2000.
[186] T. D. Faizy *et al.*, "Heterogeneity of multiple sclerosis lesions in multislice myelin water imaging," *PloS one,* vol. 11, no. 3, p. e0151496, 2016.

[187] I. Lipp *et al.*, "Comparing MRI metrics to quantify white matter microstructural damage in multiple sclerosis," *Human brain mapping,* vol. 40, no. 10, pp. 2917-2932, 2019.
[188] A. M. Klauser *et al.*, "Metabolites predict lesion formation and severity in relapsing-remitting multiple sclerosis," *Multiple Sclerosis Journal,* vol. 24, no. 4, pp. 491-500, 2018.
[189] B. Xiang, J. Wen, A. H. Cross, and D. A. Yablonskiy, "Single scan quantitative gradient recalled echo MRI for evaluation of tissue damage in lesions and normal appearing gray and white matter in multiple sclerosis," *Journal of Magnetic Resonance Imaging,* vol. 49, no. 2, pp. 487-498, 2019.
[190] F. Bagnato *et al.*, "Evolution of T1 black holes in patients with multiple sclerosis imaged monthly for 4 years," *Brain,* vol. 126, no. 8, pp. 1782-1789, 2003.
[191] Schmidt et al., 2012.
[192] A. H. Herlihy *et al.*, "Reduction of CSF and blood flow artifacts on FLAIR images of the brain with k-space reordered by inversion time at each slice position (KRISP)," *American journal of neuroradiology,* vol. 22, no. 5, pp. 896-904, 2001.
[193] U. Sara, M. Akter, and M. S. Uddin, "Image quality assessment through FSIM, SSIM, MSE and PSNR—a comparative study," *Journal of Computer and Communications,* vol. 7, no. 3, pp. 8-18, 2019.
[194] A. Gebejes and R. Huertas, "Texture characterization based on grey-level co-occurrence matrix," *Databases,* vol. 9, no. 10, 2013.
[195] D. A. Clausi, "An analysis of co-occurrence texture statistics as a function of grey level quantization," *Canadian Journal of remote sensing,* vol. 28, no. 1, pp. 45-62, 2002.
[196] G. Grabner, A. L. Janke, M. M. Budge, D. Smith, J. Pruessner, and D. L. Collins, "Symmetric atlasing and model based segmentation: an application to the hippocampus in older adults," in *International Conference on Medical Image Computing and Computer-Assisted Intervention*, 2006, pp. 58-66: Springer.
[197] J. Correale and M. C. Ysrraelit, "Multiple Sclerosis and Aging: The Dynamics of Demyelination and Remyelination," *ASN neuro,* vol. 14, p. 17590914221118502, 2022.
[198] N. Cunniffe and A. Coles, "Promoting remyelination in multiple sclerosis," *Journal of neurology,* vol. 268, no. 1, pp. 30-44, 2021.
[199] M. Macchi *et al.*, "Mature oligodendrocytes bordering lesions limit demyelination and favor myelin repair via heparan sulfate production," *elife,* vol. 9, p. e51735, 2020.
[200] R. Patani, M. Balaratnam, A. Vora, and R. Reynolds, "Remyelination can be extensive in multiple sclerosis despite a long disease course," *Neuropathology and applied neurobiology,* vol. 33, no. 3, pp. 277-287, 2007.
[201] L. Filli *et al.*, "Spatiotemporal distribution of white matter lesions in relapsing–remitting and secondary progressive multiple sclerosis," *Multiple Sclerosis Journal,* vol. 18, no. 11, pp. 1577-1584, 2012.
[202] A. Giorgio *et al.*, "Mapping the Progressive Treatment-Related Reduction of Active MRI Lesions in Multiple Sclerosis," *Frontiers in neurology,* p. 1466, 2020.
[203] P. Patrikios *et al.*, "Remyelination is extensive in a subset of multiple sclerosis patients," *Brain,* vol. 129, no. 12, pp. 3165-3172, 2006.
[204] T. Goldschmidt, J. Antel, F. König, W. Brück, and T. Kuhlmann, "Remyelination capacity of the MS brain decreases with disease chronicity," *Neurology,* vol. 72, no. 22, pp. 1914-1921, 2009.

[205] M. Habek, "Evaluation of brainstem involvement in multiple sclerosis," *Expert review of neurotherapeutics,* vol. 13, no. 3, pp. 299-311, 2013.
[206] S. K. Ludwin, "The pathogenesis of multiple sclerosis: relating human pathology to experimental studies," *Journal of Neuropathology & Experimental Neurology,* vol. 65, no. 4, pp. 305-318, 2006.
[207] M. Elzayady, N. L. Debees, M. Khalil, and M. M. Dawoud, "Cerebellum and brain stem volume loss in relapsing remission multiple sclerosis by MRI volumetry: relation to neurological disability score and number of relapses," *Egyptian Journal of Radiology and Nuclear Medicine,* vol. 52, no. 1, pp. 1-9, 2021.
[208] M. Avila, A. Bansal, J. Culberson, and A. N. Peiris, "The role of sex hormones in multiple sclerosis," *European neurology,* vol. 80, no. 1-2, pp. 93-99, 2018.
[209] R. N. Schwendimann and N. Alekseeva, "Gender issues in multiple sclerosis," *International review of neurobiology,* vol. 79, pp. 377-392, 2007.
[210] B. Neumann, M. Segel, K. J. Chalut, and R. J. Franklin, "Remyelination and ageing: Reversing the ravages of time," *Multiple Sclerosis Journal,* vol. 25, no. 14, pp. 1835-1841, 2019.
[211] J. M. Rist and R. J. Franklin, "Taking ageing into account in remyelination-based therapies for multiple sclerosis," *Journal of the neurological sciences,* vol. 274, no. 1-2, pp. 64-67, 2008.
[212] E. F. J. Fischi-Gomez, Mario; Bonnier, Guillaume; Granziera, Cristina, "The Age effect on Multi-parametric Magnetic Resonance Imaging changes in Multiple Sclerosis lesions," *Proc. Intl. Soc. Mag. Reson. Med. 26 (2018)*.
[213] Z. Hosseinpour *et al.*, "Texture analysis of clinical MRI detects characteristics of tissue repair in lesions of multiple sclerosis after treatment with domperidone."
[214] M. P. McGinley, C. H. Goldschmidt, and A. D. Rae-Grant, "Diagnosis and treatment of multiple sclerosis: a review," *Jama,* vol. 325, no. 8, pp. 765-779, 2021.
[215] R. C. Sommer, J. Hata, C. de Medeiros Rimkus, B. K. da Costa, J. Nakahara, and D. K. Sato, "Mechanisms of myelin repair, MRI techniques and therapeutic opportunities in multiple sclerosis," *Multiple Sclerosis and Related Disorders,* vol. 58, p. 103407, 2022.
[216] C. Enzinger *et al.*, "Nonconventional MRI and microstructural cerebral changes in multiple sclerosis," *Nature Reviews Neurology,* vol. 11, no. 12, pp. 676-686, 2015.
[217] T. Luo *et al.*, "Characterizing Structural Changes With Evolving Remyelination Following Experimental Demyelination Using High Angular Resolution Diffusion MRI and Texture Analysis," *Journal of Magnetic Resonance Imaging,* vol. 49, no. 6, pp. 1750-1759, 2019.
[218] F. Ribaldi *et al.*, "Accuracy and reproducibility of automated white matter hyperintensities segmentation with lesion segmentation tool: A European multi-site 3T study," *Magnetic Resonance Imaging,* vol. 76, pp. 108-115, 2021.
[219] J. Knight and A. Khademi, "MS lesion segmentation using FLAIR MRI only," *Proceedings of the 1st MICCAI challenge on multiple sclerosis lesions segmentation challenge using a data management and processing infrastructure-MICCAI-MSSEG,* pp. 21-28, 2016.
[220] J. Zhou *et al.*, "The Effects of GLCM parameters on LAI estimation using texture values from Quickbird Satellite Imagery," *Scientific Reports,* vol. 7, no. 1, pp. 1-12, 2017.
[221] A. Gebejes and R. Huertas, "Texture characterization based on grey-level co-occurrence matrix," *databases,* vol. 9, p. 10, 2013.

[222] X. S. Liu, *Statistical power analysis for the social and behavioral sciences: Basic and advanced techniques*. Routledge, 2013.
[223] L. Berben, S. M. Sereika, and S. Engberg, "Effect size estimation: methods and examples," *International journal of nursing studies,* vol. 49, no. 8, pp. 1039-1047, 2012.
[224] M. P. Sormani and M. Pardini, "Assessing repair in multiple sclerosis: outcomes for phase II clinical trials," *Neurotherapeutics,* vol. 14, no. 4, pp. 924-933, 2017.
[225] D. S. Meier, H. Weiner, and C. R. Guttmann, "MR imaging intensity modeling of damage and repair in multiple sclerosis: relationship of short-term lesion recovery to progression and disability," *American Journal of Neuroradiology,* vol. 28, no. 10, pp. 1956-1963, 2007.
[226] M. R. Kotter, C. Stadelmann, and H.-P. Hartung, "Enhancing remyelination in disease—can we wrap it up?," *Brain,* vol. 134, no. 7, pp. 1882-1900, 2011.
[227] R. J. Franklin, "Remyelination in the CNS: from biology to therapy," *Nature Reviews Neuroscience,* vol. 9, no. 11, pp. 839-855, 2008.
[228] D. Kremer, P. Göttle, J. Flores-Rivera, H.-P. Hartung, and P. Küry, "Remyelination in multiple sclerosis: from concept to clinical trials," *Current opinion in neurology,* vol. 32, no. 3, pp. 378-384, 2019.
[229] F. De Angelis, N. A. John, and W. J. Brownlee, "Disease-modifying therapies for multiple sclerosis," *bmj,* vol. 363, 2018.
[230] A. Cross and R. Naismith, "Established and novel disease-modifying treatments in multiple sclerosis," *Journal of internal medicine,* vol. 275, no. 4, pp. 350-363, 2014.
[231] M. W. Koch *et al.*, "Domperidone-induced elevation of serum prolactin levels and immune response in multiple sclerosis," *Journal of Neuroimmunology,* vol. 334, p. 576974, 2019.
[232] S. Zhornitsky, V. W. Yong, S. Weiss, and L. M. Metz, "Prolactin in multiple sclerosis," *Multiple Sclerosis Journal,* vol. 19, no. 1, pp. 15-23, 2013.
[233] S. Zhornitsky, T. A. Johnson, L. M. Metz, S. Weiss, and V. W. Yong, "Prolactin in combination with interferon-β reduces disease severity in an animal model of multiple sclerosis," *Journal of neuroinflammation,* vol. 12, no. 1, pp. 1-7, 2015.
[234] C. P. Loizou, V. Murray, M. S. Pattichis, I. Seimenis, M. Pantziaris, and C. S. Pattichis, "Multiscale amplitude-modulation frequency-modulation (AM–FM) texture analysis of multiple sclerosis in brain MRI images," *IEEE Transactions on Information Technology in Biomedicine,* vol. 15, no. 1, pp. 119-129, 2010.
[235] H. Tremlett, D. Paty, and V. Devonshire, "Disability progression in multiple sclerosis is slower than previously reported," *Neurology,* vol. 66, no. 2, pp. 172-177, 2006.